



UNIVERSITY OF CRETE  
PHYSICS DEPARTMENT

# Photoionization models of Active Galactic Nuclei (AGN)

MSc THESIS PROJECT

Haralampos M. Politakis

**Supervising professor:** Andreas Zezas  
Assistant Professor  
University of Crete

Heraklion, November 2009

.....  
Haralampos M. Politakis  
University of Crete

Copyright © Haralampos M. Politakis, 2009  
All rights reserved.

Reproduction, storage and distribution of this work for non-profit, educational or research purposes is permitted, provided that the source of origin is referenced. Questions regarding the use of this work for profit should be sent to the author.

The views and conclusions contained in this document reflect the author and not the official views of the University of Crete.

### **Abstract**

Active Galactic Nuclei (AGN) are among the most fascinating and strange astronomical objects. They emit an enormous amount of energy in an astronomically speaking tiny volume. Energy is generated by gravitational infall of material which is heated to high temperatures in a dissipative accretion disk. The accretion flow is composed of a cold medium (the thin accretion disk) producing a thermal radiation and a hot medium (corona) radiating in X-rays. In this work we develop a photoionization modelling procedure based on the ionizing continuum from the accretion flow models and analyse the produced emission lines using the standard optical emission line diagnostic NLR diagrams. The scope of the analysis is to investigate: if the accretion flow models can reproduce the emission line ratios of AGN and LINERs, which occupy well defined areas on the NLR diagrams; if we can distinguish between the accretion flow models (and consequently between the different geometries of the accretion flow region) from their produced emission line ratios and if LINER-type AGN could be associated with truncated accretion disks. This work is differentiated from similar studies on photoionization models for the choice of using a photoionizing continuum derived from self-consistent accretion flow models and not from either ad-hoc assumptions or empirical AGN SEDs.

---



---

## Table of Contents

<b>INTRODUCTION.....</b>	<b>7</b>
<b>PART 1. AGN BASICS.....</b>	<b>9</b>
<b>1.1. WHAT IS AN AGN?.....</b>	<b>9</b>
<b>1.2. AGN CHARACTERISTICS.....</b>	<b>10</b>
1.2.1 SPECTRAL CHARACTERISTICS.....	10
1.2.2 CONTINUUM CHARACTERISTICS.....	12
1.2.3 MORPHOLOGICAL CHARACTERISTICS.....	14
<b>1.3. THE PHYSICS OF AGN – STANDARD MODEL.....</b>	<b>16</b>
<b>1.4. AGN CLASSIFICATION.....</b>	<b>19</b>
<b>1.5. AGN DETECTION AND IDENTIFICATION.....</b>	<b>22</b>
<b>1.6. AGN COLOR-COLOR DIAGNOSTIC DIAGRAMS.....</b>	<b>24</b>
<b>1.7. AGN EMISSION LINE DIAGNOSTIC DIAGRAMS.....</b>	<b>28</b>
<b>PART 2. EMISSION LINES FROM ACCRETION FLOW MODELS.....</b>	<b>33</b>
<b>2.1. ACCRETION FLOW MODELS.....</b>	<b>34</b>
2.1.1. HOT SEMI-SPHERICAL INNER FLOW (SOBOLEWSKA ET AL. 2004).....	34
2.1.2. PATCHY CORONA (SOBOLEWSKA ET AL. 2004).....	35
<b>2.2. IONIZING CONTINUUM.....</b>	<b>38</b>
<b>2.3. CREATING A NLR MODEL USING CLOUDY.....</b>	<b>40</b>
<b>2.4. EVALUATION OF THE NLR MODEL.....</b>	<b>43</b>
<b>2.5. NLR DIAGRAMS - DATA ANALYSIS.....</b>	<b>46</b>
2.5.1. SUMMARY OF RESULTS.....	46
2.5.2. NLR DIAGRAMS →BOTH ACCRETION FLOW MODELS.....	47
2.5.3. NLR DIAGRAMS →SEMI SPHERICAL INNER FLOW MODEL.....	50
2.5.4. NLR DIAGRAMS →PATCHY CORONA FLOW MODEL.....	60
<b>2.6. CONCLUSIONS.....</b>	<b>74</b>
<b>REFERENCES.....</b>	<b>75</b>

---



---

## Table of Figures

Figure 1. Photoionization modelling procedure .....	7
Figure 2. Images of one non active (top left) and eight active galaxies (see text).....	9
Figure 3. Optical spectra of galaxies displayed in Figure 1(NED).....	10
Figure 4. Optical spectra of galaxies displayed in Figure 1(NED).....	11
Figure 5. SED of the spiral (non active) galaxy NGC 7741(NED) .....	12
Figure 6. SEDs of AGN with the SED of NGC 7741 (red dots) superimposed (NED).....	13
Figure 7. Brightness variability of AGN ( <a href="http://www.astr.ua.edu/keel/agn/vary.gif">http://www.astr.ua.edu/keel/agn/vary.gif</a> ).....	14
Figure 8. A generic model for an active galaxy ( <a href="http://openlearn.open.ac.uk/mod/resource/view.php?id=300300">http://openlearn.open.ac.uk/mod/resource/view.php?id=300300</a> ) .....	16
Figure 9. Optical spectra of different classes of AGN (NED).....	20
Figure 10. Optical spectra of the radio galaxy PKS1932-46 (Tadhunter C. 2008). .....	21
Figure 11. SDSS color-color diagrams (Richards et al. 2000) .....	24
Figure 12. Color-color diagrams from POSS II (Kennefick et al 1995). .....	25
Figure 13: $U_b, R$ color-color diagram from 2dF QSO Redshift Survey (Meyer et al. 2001) .....	25
Figure 14. Near Infrared color diagram from 2MASS (Cutri et al. 2001).....	26
Figure 15. Mid infrared color diagram (Kewley et al. 2002).....	26
Figure 16. Laurent diagnostic diagrams (Laurent et al. 2000).....	27
Figure 17. Flow chart used for classification of candidate spectra (Fischer et al. 1998).....	28
Figure 18. NLR diagnostic diagrams (Veilleux & Osterbrock 1987).....	29
Figure 19. NLR diagnostic diagrams (Kewley et al 2001) .....	30
Figure 20. Near Infrared emission line diagnostic diagrams (Veilleux & Osterbrock 1991).....	31
Figure 21. Mid-IR emission line diagnostic diagrams (Genzel et al. 2002) .....	32
Figure 22. Stages of the emission lines analysis .....	33
Figure 23. Hot semi spherical inner flow geometry (Sobolewska et al. 2004).....	34
Figure 24. Patchy corona geometry (Sobolewska et al. 2004) .....	36
Figure 25. Semi spherical inner flow continua. The displayed values for: $M_{\dot{m}} R_{tr} f \delta$ .....	38
Figure 26. Patchy corona continua. The displayed values for: $M_{\dot{m}} f \mu_s C kTe$ .....	39
Figure 27. Continua that enter in the calculations in CLOUDY .....	40
Figure 28. The continuum produced by the AGN command in CLOUDY (HAZY) .....	43
Figure 29. Quasar energy distribution (Elvis et al. 1994).....	43
Figure 30. NLR model emission line tracks (CLOUDY continuum).....	44
Figure 31. NLR model emission line tracks (Elvis continuum) .....	44
Figure 32. Production of NLR diagram $\rightarrow$ ionization from both accretion flow models.....	47
Figure 33. NLR diagram - all models.....	48
Figure 34. Variation of NLR model parameters .....	49
Figure 35. Production of NLR diagram $\rightarrow$ semi spherical inner flow model .....	50
Figure 36. Semi spherical inner flow - variation of NLR model parameters .....	51
Figure 37. Semi spherical inner flow - effect of $M$ .....	52
Figure 38. Semi spherical inner flow – effect of $M$ on NLR parameters.....	53
Figure 39. Semi spherical inner flow - effect of $R_{tr}$ (in $R_s$ ) .....	54
Figure 40. Semi spherical inner flow - effect of $R_{tr}$ on NLR parameters.....	55
Figure 41. Semi spherical inner flow - effect of $f$ .....	56
Figure 42. Semi spherical inner flow - effect of $f$ on NLR parameters .....	57
Figure 43. Semi spherical inner flow - effect of $\delta$ .....	58
Figure 44. Semi spherical inner flow - effect of $\delta$ on NLR parameters .....	59
Figure 45. Production of NLR diagram $\rightarrow$ patchy corona model.....	60
Figure 46. Patchy corona - variation of NLR model parameters.....	61
Figure 47. Patchy corona - effect of $M$ .....	62
Figure 48. Patchy corona - effect of $M$ on NLR parameters .....	64
Figure 49. Patchy corona - effect of $\dot{m}$ .....	65
Figure 50. Patchy corona - effect of $\dot{m}$ on NLR parameters.....	67
Figure 51. Patchy corona - effect of $f$ .....	67
Figure 52. Patchy corona - effect of $f$ on NLR parameters .....	69
Figure 53. Patchy corona - effect of $C$ .....	69
Figure 54. Patchy corona - effect of $C$ on NLR parameters .....	71
Figure 55. Patchy corona - effect of $\mu_s$ .....	72

---



---

Figure 56. Patchy corona - effect of  $\mu_s$  on NLR parameters ..... 73

## Table of Tables

Table 1. The main classification labels used for AGN..... 19  
Table 2. Solar chemical composition (Grevesse & Sauval 1998), ..... 41  
Table 3. Accretion flow models and NLR model parameters ..... 42  
Table 4. Summary of results → Ionization from both accretion flow models ..... 46  
Table 5. Summary of results → Ionization from the semi spherical inner flow model ..... 46  
Table 6. Summary of results → Ionization from the patchy corona model ..... 47

# Introduction

Active Galactic Nucleus (AGN) is a galaxy nucleus which shows evidence for accretion onto a supermassive black hole. It produces an enormous amount of luminosity ( $\sim 10^{12} L_{\odot}$ ) in what is astronomically speaking a tiny volume. The galaxy that hosts an AGN is called active galaxy.

According to the current working model an AGN is comprised of: The central engine (a supermassive black hole) surrounded by an accretion disc often accompanied by jets emerging perpendicular to the disc, an obscuring torus of gas and dust that surrounds the engine, the broad-line region (BLR) that occupies the area inside the torus and the narrow-line region (NLR) that lies further out. The entire AGN appears as a bright nucleus in an otherwise normal galaxy.

When comparing the optical spectra and SEDs of normal (non active) galaxies to active ones, the extraordinary characteristics of AGN emerge: Very broad permitted emission lines with a wide range of ionization, narrower forbidden lines (although broader compared to the spectral lines exhibited by normal galaxies), featureless broad band continuum (persisting over some 10 orders of magnitude in frequency).

The fundamental question about AGNs is how the energy that is detected as radiation is generated. According to the current working model, energy is generated by gravitational infall of material which is heated to high temperatures in a dissipative accretion disk. Observations of accreting sources support the hypothesis that the accretion flow is composed of a cold medium producing thermal radiation (the geometrically thin, optical thick accretion disk thermalizes the gravitational potential energy and radiates it as a multi-temperature black body giving a characteristic bump in the spectrum) and a hot medium radiating in X-rays.

Two self consistent models (Sobolewska et al. 2004) describing the ionizing continuum for two possible geometries of the accretion flow will be referenced in this paper. The geometry of the models consists of a cold, optically thick accretion disk with a hot corona above it. In the first model the disk truncates to a hot inner flow, while in the second, the corona consists of hot clouds of plasma (patchy corona) and does not truncate.

In this work we develop a photoionization modelling procedure (presented in **Figure 1**) based on the ionizing continuum from the accretion flow models and analyse the produced emission lines using the standard optical emission line diagnostic NLR diagrams. The analysis consists of the creation of a NLR model using the CLOUDY photoionization code (Ferland et al. 1998).

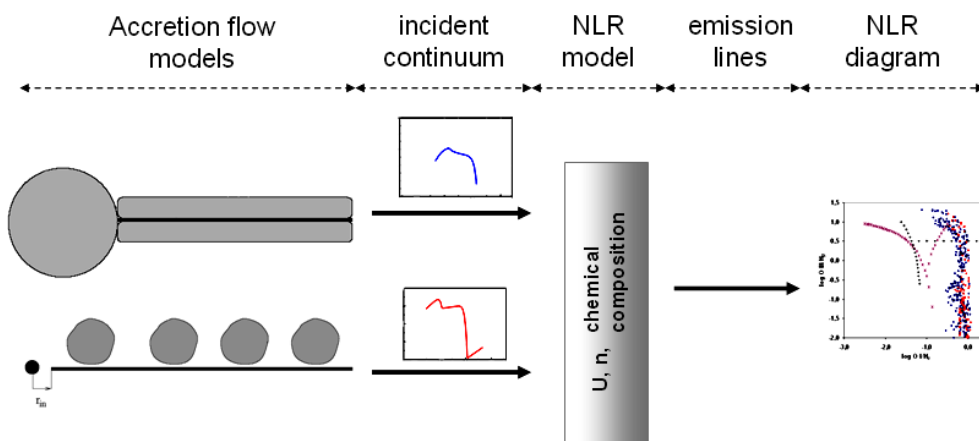


**Figure 1.** Photoionization modelling procedure

The key issue of this work is to investigate whether the accretion flow models can reproduce the emission line ratios of AGN and LINERs, which occupy well defined areas on the NLR diagrams. Another important issue is to investigate whether we can distinguish between the accretion flow models (and consequently between the different geometries of the accretion flow region) from their produced emission line ratios. A third issue that is investigated is the suggestion that LINER-type AGN could be associated with truncated accretion disks (Quataer et al. 1999) as described in the hot semi-spherical inner flow model.

This study is differentiated from similar studies on photoionization models for the choice of using a photoionizing continuum derived from self-consistent accretion flow models and not from either ad-hoc assumptions (Netzer 1990) or empirical AGN SEDs (Groves and Kewley 2007). This choice enables our analysis to avoid the drawbacks that the other studies encounter such as: the assumptions for the UV to soft X-rays part of the incident continuum (observations in the important UV to soft X-rays spectral range are rather poor since extreme UV radiation is absorbed by interstellar gas) and the fact that the empirical SEDs reflect the reprocessed radiation and therefore may not represent the ionizing continuum seen by the photoionized gas.

The paper is structured in two parts. Part 1 presents the general properties of AGN, while Part 2 presents the results from the analysis of the emission lines of the accretion flow models.

---

---

## Part 1. AGN Basics

### 1.1. What is an AGN?

We now know that all galaxy bulges harbour supermassive black holes (SMBH) in their nuclei. Most of them are quiet (starved of gas) and detectable only via orbital dynamics. But a few are accreting gas which makes them visible through the release of potential energy. Such nuclei are called **Active Galactic Nuclei** (AGN) and their hosts are called Active Galaxies. The distinctive characteristic of AGN is that they produce an enormous amount of power (luminosity) in what is astronomically speaking a tiny volume. **Figure 2** presents the images of a number of active galaxies. From top left: NGC7741 (optical; Palomar), NGC5128 (infrared; 2MASS), 3C273 (X-rays; CHANDRA), NGC1068 (optical; SDSS), NGC1275 (X-rays; CHANDRA), NGC3516 (infrared; 2MASS), NGC4051 (optical; SDSS), NGC4151 (optical; SDSS), NGC7469 (ultraviolet; GALEX). It is quite evident from the images that the active galaxies' nucleus appears as a bright point-like source in an otherwise inconspicuous spiral or elliptical galaxy.

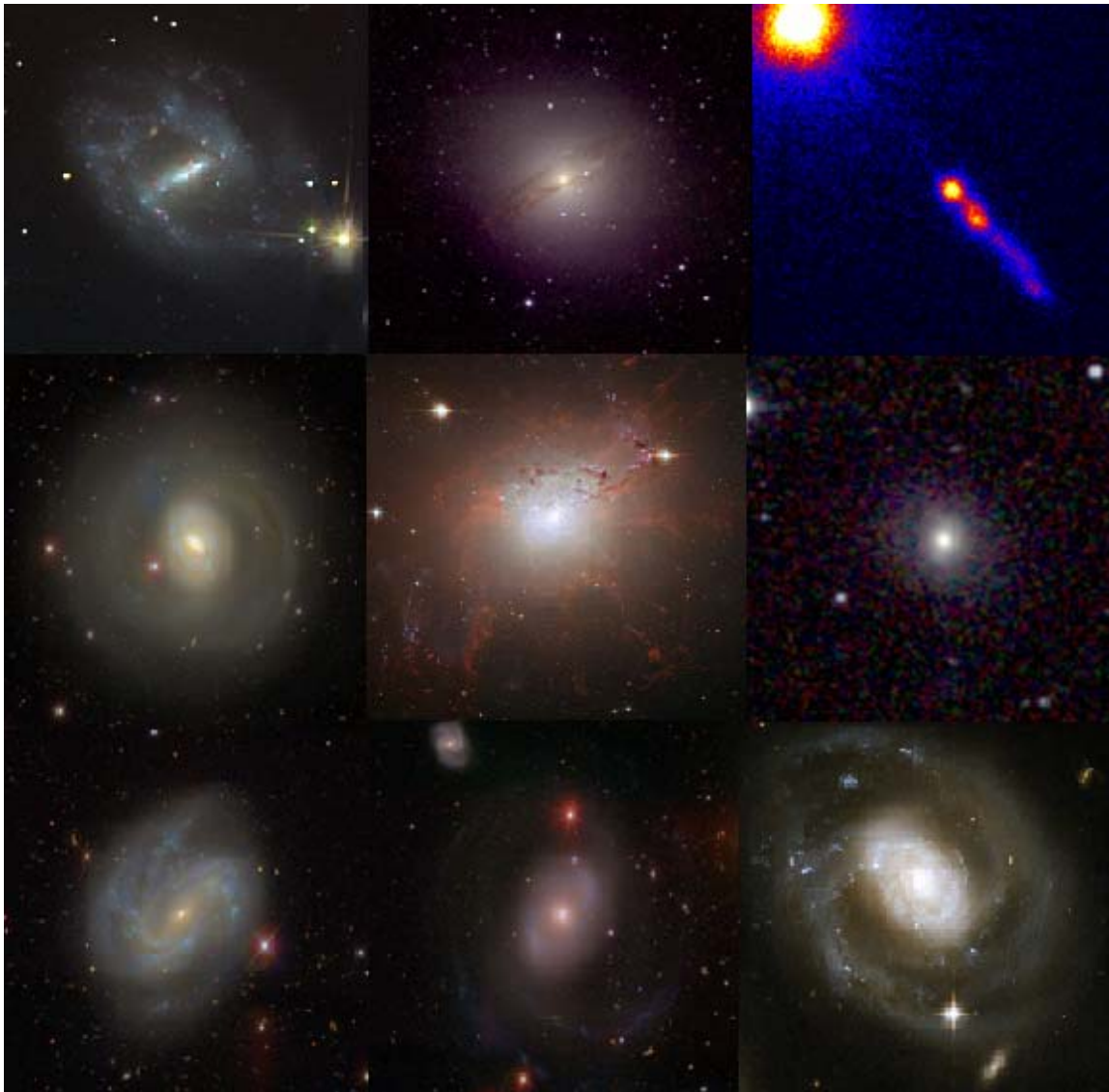


**Figure 2.** Images of one non active (top left) and eight active galaxies (see text).

## 1.2. AGN characteristics

The differences between normal (non active) and active galaxies are evident when comparing their optical spectra and their radio to X-ray Spectral Energy Distribution (SED). Furthermore, since AGN remain unresolved even when Very Long Baseline Interferometry (VLBI) is used (an indication of their small size) SEDs and optical spectra are the only tools available for deriving information on their physical structure. In **Figure 3** and **Figure 4**, the optical spectra of the galaxies displayed in Figure 2 are presented. In **Figure 5** the SED of the normal (non active) galaxy NGC 7741 is presented, while in **Figure 6**, the SED of NGC 7741 is superimposed on the SEDs of the active galaxies of Figure 2.

### 1.2.1 Spectral characteristics

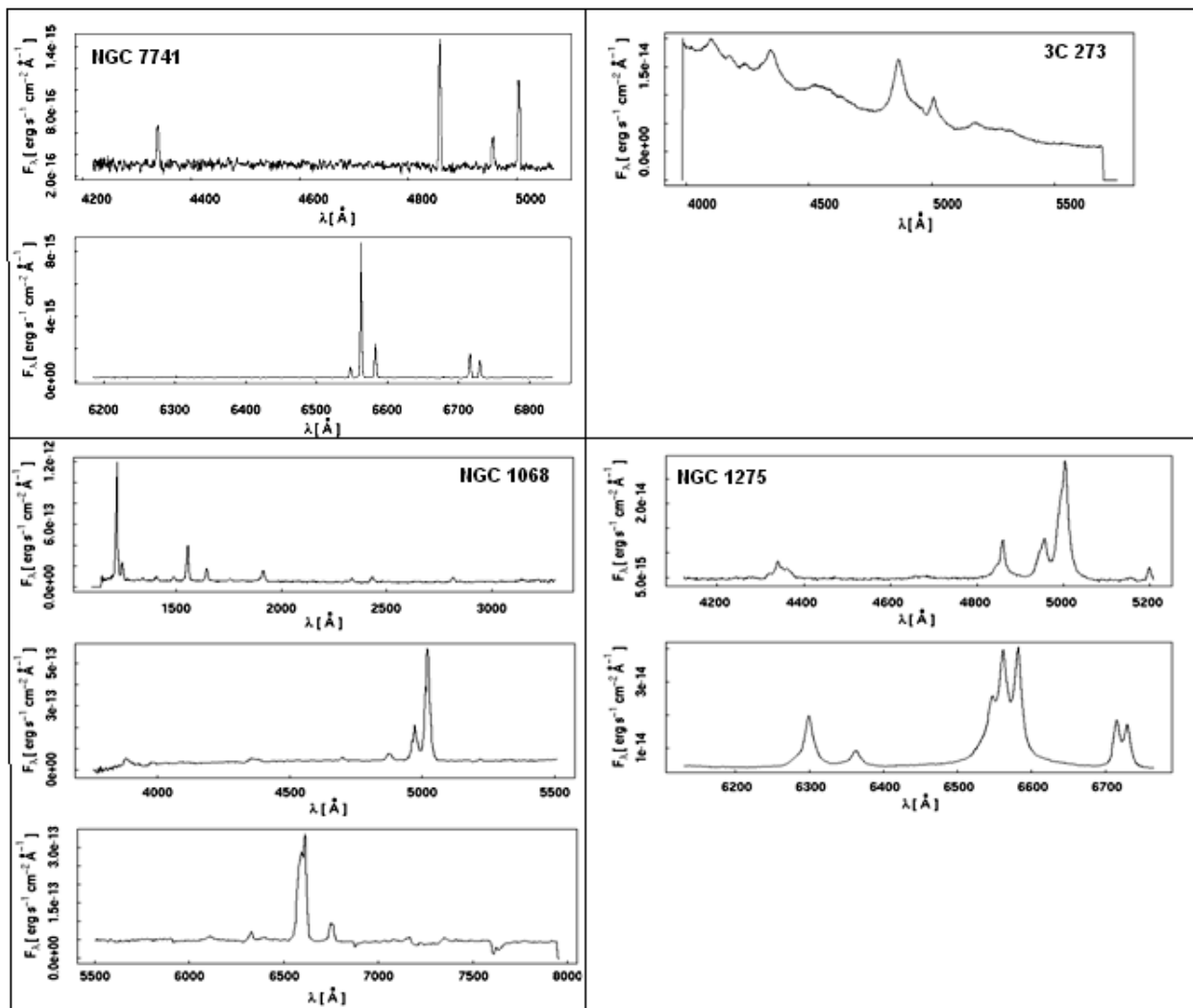


**Figure 3.** Optical spectra of galaxies displayed in Figure 1(NED)

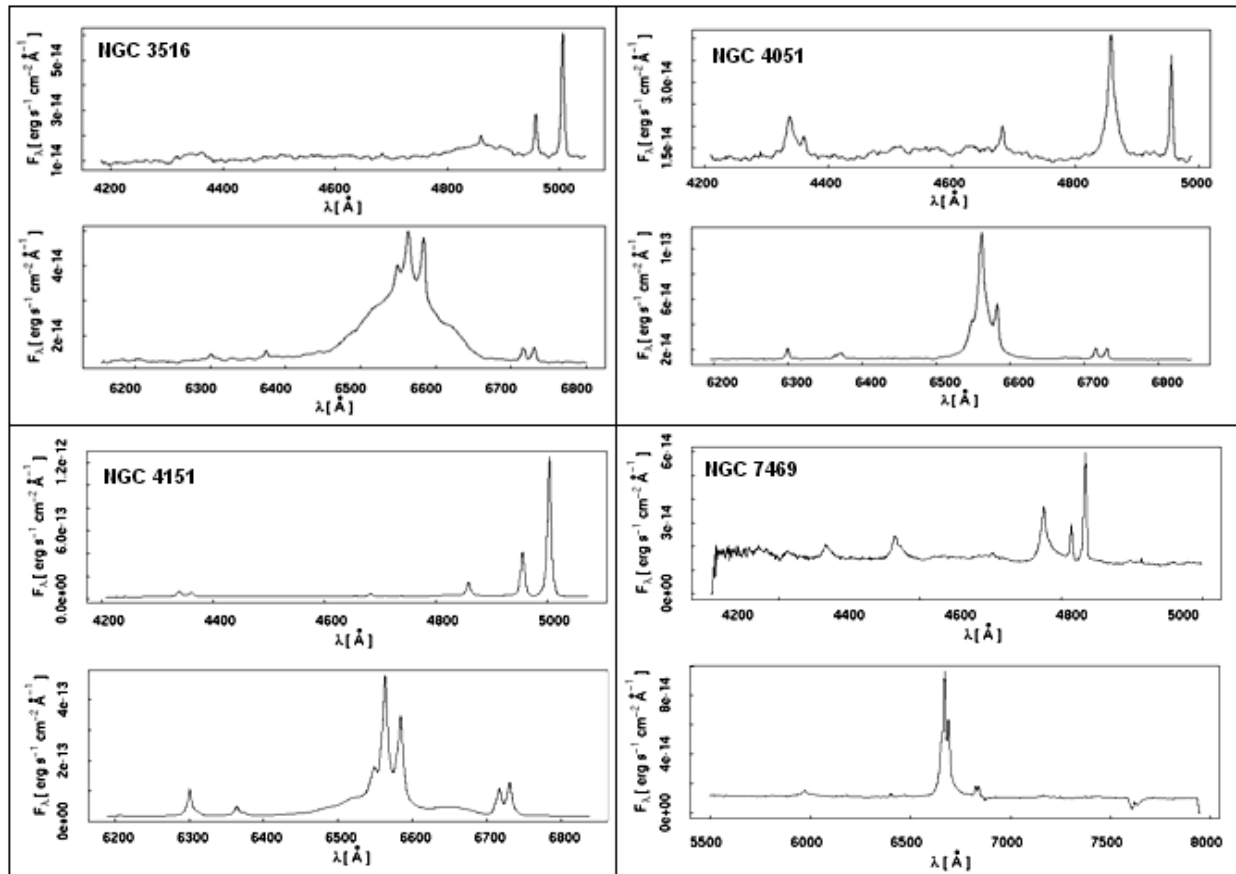


**Figure 4.** Optical spectra of galaxies displayed in Figure 1(NED)

From Figure 3 and Figure 4, comparing the spectrum of the normal (non active) galaxy NGC 7741 (top left) with the spectra of active galaxies, the spectral characteristics of AGN emerge:

- Very broad emission allowed lines (H I, He I, He II)
- Narrower forbidden lines (such as [O III]), although even the narrow lines are broad compared to the spectral lines exhibited by normal galaxies.
- Quite often high excitation lines (He II, S II)

## 1.2.2 Continuum characteristics

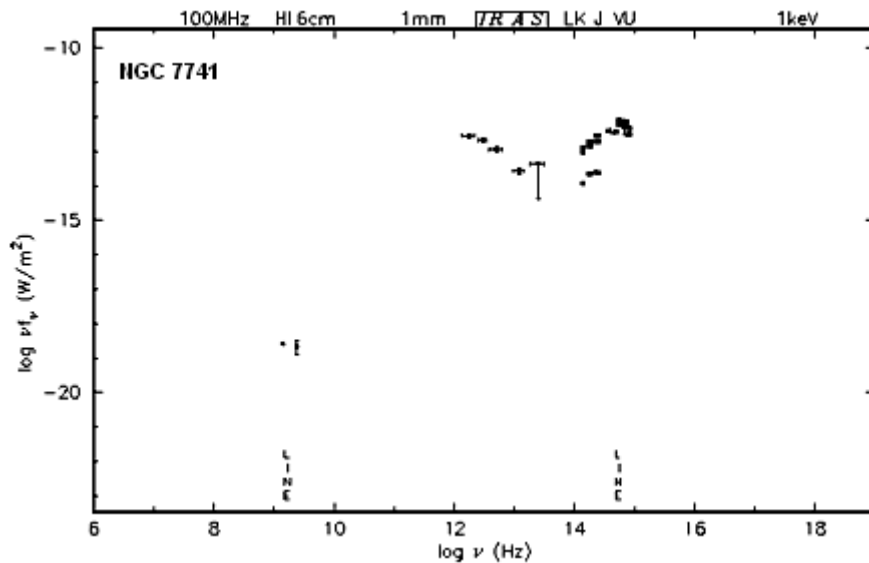


**Figure 5.** SED of the spiral (non active) galaxy NGC 7741(NED)

Comparing the SED of the normal (non active) galaxy NGC 7741 with the SEDs of active galaxies, the continuum characteristics of AGN quickly emerge:

- Featureless broad band continuum
- Active galaxies emit a normal amount of starlight in the optical and they emit several times this amount of energy at other wavelengths
- The SED is persistent over some 10 orders of magnitude in frequency. This wide spectrum is markedly different from the thermal (blackbody) spectrum of a star or the combined spectra of a galaxy of stars. Although the continuum spectra of AGNs are complicated, involving a mix of thermal and non thermal emission a power law of the form  $F_\nu \propto \nu^{-\alpha}$  is often used to parameterize the continuum between different energy bands. The spectral index typically has a value between 0.5 and 2.
- A significant amount of energy is emitted in a strong broad feature that dominates the spectrum at wavelengths shortward of  $\sim 4000 \text{ \AA}$  and extends beyond the shortest observable wavelengths in UV. This prominent feature is commonly known as the “big blue bump” and is generally agreed to be thermal in origin.



### 1.2.3 Morphological characteristics

- **Brightness variability:** The continuum spectra (or the emission lines) of most AGN vary appreciably in brightness over a one-year timescale, and several vary over timescales as short as a few hours or even seconds, especially at X-ray wavelengths (**Figure 7**). The observed variability of AGNs places the strongest constraint on their size.

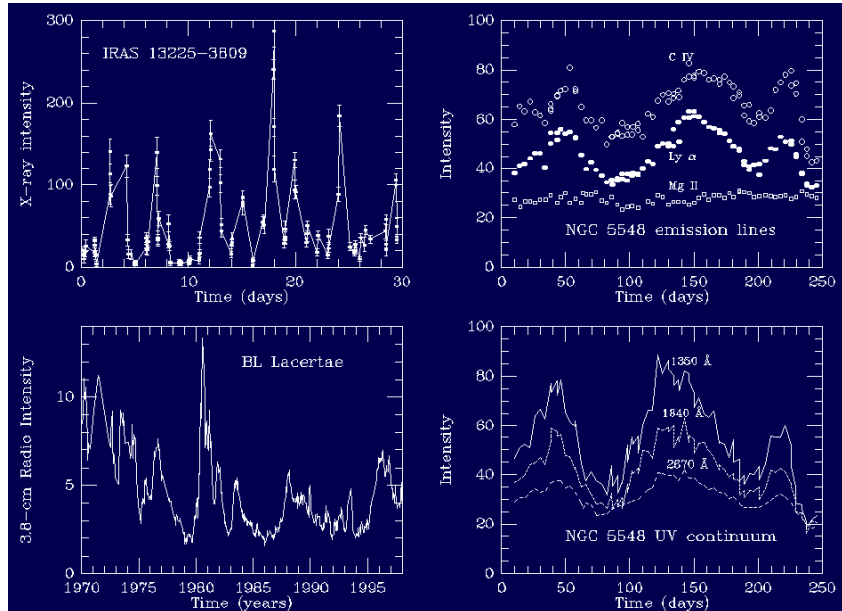


**Figure 7.** Brightness variability of AGN (<http://www.astr.ua.edu/keel/agn/vary.gif>)

- **Size:** The size of AGN is approximately  $1 \times 10^{-4}$  pc. This is derived as follows: The relationship between the maximum extent ( $R$ ) of any source of radiation and its variability ( $\Delta t$ ) is expressed as  $R \sim c\Delta t$ . Based on **Figure 7**, we obtain  $\Delta t = 1 \times 10^4$  s, therefore  $R \sim 3 \times 10^{12}$  m =  $1 \times 10^{-4}$  pc. This is a staggeringly small result that corresponds to about 20 times the distance from the Sun to the Earth. The AGN would easily fit within our Solar System.
- **Luminosity:** AGN luminosity ranges from  $L \sim 10^8$  to  $10^{14} L_{\odot}$ . For comparison, the luminosity of our galaxy is approximately  $2 \times 10^{10} L_{\odot}$ .
- **Mass:** The mass of the central source is estimated as follows (Peterson 1977): Around an accreting black hole, radiation will be so intense that it will exert a large outward pressure (radiation pressure) on the infalling material. If the force on the gas due to radiation pressure exactly counteracts the gravitational force, accretion will cease. The outward energy flux at some distance  $r$  from the center is  $F = L/4\pi r^2$ , where  $L$  is the luminosity ( $\text{erg s}^{-1}$ ) of the source. Noting that the momentum carried by a photon (energy  $E = h\nu$ ) is  $E/c$ , the outward pressure is:

$$P_{rad} = \frac{F}{c} = \frac{L}{4\pi r^2 c}$$

and the outward radiation force on a single electron is thus obtained by multiplying by the cross-section for interaction with a photon:

$$F_{rad} = \sigma_e \frac{L}{4\pi r^2 c} r$$

where  $\sigma_e$  is the Thomson scattering cross-section. The gravitational force acting on an electron-proton pair (masses  $m_e$  and  $m_p$  respectively) by a central mass  $M$  is:

$$F_{grav} = -\frac{GM(m_p + m_e)}{r^2} r \approx -\frac{GM(m_p)}{r^2} r$$

The inward gravitational force acting on the gas must balance or exceed the outward radiation force if the source is to remain intact:

$$\begin{aligned} |F_{rad}| \leq |F_{grav}| &\Leftrightarrow \sigma_e \frac{L}{4\pi r^2 c} \leq \frac{GM(m_p)}{r^2} \Leftrightarrow L \leq \frac{4\pi G c m_p}{\sigma_e} M \Leftrightarrow \\ L &\approx 1.26 \times 10^{38} (M / M_\odot) \text{ erg s}^{-1} \end{aligned} \quad (1)$$

Equation (1) is known as the Eddington limit and can be used to establish a minimum mass, the Eddington mass  $M_E$ , for a source of luminosity  $L$ . In units appropriate for AGN:

$$M_E = 8 \times 10^5 L_{44} M_\odot \quad (2)$$

For a typical quasar luminosity  $L_{QSO} \approx 10^{46} \text{ erg s}^{-1}$ , (2) gives:  $M \approx 10^8 M_\odot$

### 1.3. The Physics of AGN – Standard model

A set of detailed spectroscopic and spectropolarimetric observations have led to the development of the so-called “standard model”. The standard model consists of the following components (**Figure 8**): (a) The central engine is a supermassive black hole surrounded by an accretion disc with jets emerging perpendicular to the accretion disc. (b) The engine is surrounded by an obscuring torus of gas and dust. The broad-line region occupies the inner region of the torus and the narrow-line region lies further out. (c) The entire AGN appears as a bright nucleus in an otherwise normal galaxy. Note that the jets extend to beyond the host galaxy and often terminate in radio lobes

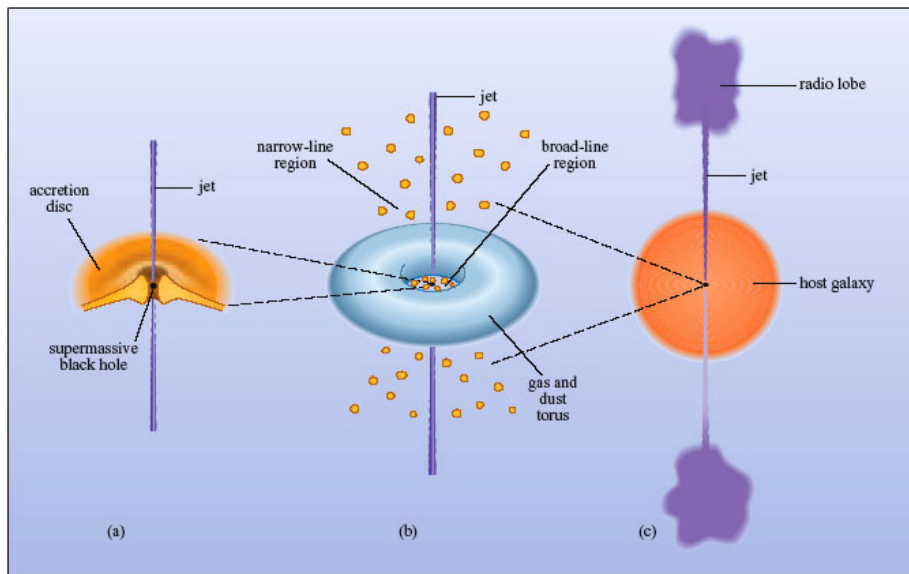


**Figure 8.** A generic model for an active galaxy (<http://openlearn.open.ac.uk/mod/resource/view.php?id=300300>.)

**Supermassive black hole:** Although incontrovertible observational proof of the existence of supermassive black holes (SMBHs) has not yet been found, evidence is mounting to suggest the presence of massive dark objects, or large mass concentrations at the centres of galaxies. The presence of SMBHs has been inferred indirectly from the energetics of accretion required to power luminous AGN and explain rapid flux variability and, more directly, from kinematics studies of the influence of the black hole’s gravitational pull on stars and gas orbiting close to it in the central regions of both active and non-active galaxies.

**Accretion disk:** Cold material close to the central black hole forms an accretion disc. Dissipative processes in the accretion disc transport matter inwards and angular momentum outwards, while causing the accretion disc to heat up. The expected spectrum of an accretion disc around a supermassive black hole consists of a combination of black body spectra arising from regions of the disk with different temperatures and peaks in the optical-ultraviolet waveband; in addition, a corona of hot material forms above the accretion disc and can inverse-Compton scatter photons up to X-ray energies. The peak temperature of the thermal emission scales like  $M^{-1/4}$  so for more massive black holes the peak temperature of the accretion disc will be lower.

**Relativistic jets:** At least some accretion discs produce jets, twin highly collimated and relativistic outflows that emerge in opposite directions from the vicinity of the SMBH (the direction of the jet ejection must be determined either by the angular momentum axis of the disc

or the spin axis of the black hole). The jet production mechanism and the jet composition on very small scales are not known at present. The jets have the most obvious observational effects in the radio waveband, where Very Long Baseline Interferometry can be used to study the synchrotron radiation they emit down to sub-parsec scales. However, they radiate in all wavebands from the radio through to the gamma-ray via the synchrotron and inverse-Compton process, and so AGN with jets have a second potential source of continuum radiation.

**The obscuring torus:** Spectropolarimetry data of the nucleus of NGC 1068 (Antonucci and Miller 1985) discovered that ~16% of non stellar continuum is polarized and suggested that for all Seyfert 2 galaxies the ionizing continuum and broad line region are located inside an optically and geometrically thick disk. The ionizing continuum and the broad line photons are scattered into the line of sight by free electrons above and below the disk. Working on the idea, the standard model includes a torus of gas and dust that surrounds the central engine that accounts for the strong infrared emission from many AGNs, The dust particles – which are usually assumed to be grains of graphite – will be heated by the radiation from the engine until they are warm enough to radiate energy at the same rate at which they receive it. So such a dust cloud will act to convert ultraviolet and X-ray emission from the engine into infrared radiation, with the shortest wavelengths coming from the hottest, inner parts of the cloud.

**Broad-line region (BLR):** BLR corresponds to dense fast-moving clouds that surround the central engine within the opening in the middle of the dust torus. At this distance from the black hole orbital speeds are several thousand kilometres per second, which is consistent with the typical speed of  $5000 \text{ km s}^{-1}$  that is measured from Doppler broadening. The clouds are fully exposed to the intense radiation from the engine and will be ionized to a high degree of excitation. Broad lines are not seen in every AGN. According to the “standard model” every AGN has a broad-line region, but in some cases our view of the BLR clouds is obscured by the dust torus, so broad lines do not appear in the spectrum.

**Narrow-line region (NLR):** NLR is the most extensive part of the AGN and envelops all the other components. It is placed much further out from the central engine where orbital speeds are lower;  $200\text{--}900 \text{ km s}^{-1}$  is typical for the NLR. An important consequence of the NLR being outside the dust torus is that it is always in view, so narrow lines will be seen even if the broad-line emitting gas is obscured. The NLR is illuminated by radiation from the central engine. As the engine is partly hidden by the dust torus, radiation can only reach the NLR through the openings along the axis of the torus. Any gas near the plane of the torus lies in its shadow and will not be illuminated.

On the basis of the aforementioned model, the features of the AGN spectrum and SED can be explained:

- **Optical continuum.** This is visible whenever we have a direct view of the accretion disc. If the direct continuum is reprocessed by the torus we still see optical either leaking through the torus or scattered in the NLR. Jets can also contribute to this component of the AGN emission. The optical continuum has a roughly power-law dependence on wavelength.
- **Broad optical emission lines.** These come from cold material located at the BLR. The lines are broad because the emitting material is revolving around the black hole with high speeds, emitting photons at varying Doppler shifts.
- **Narrow optical emission lines.** These come from more distant cold material located at the NLR, and so are narrower than the broad lines.
- **Infra-red continuum.** This is visible whenever the accretion disc and its environment are obscured by gas and dust of the obscuring torus and then re-emitted as thermal emission.

- **Radio continuum.** This is associated with a jet either in small (pc) or large (Kpc) scales. It shows a spectrum characteristic of synchrotron radiation.
- **X-ray continuum.** This can arise both from a jet and from the hot corona of the accretion disc via scattering processes: in both cases it shows a power-law spectrum.
- **X-ray emission lines.** This is a result of illumination of cold heavy elements on the accretion disk or the inner side of the torus by the X-ray continuum. Fluorescence gives rise to various emission lines, the best-known of which is the iron feature around 6.4 keV.

## 1.4. AGN Classification

It is convenient to divide AGN into two classes, conventionally named radio-quiet and radio-loud. In the radio-loud objects a contribution from the jet(s) dominates the luminosity of the AGN, at least at radio wavelengths. AGN are further divided into different classes according to their optical spectrum characteristics and their time variability (**Table 1**).

Observational Characteristics	Radio Quiet	Radio Loud	
Broad permitted lines detected at optical wavelengths	Radio quiet quasar (RQQ)	Radio loud quasar (RLQ)	Type 1
	Seyfert 1	Broad line radio galaxy (BLRG)	
Only narrow emission lines	Seyfert 2	Narrow line radio galaxy (NLRG)	Type 2
Lower luminosity AGN	LINER	Weak line radio galaxy (WLRG)	Type 3
Rapid variability at optical wavelengths		BL Lac	Type 0
		Optically violent variable quasar (OVV)	

**Table 1.** The main classification labels used for AGN

Quasar spectra are remarkably similar to those of Seyfert galaxies, except that (a) stellar absorption features are very weak, if detectable at all, and (b) the narrow lines are generally weaker relative to the broad lines than is the case in Seyfert galaxies (Peterson 1997) Another criterion for distinguishing Seyfert galaxies from quasars is according to their nuclear magnitudes (Schmidt et al. 1983) with  $M_B > -21.5+5\log h_0$  for Seyfert galaxies and  $M_B < -21.5+5\log h_0$  for quasars.

The classification into two types, Seyfert 1 and 2, may further include intermediate types such as Seyfert 1.5 (intermediate type H I profiles in which both components can be easily recognized), Seyfert 1.8 (strong narrow components and very weak but visible broad components of H $\alpha$  and H $\beta$ ) and Seyfert 1.9 (weak broad components of H $\alpha$  and none at H $\beta$ )

LINERs (Low Ionization Nuclear Emission-line Region) are the least luminous and the most common AGNs. At least 30% of all spiral galaxies show this phenomenon and the fraction may even be larger (Ho et al. 1994). LINERs show strong, low excitation emission lines, compared with the high excitation narrow lines of other AGNs (Heckman 1980).

BL Lacs (named after its prototype, BL Lacertae) are AGN characterized by rapid and large amplitude flux variability and significant optical polarization. BL Lacs have spectra dominated by a featureless non-thermal continuum and are believed to be intrinsically identical to low power radio galaxies but with the jet closely aligned to the line of sight of the observer.

Optically violent variable quasars (OVV quasar) are similar in appearance to BL Lacs but generally have stronger broad emission lines, and tend to have higher red shift components.

**Figure 9** presents optical spectra from the different types of AGN (the respective type indicated in red). All spectra are obtained from NED otherwise referenced in the respective spectrum.

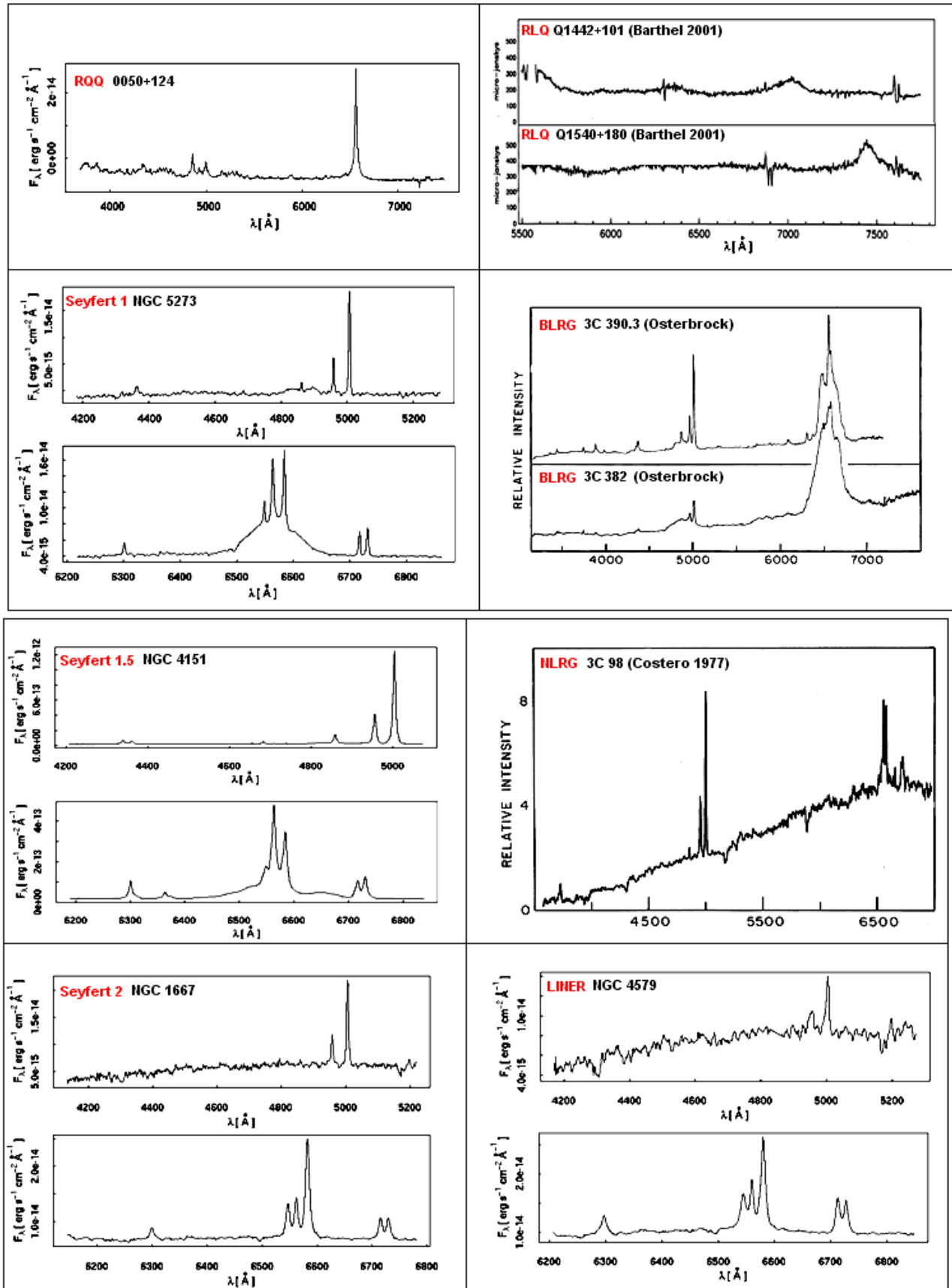
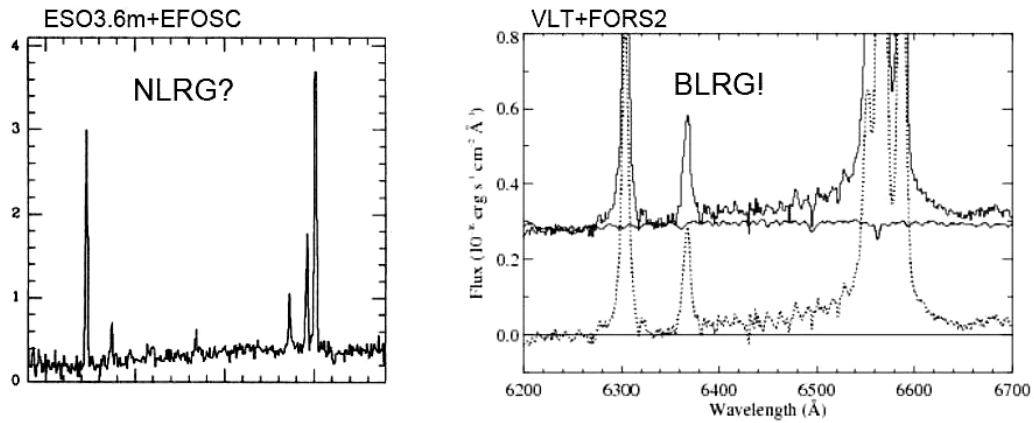


Figure 9. Optical spectra of different classes of AGN (NED)

It is worth noting that AGN terminology is often confusing, since the distinctions between different types of AGN sometimes reflect historical differences in how objects were discovered or initially classified, rather than real physical differences. Furthermore, as instrumental sensitivity improves, and new techniques are developed, classifications can change. The case of PKS1932-46 shown in **Figure 10** illustrates this point well. Although this object was originally classified as a NLRG based on relatively low S/N blue spectra taken with the ESO3.6m telescope, a higher S/N spectrum taken on the 8m VLT reveals a broad H $\alpha$  line.



**Figure 10.** Optical spectra of the radio galaxy PKS1932-46 (Tadhunter C. 2008).

## 1.5. AGN Detection and Identification

The general principle for discovering AGNs is to make use of their unique characteristics (see §1.2) in which they are not like stars or galaxies, for example, how they differ in the SEDs or emission-line spectra. The point like, spatially unresolved, nature of the nuclei is another distinguishing factor.

In the UV/optical/near-IR the characteristic AGN emission-line spectra stand out for the strength and breadth of the principal emission lines and for the wide range of ionization. Typical line widths of permitted lines are 5000 km/s or more. The strongest individual lines are those of hydrogen ( $\text{Ly}\alpha$ ,  $\text{H}\alpha$ , and  $\text{H}\beta$ ), C IV, C III, Mg II, and N V, while broad emission complexes of Fe II are visible. In addition, forbidden lines of [O I], [O II], [O III], and [S II] are prominent.

In the infrared, there are also characteristic emission lines from relatively high excitation ions, such as the [NeV]  $\lambda 14.3\mu\text{m}$ , [NeV]  $\lambda 24.3\mu\text{m}$ , [OIV]  $\lambda 25.9\mu\text{m}$ , [SIV]  $\lambda 10.5\mu\text{m}$  and [SIII]  $\lambda 18.7/33.5\mu\text{m}$ . Furthermore, another characteristic is the strength of the PAH (Polycyclic Aromatic Hydrocarbon) emission bands at 3.3, 6.2, 7.7, 8.7 and 11.2  $\mu\text{m}$ , which are ubiquitous in normal galaxies and starbursts but suppressed in AGN since the hard radiation field photo-dissociates the PAH molecules.

The diagnostic tools used in most of the surveys in UV/optical/near-IR/IR, consist of bidimensional color-color diagrams (see §1.6) or emission line ratio diagrams (see §1.7)

Radio selection was the original way to find AGN. It is very powerful; since almost all luminous radio sources are AGN in our definition of radiating supermassive black holes (normal stars and galaxies are weak emitters in these wavelengths). The only contamination is at lower luminosities, where there can be significant radio emission from very active star-forming regions. Quasars and radio galaxies are the most luminous radio sources known. The emission process is well known to be synchrotron emission by relativistic electrons in a magnetic field, leading to power-law spectra. Thus, for most luminous objects, mere detection in the radio indicates the presence of an AGN. Radio surveys are rather sensitive, and the positions are extremely accurate allowing counterparts in other wavelength bands to be readily identified. The morphological information is also important, since all radio sources showing double-lobe or jet-like structures are AGN.

X-rays emission, like radio emission, is an almost certain indicator of the existence of an AGN and does not need "confirmation" by data in other wavelength bands. The efficiency of X-ray surveys is very high, finding considerably more AGN at a fixed optical magnitude than other techniques. Selection of AGN rely on the advantages of X-rays such as their penetrating power (even column densities of  $3 \times 10^{23} \text{ cm}^{-2}$  do not reduce the flux at  $E > 5 \text{ keV}$  significantly), the great sensitivity of Chandra and XMM-Newton (sources in the luminosity range  $10^{42} - 10^{46} \text{ ergs s}^{-1}$  can be detected out to  $z \sim 3$ , independent of the nature of the host galaxy) and the accurate positions provided from Chandra.

In  $\gamma$ -rays, AGN represent the largest identified class of high-energy sources and are generally only detected as  $\gamma$ -ray sources when one of the jets is directed toward us. This is also the orientation in which the torus and material accreting around the black hole at the centre does not actually obscure the black hole or the inner part of the jet. Therefore,  $\gamma$ -ray surveys will detect mostly BL Lac, OVV objects and loud radio galaxies.

Objects in radio, X-ray and gamma-ray catalogs are then matched to optical catalogs for identification and follow-up optical spectroscopy in order to confirm the identification and establish the redshift and nature of the object.

## 1.6. AGN color-color diagnostic diagrams

In the **optical** waveband region, identification of AGN is based on the different colors of AGN compared to stars. Stars have a spectrum that is roughly blackbody in shape, whereas AGN have spectra that are characterized by featureless blue continua and strong emission lines, causing AGN to have colors quite different from those of stars. **Figure 11** presents three color-color diagrams from Sloan Digital Sky Survey. SDSS uses a dedicated 2.5 m telescope to obtain CCD images down to  $\sim 23$  mag in five broad optical bands  $u'$ ,  $g'$ ,  $r'$ ,  $i'$ , and  $z'$ , centered at 3540, 4770, 6230, 7630, and 9130 Å respectively.

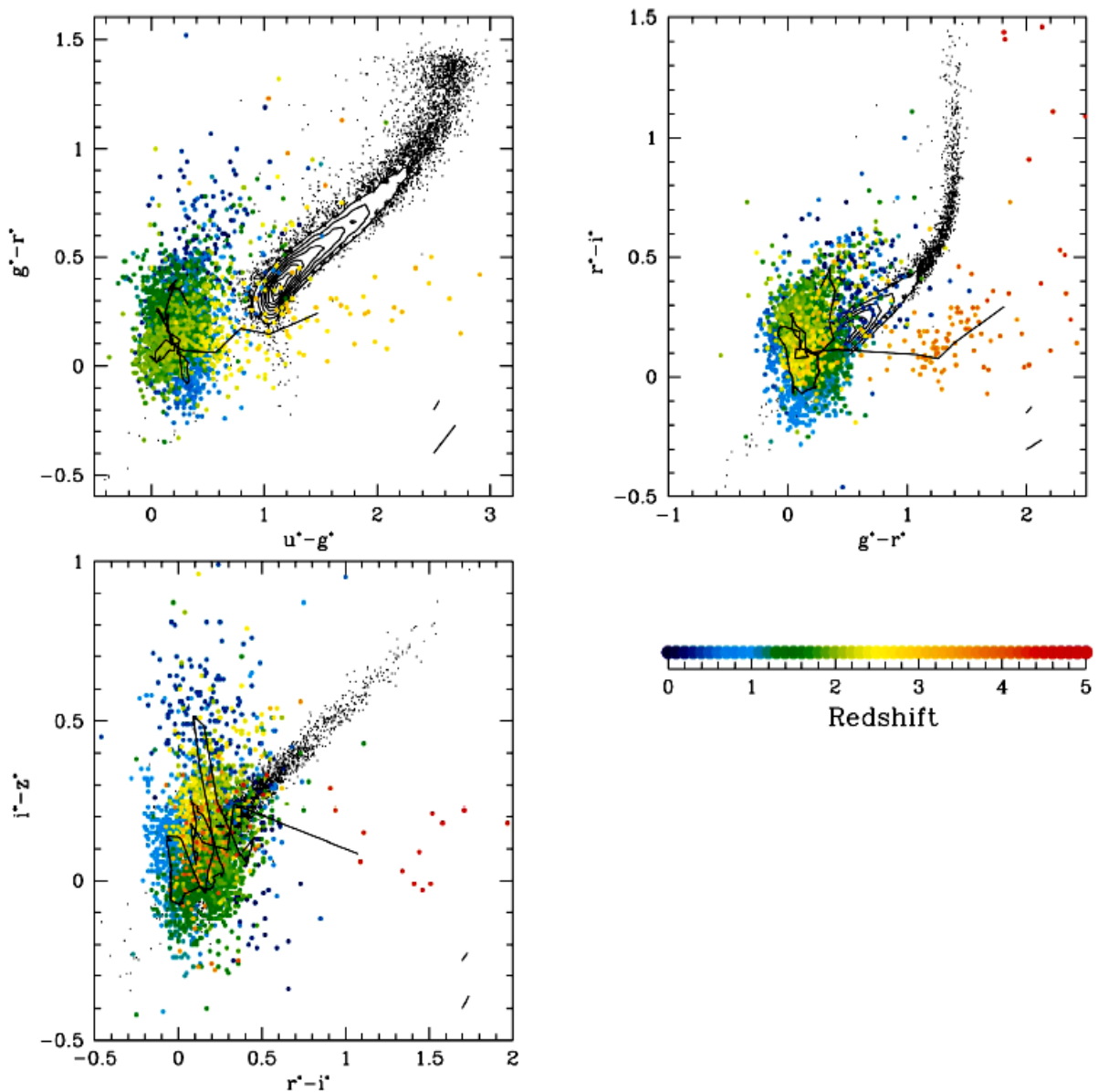


**Figure 11.** SDSS color-color diagrams (Richards et al. 2000)

**Figure 12** presents three color-color diagrams from the second Palomar Observatory Sky Survey (POSS II). The large circles are the identified quasars. The solid lines demark the survey selection area: objects are chosen as candidates if they lie to the right of these lines.

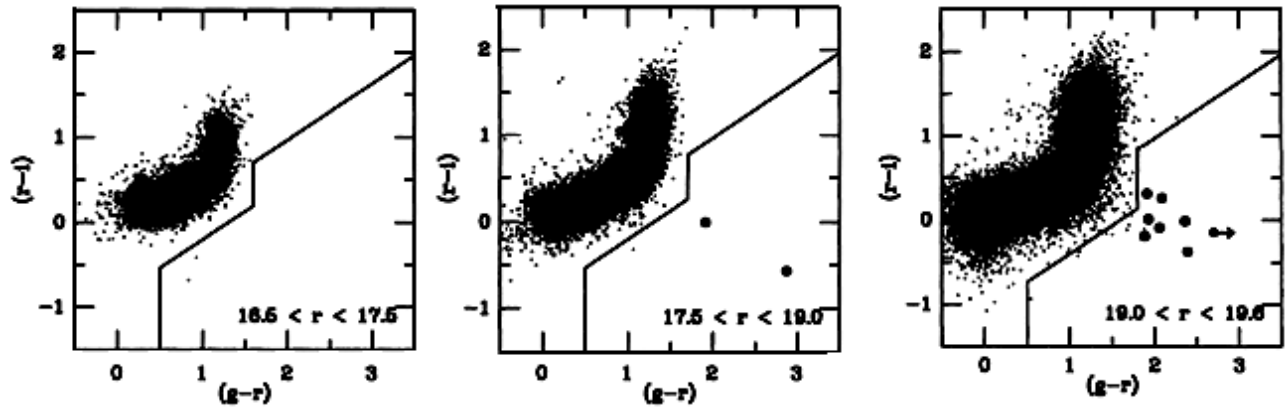


**Figure 12.** Color-color diagrams from POSS II (Kennefick et al 1995).

**Figure 13** presents a  $U_bR$  color-color diagram of QSOs and stars from 2dF QSO Redshift Survey. The multicolour selection cutoff used is shown by the dotted line.

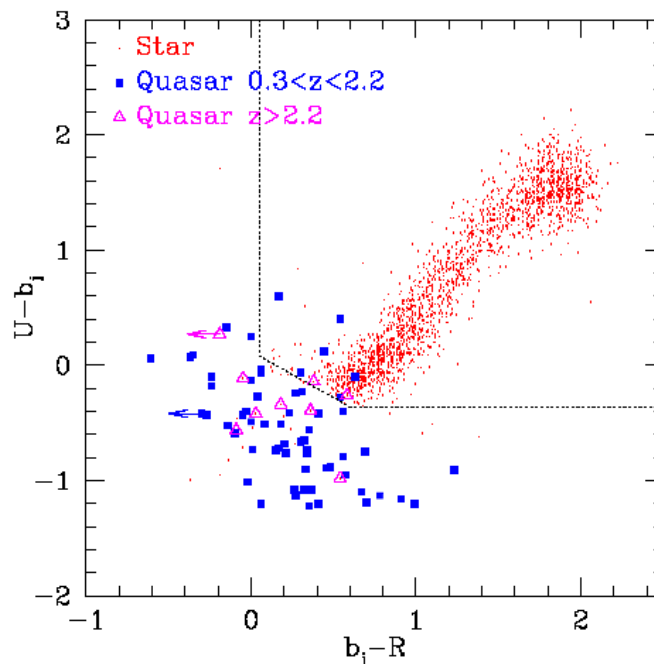


**Figure 13:**  $U_bR$  color-color diagram from 2dF QSO Redshift Survey (Meyer et al. 2001)

In the **near IR**, a simple color selection criterion can be defined based on the fact that virtually all known QSOs have  $J - K_s \leq 2.0$  mag. **Figure 14** presents a near Infrared color diagram from the Two Micron All-Sky Survey (2MASS) in the J ( $1.25 \mu\text{m}$ ), H ( $1.65 \mu\text{m}$ ), and  $K_s$  ( $2.17 \mu\text{m}$ ) photometric bands.

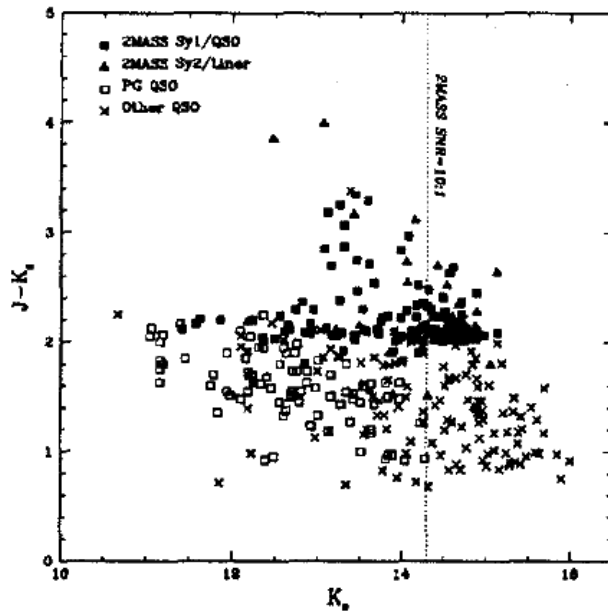


Figure 14. Near Infrared color diagram from 2MASS (Cutri et al. 2001)

In the **mid-IR**, emission of AGNs is dominated by dust continuum re-radiating energy from black hole accretion. Infrared colors such as the flux ratio  $F_{25\mu\text{m}}/F_{60\mu\text{m}}$  is considered a good indicator of AGN activity, since AGN heat the dust to higher temperatures (warmer colors – higher  $F_{25\mu\text{m}}/F_{60\mu\text{m}}$  ratio) than star-forming regions (Hunt & Malkan 1999). **Figure 15** presents a mid infrared color diagram of the ratio  $F(25\mu\text{m})/F(60\mu\text{m})$  vs.  $[\text{O III}] \lambda 5007/\text{H}\beta$ . Galaxies classed as AGNs (filled circles), starbursts (crosses), and composite/ possible composite (open circles) objects are shown.

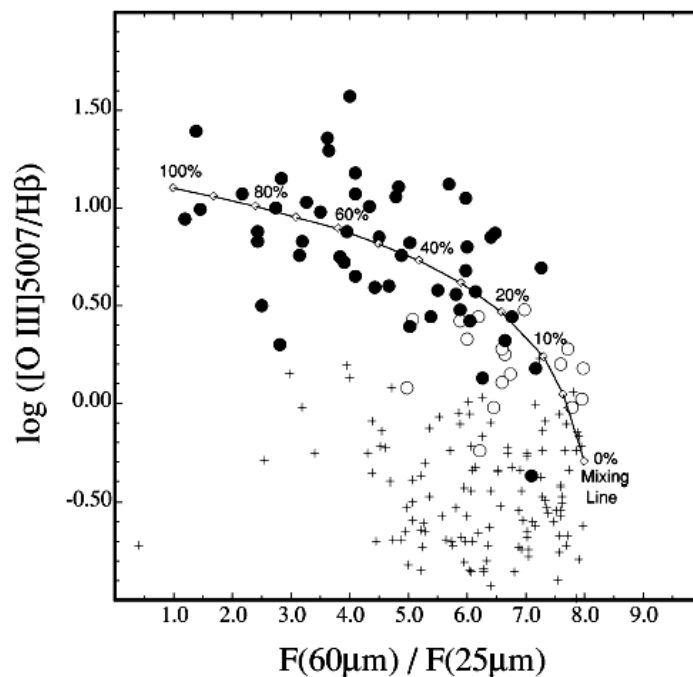
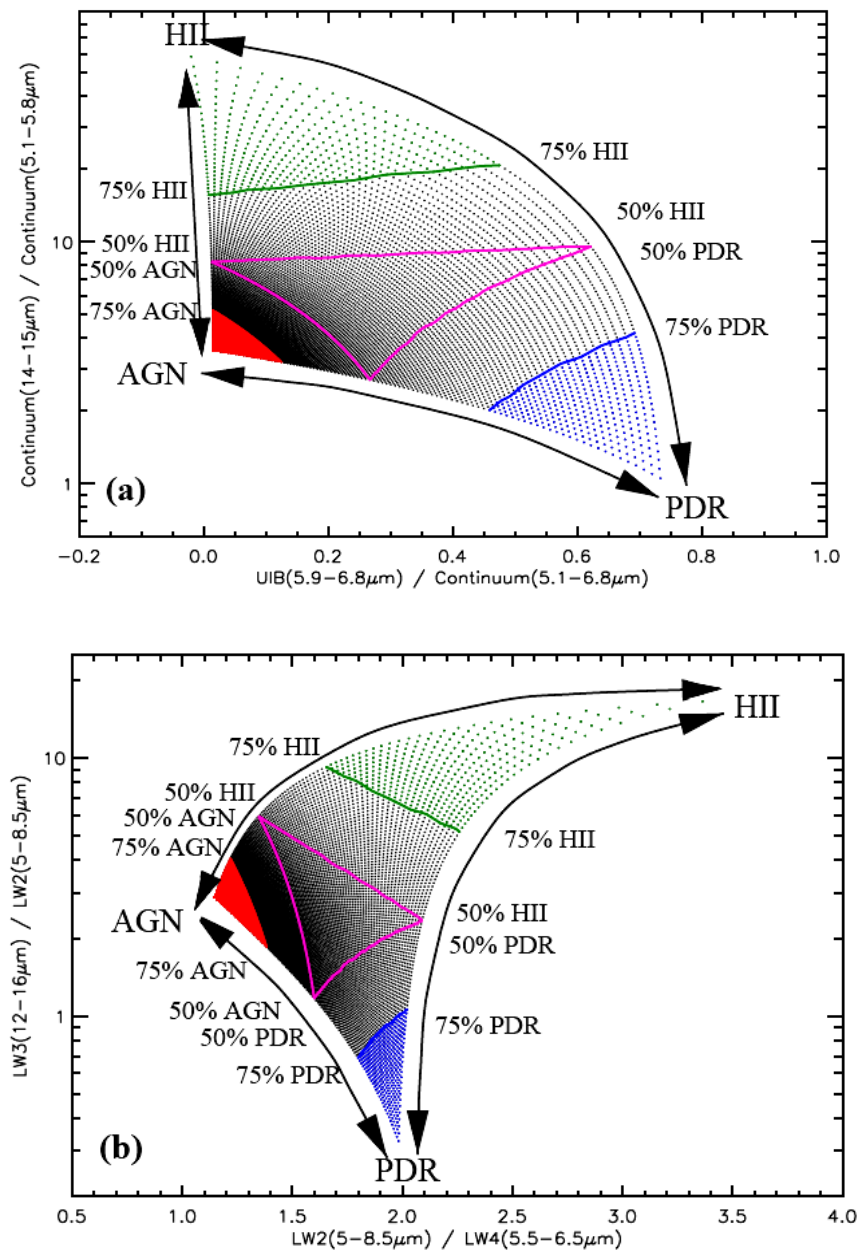


Figure 15. Mid infrared color diagram (Kewley et al. 2002).

Mid-IR emission arises mostly from HII regions, photo-dissociation regions (PDRs) and AGNs. The analysis of the strength of the 6.2  $\mu\text{m}$  Unidentified Infrared Band (UIB) and the mid-IR continuum shows that UIBs are very faint or absent in regions harbouring the intense and hard radiation fields of AGNs and pure HII regions where the UIB carriers could be destroyed while the presence of an important continuum in the 3–10  $\mu\text{m}$  band which originates from very hot dust heated by the intense AGN radiation field is a signature of AGNs. Using these two distinct spectral properties, Laurent (Laurent et al. 2000) proposed an AGN diagnostic method – now called the “Laurent Diagram”– that provides quantitative estimates of the AGN, PDR and HII region contribution. **Figure 16** presents two Laurent diagrams. In the upper corner, spectra are dominated by massive HII regions such as those found in starbursts. On the lower left, AGN spectra are dominant in a very small region, and finally, PDR spectra fall in the lower right part. The solid lines and the associated percentages indicate a constant fraction of one component along each line.



**Figure 16.** Laurent diagnostic diagrams (Laurent et al. 2000).

## 1.7. AGN emission line diagnostic diagrams

In the **optical** region, identification of AGNs is based on the emission-line spectrum that stands out for the strength and breadth of the principal emission lines and for the wide range of ionization. Typical line widths of permitted lines are 5000 km/s or more. The strongest individual lines are those of hydrogen ( $\text{Ly}\alpha$ ,  $\text{H}\alpha$ , and  $\text{H}\beta$ ), C IV, C III], Mg II, and N V, while broad emission complexes of Fe II are visible. In addition, forbidden lines of [O I], [O II], [O III], and [S II] are prominent. The detection of broad line components ( $>2000$  km/s) provides the capability for the identification of broad line AGN (Seyfert 1s, 1.5s, 1.9s and BLRGs).

But what about narrow line AGN (Seyfert 2s, NLRGs, LINERs) that present weaker activity? How does one hunt for them since optical spectra from H II regions and starburst galaxies present similar narrow line components? One of the most sensitive diagnostics of activity is narrow emission line ratios where several combinations of easily measured emission line ratios can be used to separate emission line galaxies into the three aforementioned categories: H II regions or starbursts, Seyfert 2s and NLRGs, LINERs. **Figure 17** presents a flowchart used for the classification of objects according to their optical spectra analysis.

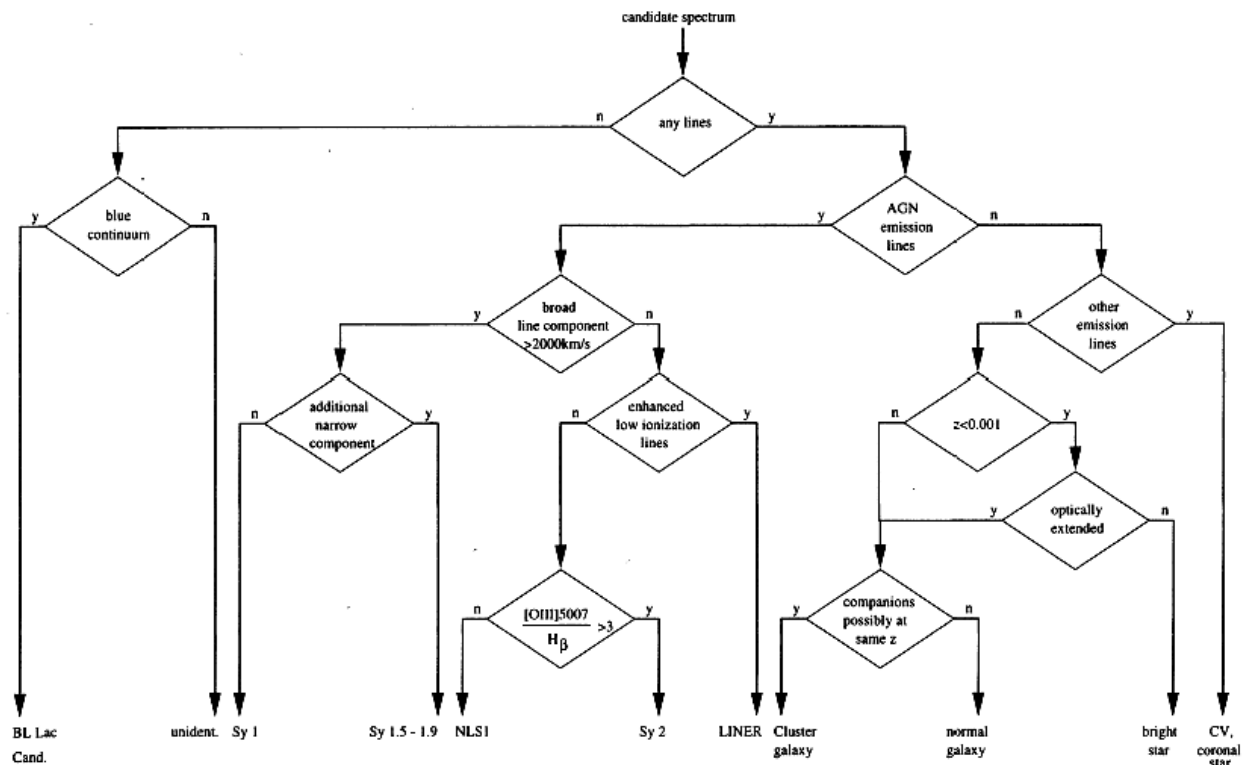


**Figure 17.** Flow chart used for classification of candidate spectra (Fischer et al. 1998)

Veilleux & Osterbrock (1987) have proposed a semi empirical method of classification involving the line ratios  $[\text{O III}] \lambda 5007 / \text{H}\beta$ ,  $[\text{N II}] \lambda 6583 / \text{H}\alpha$ ,  $[\text{S II}] \lambda \lambda 6717, 6731 / \text{H}\alpha$  and  $[\text{O I}] \lambda 6300 / \text{H}\alpha$ . These line ratios take full advantage of the physical distinctions between the various types of objects, minimizing the effects of reddening correction and calibration errors and were chosen since they satisfy the following five criteria:

1. Each ratio should be made up of strong lines that are easy to measure in typical spectra.

2. Lines that are badly blended with other lines should be avoided because the somewhat subjective nature of the deblending procedure increases the uncertainty in the flux measurements of these lines.
3. The wavelength separation between the two lines should be as small as possible so that the ratio is relatively insensitive to reddening and flux calibration.
4. Ratios involving a line of only one element and an H I Balmer line should be preferred to those involving forbidden lines of different elements, because they are less abundance-sensitive.
5. The lines should be in a region of the spectrum accessible with present-day instruments. Among other considerations, lines in the ultraviolet should be avoided because of the low sensitivity of many CCDs at short wavelengths.

**Figure 18** presents the semi empirical diagnostic diagrams (known as NLR diagrams) derived from Veilleux & Osterbrock's line ratios. Symbols for types of objects are shown in keys. Four short-dashed lines are H II region models of Evans and Dopita (1985) for  $T = 56,000, 45,000, 38,500$  and  $37,000$  K from the top to the bottom respectively. Long-dashed curve represents H II region models of McCall, Rybski, and Shields (1985). Solid curve divides AGNs from H II region like objects.

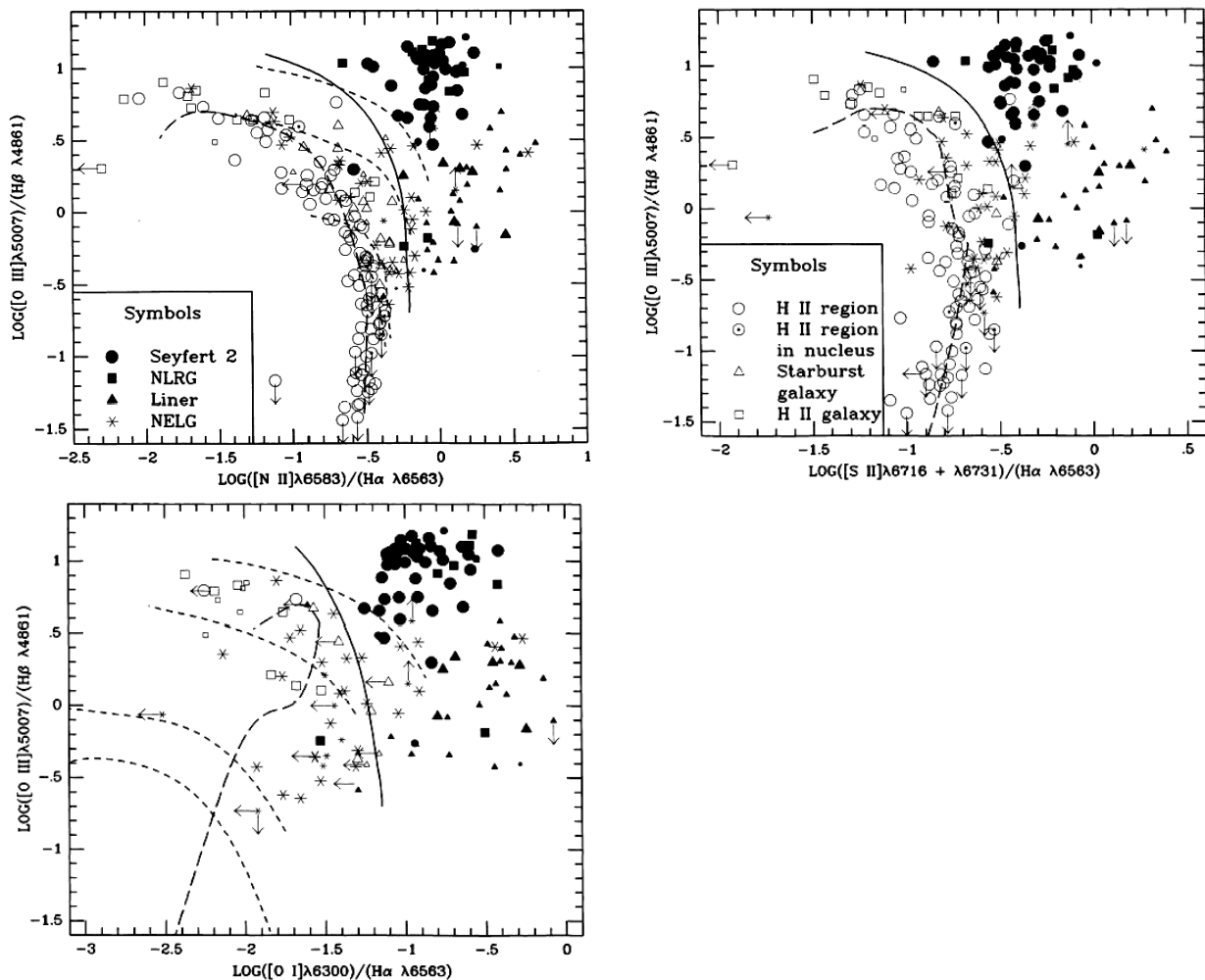


**Figure 18.** NLR diagnostic diagrams (Veilleux & Osterbrock 1987)

In **Figure 19**, similar NLR diagrams from a more recent study are presented (Kewley et al 2001). In this study, the separation between star-forming and AGN galaxies is based on the identification of the starbursts locus from detailed photoionization modelling.

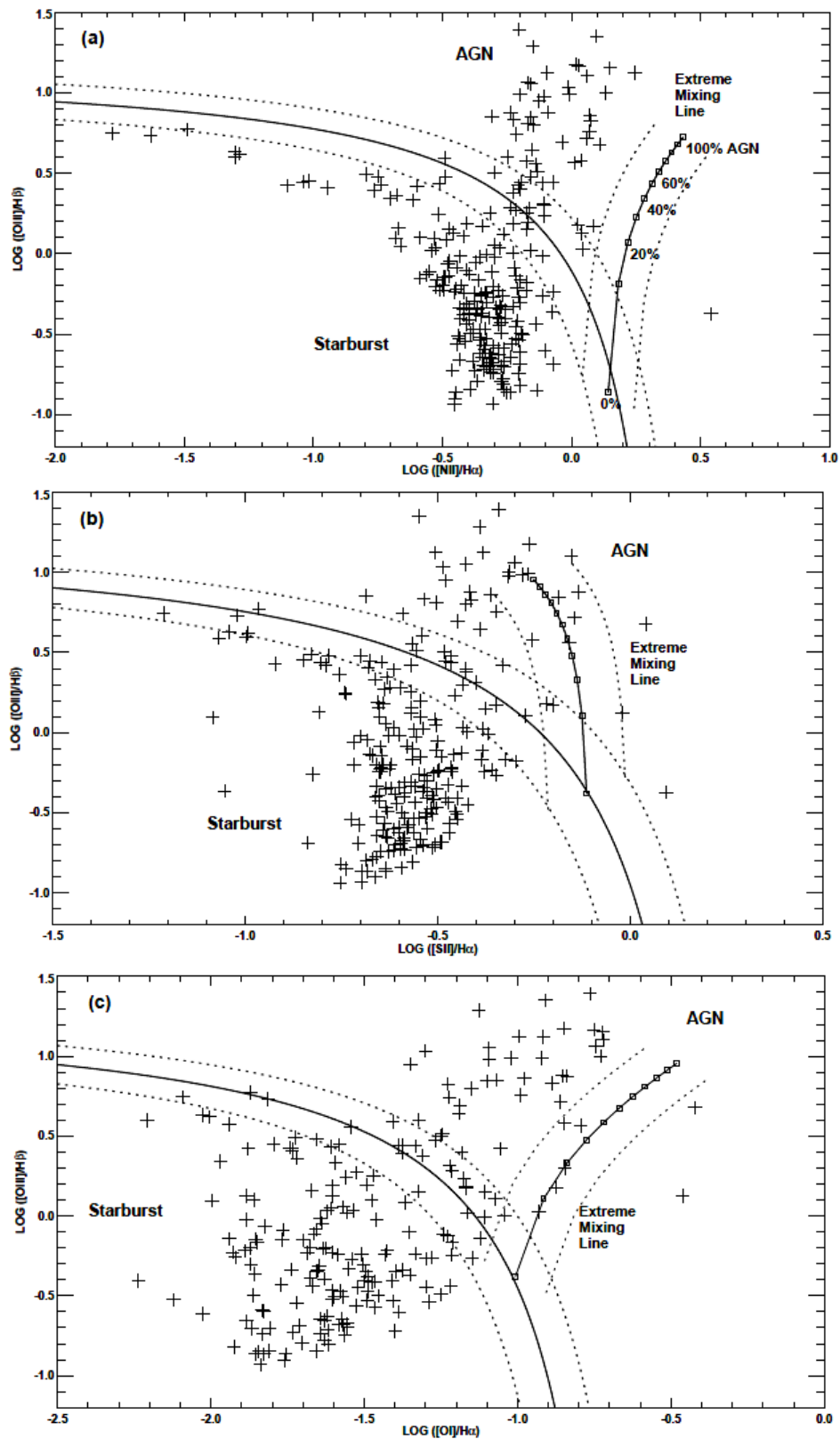


**Figure 19.** NLR diagnostic diagrams (Kewley et al 2001)

By extending the spectral range observed towards the **near-infrared** (6950 ~ 10100 Å), the number of emission lines and ions available for investigation increase. The strongest emission line in the near-infrared is [S III]  $\lambda\lambda 9069, 9531$ . Therefore it is possible to produce diagnostic diagrams (**Figure 20**) based on deep red and near infrared line ratios: [S III]  $\lambda\lambda 9069, 9531/H\alpha$ , [O II]  $\lambda\lambda 7320, 7330/H\alpha$ , [S II]  $\lambda\lambda 6716, 6731/H\alpha$ , [O III]  $\lambda 5007/H\beta$ .

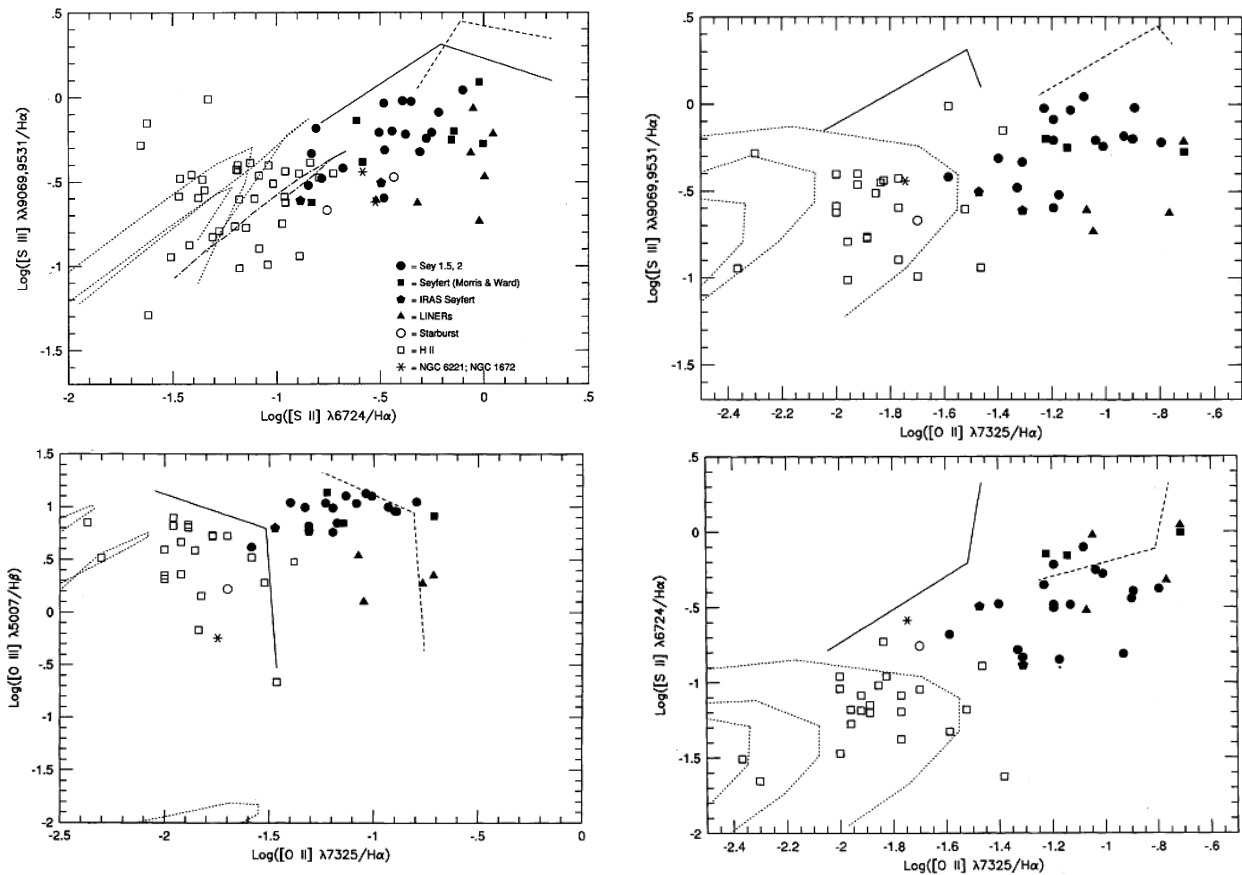


**Figure 20.** Near Infrared emission line diagnostic diagrams (Veilleux & Osterbrock 1991)

Seyfert galaxies and QSOs emit much of their radiation in the **infrared**. Furthermore, the mid-IR emission of AGNs is dominated by dust continuum re-radiating energy from black hole accretion. Diagnostic tools include mid-IR emission lines from relatively high excitation ions such as the [Ne II]  $\lambda 14.3\mu\text{m}$ , [NeV]  $\lambda 24.3\mu\text{m}$  and the [OIV]  $\lambda 25.9\mu\text{m}$  as well as the strength of the PAH (Polycyclic Aromatic Hydrocarbon) emission lines at 3.3, 6.2, 7.7, 8.7 and 11.2  $\mu\text{m}$  which are ubiquitous in normal galaxies and starbursts but suppressed in AGN. In the diagram of **Figure 21**, squares represent AGN, triangles starbursts while circles represent Ultra Luminous Infrared Galaxies (ULIRG).

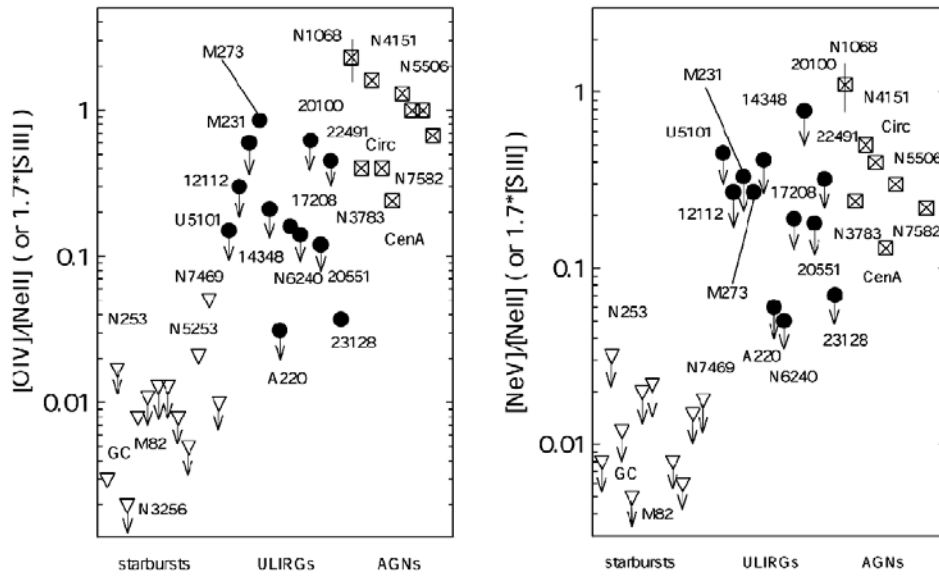


**Figure 21.** Mid-IR emission line diagnostic diagrams (Genzel et al. 2002)

## Part 2. Emission lines from accretion flow models

The fundamental question about AGNs is how the energy that is detected as radiation is generated. According to the current working model, energy is generated by gravitational infall of material which is heated to high temperatures in a dissipative accretion disk. Observations of accreting sources support the hypothesis that the accretion flow is composed of a cold medium producing thermal radiation (the geometrically thin, optical thick accretion disk thermalizes the gravitational potential energy and radiates it as a multi-temperature black body giving a characteristic bump in the spectrum) and a hot medium radiating in X-rays.

Two self consistent models describing a possible geometry of the accretion flow will be used in this work (Sobolewska et al. 2004).

- Model A: “slab” hot corona – the optically thick accretion disk truncates to a hot semi spherical inner flow
- Model B: “patchy” corona consisting of hot clouds of plasma - the optically thick accretion disk extends to the last stable orbit.

Based on the ionizing continuum from the accretion flow models we develop a photoionization modelling procedure - creating an NLR model using the CLOUDY photoionization code (Ferland et al. 1998) - and analyse the produced emission lines using the standard optical emission line diagnostic NLR diagrams. The different stages of the analysis are presented in **Figure 22**.

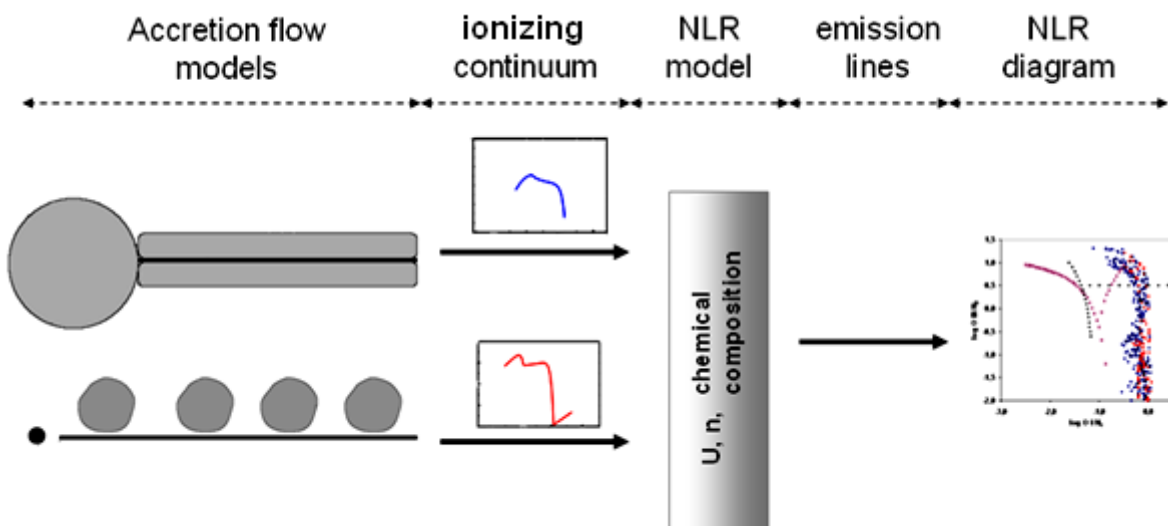


**Figure 22.** Stages of the emission lines analysis

- The **accretion flow models** are described in detail in 2.1
- The graphical representation of the **ionizing continua** emitted from the accretion flow models are presented in 2.2
- A detailed description of the parameters used for the creation of the **NLR model** using CLOUDY is presented in 2.3 while in 2.4, we evaluate the NLR model.
- Finally in 2.5 the resulting **NLR diagrams** are analysed.

## 2.1. Accretion flow models

### 2.1.1. Hot semi-spherical inner flow (Sobolewska et al. 2004)

The model examines the Optical to X-ray SED resulting from a two-component accretion flow that consists of (1) a cold, optically thick accretion disk with (2) a hot corona above it. At a radius  $r_{tr}$  greater than the radius of the innermost stable orbit,  $r_{in}$ , the disk evaporates completely to (3) a hot semi spherical inner flow.

The cold disk ( $r > r_{tr}$ ) is illuminated by both the hot inner flow and the hot corona. Part of this illuminating flux is reprocessed in the disk. Therefore, at each radius three contributions account for the total accretion disk soft flux  $F_{soft}$ : (1) viscous dissipation in the disk, (2) reprocessing of the hard coronal radiation, and (3) reprocessing of the hard radiation originating in the inner flow.

In the disk/corona region the accretion disk radiates locally as a black-body with a temperature  $T = (F_{soft}/\sigma_{SB})^{1/4}$ , where  $\sigma_{SB}$  is the Stefan-Boltzmann constant. The expected spectrum consists of a combination of black body spectra arising from regions of the disk with different temperatures and peaks in the optical-ultraviolet waveband. This local disk emission is Comptonized in the corona. The input spectrum for the Comptonization in the inner flow is determined as a superposition of local blackbodies originating in the disk at various radii.

The computed spectra are a superposition of the thermal disk radiation that escapes the hot plasma (both the corona and the inner flow) without being scattered, and the Comptonized component. The spectra are computed in a face-on view. The geometry is schematically presented in **Figure 23**. The accretion disk evaporates at a radius  $r_{tr} > r_{in}$  and forms a hot, semispherical inner flow. The total luminosity of the hot inner flow is  $L_{diss}$ . The truncated disk is covered with a hot corona at radii  $r > r_{tr}$ . At each radius  $r > r_{tr}$ , three components contribute to the soft disk flux  $F_{soft}(r)$ : a viscous dissipation in the disk; reprocessing of the hard coronal radiation; and reprocessing of the hard radiation from the inner flow,  $F_{inc}(r)$ . The spectrum is composed of (1) the soft disk blackbody-like radiation that escapes plasma without being scattered, (2) the Comptonized component in the hot corona, and (3) the Comptonized component in the hot inner flow.

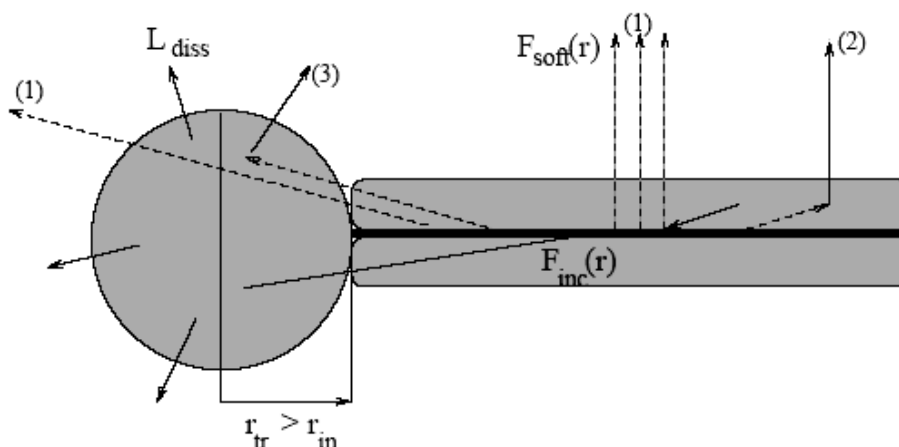


**Figure 23.** Hot semi spherical inner flow geometry (Sobolewska et al. 2004)

The model is parametrized by:

- The mass of the black hole
- The accretion rate,
- The fraction of gravitational energy dissipated in the corona
- The truncation radius
- The plasma temperature
- The accretion efficiency correction

The **mass of the black hole  $M$**  takes the values  $M = 10^6 M_{\odot}$  and  $M = 10^9 M_{\odot}$ .

The **accretion rate**, is described by the unitless quantity  $\dot{m} = \frac{\dot{M}}{\dot{M}_{Edd}}$  where  $\dot{M} = \frac{dM}{dt}$  and  $\dot{M}_{Edd}$

is the Eddington accretion rate defined as  $\varepsilon \dot{M}_{Edd} c^2 = 1.3 \times 10^{46} \frac{M}{10^8 M_{\odot}} \text{ ergs s}^{-1}$  where  $\varepsilon = 1/12$ .

The accretion rate takes the value  $\dot{m} = 0,001$

The **fraction of gravitational energy dissipated in the corona  $f$**  (strength of the corona) where it is considered that at each radius  $r > r_{tr}$ , the hot corona above the accretion disk dissipates a fraction  $f$  of the locally released gravitational energy and the remaining energy is dissipated in the disk. The fraction  $f$  takes the values:  $f = 0,1$  and  $f = 0,9$

The **truncation radius  $r_{tr}$** , at which the accretion disk evaporates to the spherical inner flow. The truncation radius takes the values:  $r_{tr} = 5 R_S$ ,  $r_{tr} = 10 R_S$ ,  $r_{tr} = 20 R_S$  where  $R_S$  is the Schwarzschild radius defined as  $R_S = 2GM_{BH}/c^2$

The **plasma temperature  $kT_e$**  is considered to be the same in both Comptonized components (corona and innerflow). It takes the value:  $kT_e = 100 \text{ keV}$ .

The **accretion efficiency correction  $\delta$** , is the fraction of energy that is dissipated in the hot inner flow (in other words is the radiation efficiency of the accretion flow). The total luminosity  $L_{diss}$  dissipated in the hot inner flow is:

$$L_{diss} = \delta L_{available}$$

$$\text{where } L_{available} = 4\pi \int_{r_{in}}^{r_{tr}} F_{visc}(r) r dr \text{ where } F_{visc}(r) = \frac{3GM\dot{M}}{8\pi r^3} \left(1 - \sqrt{\frac{r_{in}}{r}}\right).$$

The accretion efficiency correction takes the values  $\delta = 1$  where it is assumed that the hot inner flow efficiency is comparable to the disk efficiency and  $\delta = 0.12$  where it is assumed that the hot plasma located within the truncation radius  $r_{tr}$ , may form an advection dominated flow (ADAF), which was found to be several times less efficient than the accretion through the optically thick disk (Narayan, Mahadevan & Quataert 1998).

### 2.1.2. Patchy corona (Sobolewska et al. 2004)

The model examines the Optical to X-ray SED resulting from a two-component accretion flow that consists of: (1) a cold, optically thick accretion disk with (2) hot clouds of plasma (e.g. a magnetically driven “active corona”) distributed above the accretion disk extending to the last stable orbit.

The soft disk blackbody-like radiation was Comptonized in the hot plasma clouds, and the electron energy distribution in the hot plasma was thermal. The spectra are computed in a face-

on view. The geometry is schematically presented in **Figure 24**. The accretion disk extends to the last stable orbit,  $r_{in}$ . The disk is covered with hot clouds whose total luminosity accounts for  $L_{diss}$ . The spectral components are: the disk blackbody-like radiation which escapes the system without encountering the hot plasma (1), or without being scattered in the hot plasma (2), and the Comptonized component. The soft photons for Comptonization come from viscous dissipation in the disk (3) or reprocessing of the hot plasma radiation (4).

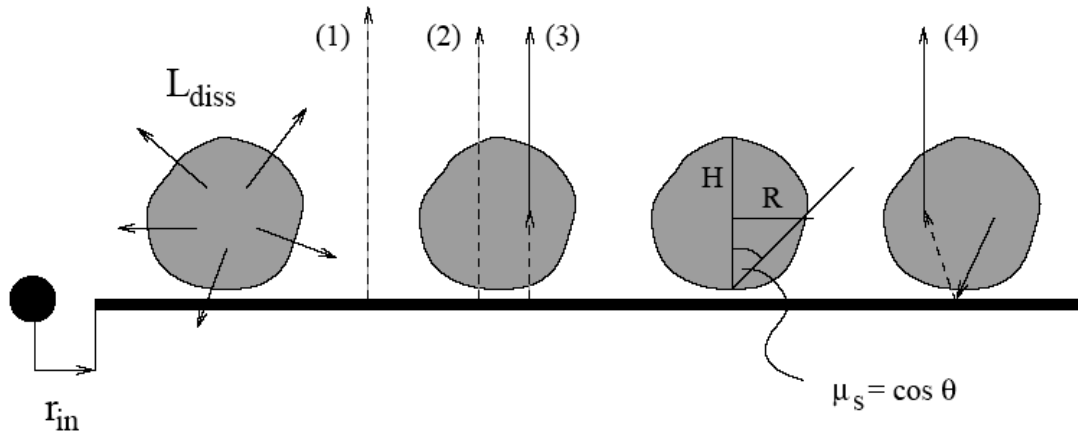


**Figure 24.** Patchy corona geometry (Sobolewska et al. 2004)

The model is parametrized by:

- the mass of the black hole
- the accretion rate
- the fraction of gravitational energy dissipated in the corona
- the plasma temperature
- the geometry of the clouds
- the disk covering factor

The **mass of the black hole  $M$**  takes the values  $6 \times 10^9 M_{\odot} < M < 5 \times 10^{10} M_{\odot}$

The **accretion rate**, is described by the unitless quantity  $\dot{m} = \frac{\dot{M}}{\dot{M}_{Edd}}$  where  $\dot{M} = \frac{dM}{dt}$  and  $\dot{M}_{Edd}$

is the Eddington accretion rate defined as  $\varepsilon \dot{M}_{Edd} c^2 = 1.3 \times 10^{46} \frac{M}{10^8 M_{\odot}} \text{ ergs s}^{-1}$  where  $\varepsilon = 1/12$ .

The accretion rate takes the values  $0,001 < \dot{m} < 1$

The **fraction of gravitational energy dissipated in the corona  $f$**  (strength of the corona) where it is considered that at each radius  $r > r_{tr}$ , the hot corona above the accretion disk dissipates a fraction  $f$  of the locally released gravitational energy and the remaining energy is dissipated in the disk. The fraction  $f$  takes the values  $0 < f < 0,9$

The **plasma temperature  $kT_e$**  takes the value:  $kT_e = 100 \text{ keV}$ .

The **geometry of the clouds  $\mu_s$** , is parametrized by their height  $H$  and radius  $R$ . The clouds are approximately spherical for  $H/R \sim 2$ , which corresponds to  $\mu_s \sim 0.7$ . For  $\mu_s \sim 0.8 - 0.95$  the clouds are vertically extended with  $H/R \sim 3-6$ . The height and radius of the clouds are of the same order for  $\mu_s \sim 0.45$ . The plane-parallel geometry corresponds to the case with  $\mu_s = 0$ . (the corona covers the whole surface of the disk) while for  $\mu_s = 1$  the clouds vanish ( $R \rightarrow 0$ ).

The **disk covering factor  $C$**  describes the fraction of the viscous disk radiation intercepted by the clouds (not all the disk radiation cools the clouds, since only a fraction of the disk surface is covered by the clouds). The disk covering factor takes the values:  $0,037 < C < 0,3$

## 2.2. Ionizing continuum

The **ionizing continua** used in this work are predicted from the accretion flow models presented in the previous section. **Figure 25** and **Figure 26** present the incident continua for the semi spherical inner flow and the patchy corona model respectively. The values of the parameters used for the prediction of each continuum are displayed in each continuum.

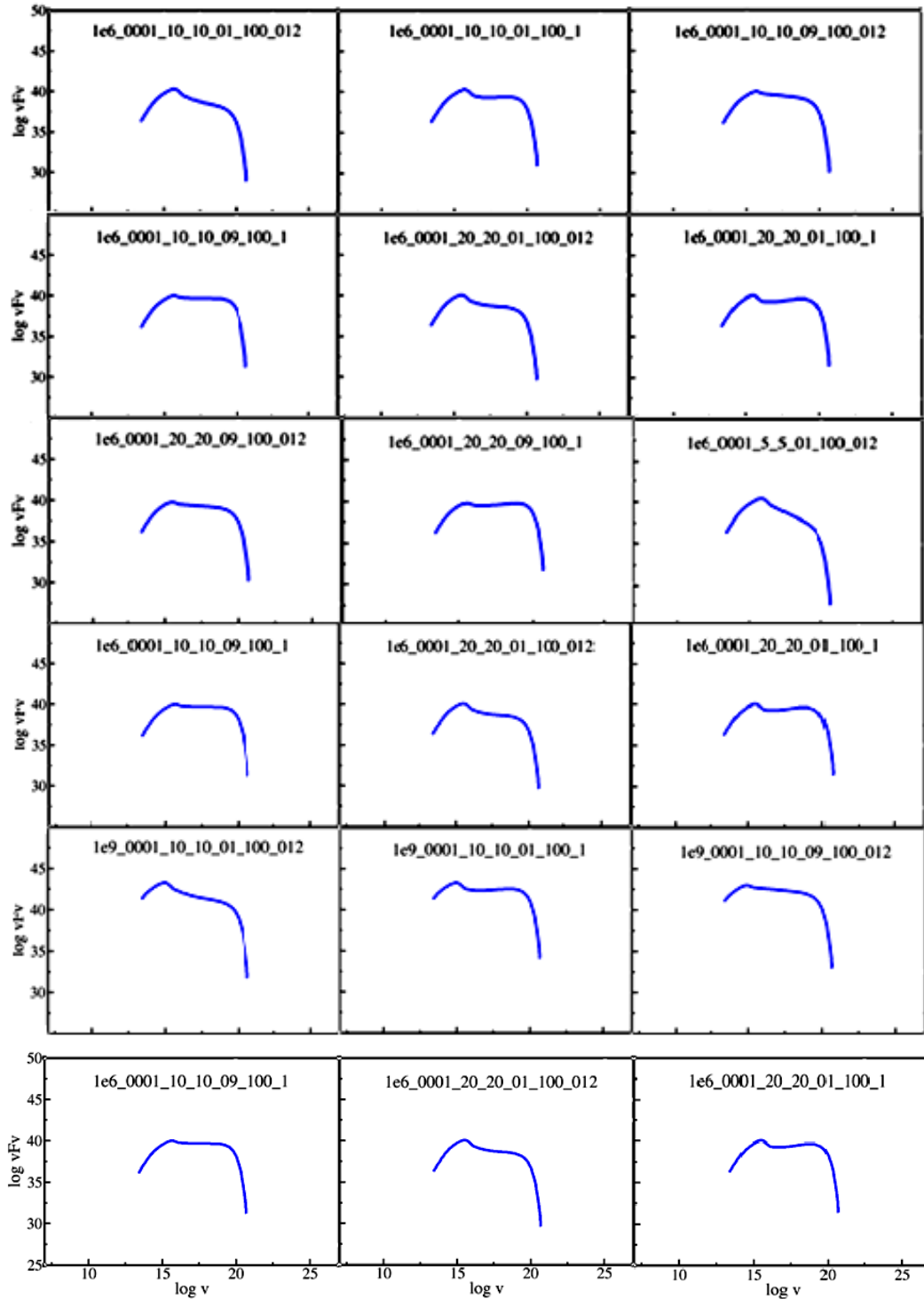


**Figure 25.** Semi spherical inner flow continua. The displayed values for:  $M_{\bullet} \dot{M}_{R_{tr} R_{tr} f_{\delta}}$

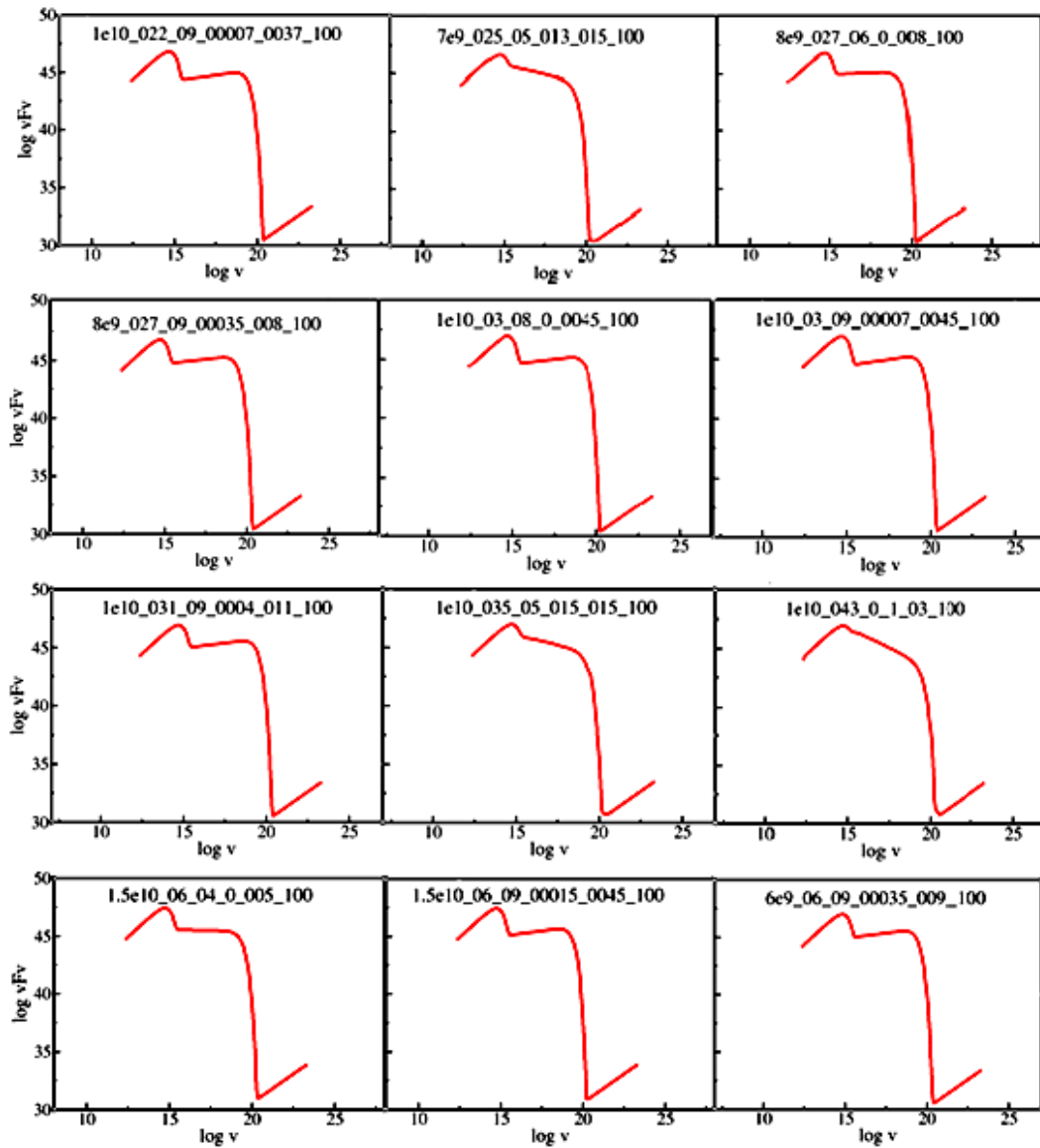
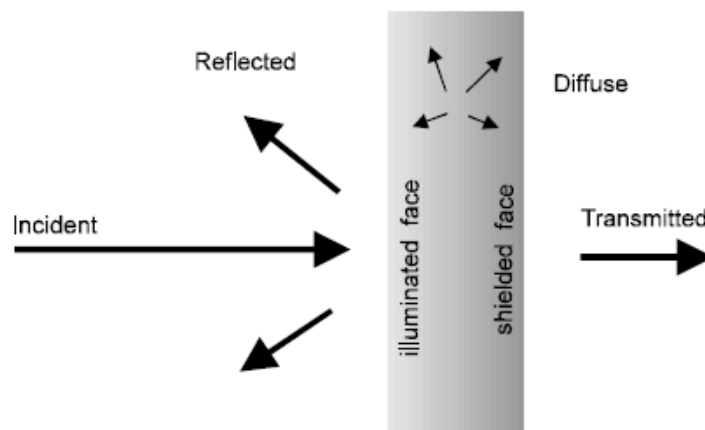


Figure 26. Patchy corona continua. The displayed values for:  $M_{\dot{m}} \cdot f_{\mu_s} \cdot C_{kTe}$

## 2.3. Creating a NLR model using CLOUDY

The ionizing continuum from the regions described in the previous section, will illuminate the NLR. In order to identify the emission lines produced from the NLR, it is necessary to create a model that will simulate the conditions in the NLR. The NLR model is realised using the CLOUDY photoionization code (Ferland et al. 1998). CLOUDY is designed to simulate emission line regions ranging from the intergalactic medium to the Broad Line Regions of Quasars. CLOUDY works by dividing a spherical nebula into a set of thin concentric shells. The shells are chosen to have thicknesses that are small enough for the physical conditions to be nearly constant within. Under these circumstances it is possible to predict the physical conditions (that is, the run of ionization, density, and temperature) of the gas, and its resulting emission-line spectrum, in a unique and self-consistent manner. This is done by simultaneously solving the equations of statistical and thermal equilibrium, equations that balance ionization-neutralization processes, and heating-cooling processes, respectively Osterbrock (1988), Aller (1984). **Figure 27** shows several of the continua computed in the calculation.



**Figure 27.** Continua that enter in the calculations in CLOUDY

**Incident continuum** is the external continuum emitted by the central object, which strikes the illuminated face of the cloud. Within the cloud the incident continuum is diminished by extinction and reprocessing. **Diffuse continuum** is the radiation field emitted by gas and grains within the nebula. **Transmitted continuum** is the net continuum emergent from the shielded face of the cloud. It includes both the attenuated incident continuum and the transferred diffuse continuum. **Reflected continuum**, is the continuum emitted from the illuminated face of the cloud in the direction towards the source of the incident continuum.

A complete NLR model requires that the following parameters be defined:

- The frequency dependence of the ionizing continuum
- The gas chemical composition
- The gas density
- The ionization parameter
- The gas pressure
- The gas temperature
- The geometry of the emission line region

The values of the parameters used for defining the NLR model are based on similar values used in other extensive studies of AGN photoionization (Hamann & Ferland 1993, Groves 2004) or on published measurements of optical emission line ratios (Ho et al. 2007)

The **ionizing continua** as predicted from the accretion flow models are presented in **Figure 25** and **Figure 26** of the previous section.

The gas **chemical composition**: The default chemical composition (metallicity) is that of the solar neighbourhood (referred as solar hereafter) and is summarized in the following **Table 2**: Apart from the solar metallicity, in the NLR model a composition that is 0.5 times solar (referred as 0.5 solar hereafter) is also examined.

			12+log	log	n/n(H)	ref
1	H	Hydrogen	12.00	0.00	1.00E+00	GS98
2	He	Helium	11.00	-1.00	1.00E-01	text
3	Li	Lithium	3.31	-8.69	2.04E-09	GS98
4	Be	Beryllium	1.42	-10.58	2.63E-11	GS98
5	B	Boron	2.79	-9.21	6.17E-10	GS98
6	C	Carbon	8.39	-3.61	2.45E-04	AP02
7	N	Nitrogen	7.93	-4.07	8.51E-05	H01
8	O	Oxygen	8.69	-3.31	4.90E-04	AP01
9	F	Fluorine	4.48	-7.52	3.02E-08	GS98
10	Ne	Neon	8.00	-4.00	1.00E-04	H01
11	Na	Sodium	6.33	-5.67	2.14E-06	GS98
12	Mg	Magnesium	7.54	-4.46	3.47E-05	H01
13	Al	Aluminium	6.47	-5.53	2.95E-06	GS98
14	Si	Silicon	7.54	-4.46	3.47E-05	H01
15	P	Phosphorus	5.51	-6.50	3.20E-07	GS98*
16	S	Sulphur	7.27	-4.74	1.84E-05	GS98*
17	Cl	Chlorine	5.28	-6.72	1.91E-07	GS98
18	Ar	Argon	6.40	-5.60	2.51E-06	GS98
19	K	Potassium	5.12	-6.88	1.32E-07	GS98
20	Ca	Calcium	6.36	-5.64	2.29E-06	GS98
21	Sc	Scandium	3.17	-8.83	1.48E-09	GS98
22	Ti	Titanium	5.02	-6.98	1.05E-07	GS98
23	V	Vanadium	4.00	-8.00	1.00E-08	GS98
24	Cr	Chromium	5.67	-6.33	4.68E-07	GS98
25	Mn	Manganese	5.46	-6.54	2.88E-07	GS98*
26	Fe	Iron	7.45	-4.55	2.82E-05	H01
27	Co	Cobalt	4.92	-7.08	8.32E-08	GS98
28	Ni	Nickel	6.25	-5.75	1.78E-06	GS98
29	Cu	Copper	4.21	-7.79	1.62E-08	GS98
30	Zn	Zinc	4.60	-7.40	3.98E-08	GS98

**Table 2.** Solar chemical composition (Grevesse & Sauval 1998),

The gas **density  $n$**  is the total hydrogen density (ionic, atomic, and molecular) at the illuminated face of the cloud. This is the sum

$$n(H) = n(H^0) + n(H^+) + 2n(H_2) + \sum_{other} n(H_{other}) [cm^{-3}]$$

In the NLR model, gas density varies from:  $10^2 \text{ cm}^{-3} < n < 10^4 \text{ cm}^{-3}$

The **ionization parameter**  $U$  is the dimensionless ratio of hydrogen-ionizing photon to total-hydrogen densities. It is defined as

$$U \equiv \frac{Q(H)}{4\pi r_0^2 n(H)c} \equiv \frac{\Phi(H)}{n(H)c}$$

where  $r_0$  is the distance [cm] between the source of ionizing radiation and the illuminated face of the cloud;  $n(H)$  [ $\text{cm}^{-3}$ ] is the total hydrogen density (ionized, neutral, and molecular);  $c$  is the speed of light;  $Q(H)$  [ $\text{s}^{-1}$ ] is the number of hydrogen-ionizing photons emitted by the central object, and  $\Phi(H)$  [ $\text{cm}^{-2} \text{ s}^{-1}$ ] is the flux of ionizing photons at the surface of the cloud. In the NLR model,  $U$  varies from:  $10^{-5} < U < 10^{-2}$

The **gas pressure** is kept constant. This includes ram, magnetic, turbulent, particle, and radiation pressure.

The **gas temperature** is set at 15.000 K (Ho et al. 2007).

The **geometry of the emission-line region** is spherical.

The parameters used for each model as well as their respective values are presented in **Table 3**.

Model	Parameter	Value
NLR	U N ( $\text{cm}^{-3}$ ) Chemical composition	$10^{-5}, 10^{-4}, 10^{-3}, 10^{-2}, 10^{-1}$ $10^2, 10^3, 10^4$ solar, 0.5 solar
Semi spherical inner flow	M ( $M_{\odot}$ ) $\dot{m}$ f $r_{\text{tr}} (R_s)$ $\delta$	$10^6, 10^9$ 0.001 0.1, 0.9 $5R_s, 10R_s, 20R_s$ 0.12, 1
Patchy corona	M ( $M_{\odot}$ ) $\dot{m}$ f $\mu_s$ C	$6 \times 10^9, 7 \times 10^9, 8 \times 10^9, 10^{10}, 5 \times 10^{10}$ 0.22, 0.25, 0.27, 0.3, 0.31, 0.35, 0.43, 0.6 0, 0.4, 0.5, 0.6, 0.8, 0.9 0, 0.0007, 0.0015, 0.0035, 0.004, 0.13, 0.15, 1 0.037, 0.045, 0.05, 0.08, 0.09, 0.11, 0.15, 0.3

**Table 3.** Accretion flow models and NLR model parameters

It is worth noting that:

- Each incident continuum illuminating the NLR model represents a different set of accretion flow model parameters.
- Each set of NLR model parameters ( $U$ ,  $n$ , chemical composition) represents a different NLR model.
- For the NLR models with  $U=10^{-5}$  the intensity of the O III  $\lambda 5007$  is too low to be displayed in the NLR diagram
- The number of NLR models is 3 ( $n$  values) x 3 ( $U$  values) x 2 (chemical composition values) = 18

## 2.4. Evaluation of the NLR model

The intensity of the emission lines produced from the illumination of the NLR model by each of the ionizing continua presented in Figure 25 and Figure 26, will be plotted in a NLR diagnostic diagram. The NLR diagram to be used will be similar to the semi empirical diagrams proposed by Veilleux - Osterbrock (Figure 18) and Kewley et al (Figure 19) and specifically those constructed from the line ratios  $\log [\text{O III}] \lambda 5007 / \text{H}_\beta \lambda 4861$  and  $\log [\text{O I}] \lambda 6300 / \text{H}_\alpha \lambda 6563$  since the  $[\text{O I}] \lambda 6300 / \text{H}_\alpha \lambda 6563$  line ratio is the most sensitive discriminator between AGN (of Seyfert type) and LINERs.

In order to proceed with the analysis we first test our photoionization modeling procedure by comparing the simulated line ratios against the starburst-AGN-LINER separating lines proposed by Veilleux-Osterbrock (VO hereafter) and Kewley as a result of the illumination of the NLR model by ionizing continua provided from:

1. CLOUDY (**Figure 28**) – a default AGN continuum used extensively for simulating NLR regions.
2. The “Atlas of Quasar Energy Distribution” (Elvis et al. 1994) (**Figure 29**).

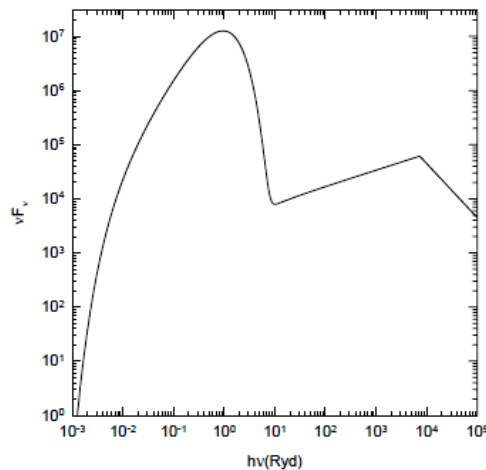


**Figure 28.** The continuum produced by the AGN command in CLOUDY (HAZY)

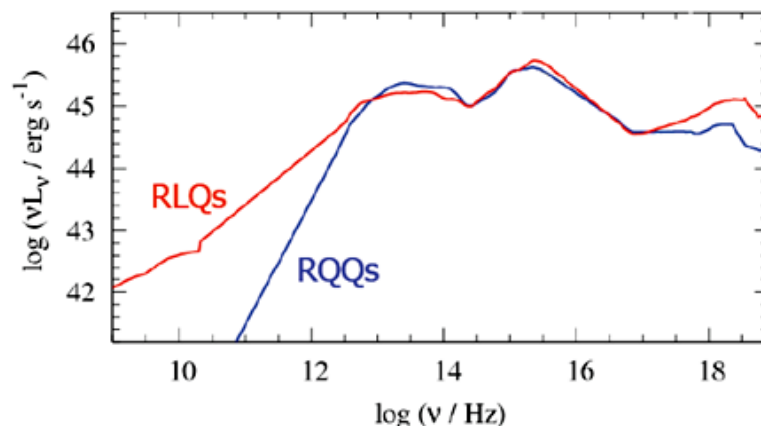


**Figure 29.** Quasar energy distribution (Elvis et al. 1994)

In both cases, apart from the incident continua, all the other model parameters are set as described in §2.3. The produced emission lines are displayed in the NLR diagrams of **Figure 30** and **Figure 31** (red dots) along with the respective tracks for different ionization parameter and gas density values (blue, red, green lines). In the same diagrams, are also displayed:

1. The separating lines of VO (black crosses) and Kewley (purple stars)
2. The distribution of objects (AGN, LINERs, H II) as derived from the observations in the optical spectroscopic survey of a large sample of nearby galaxies (Ho et al 1997).

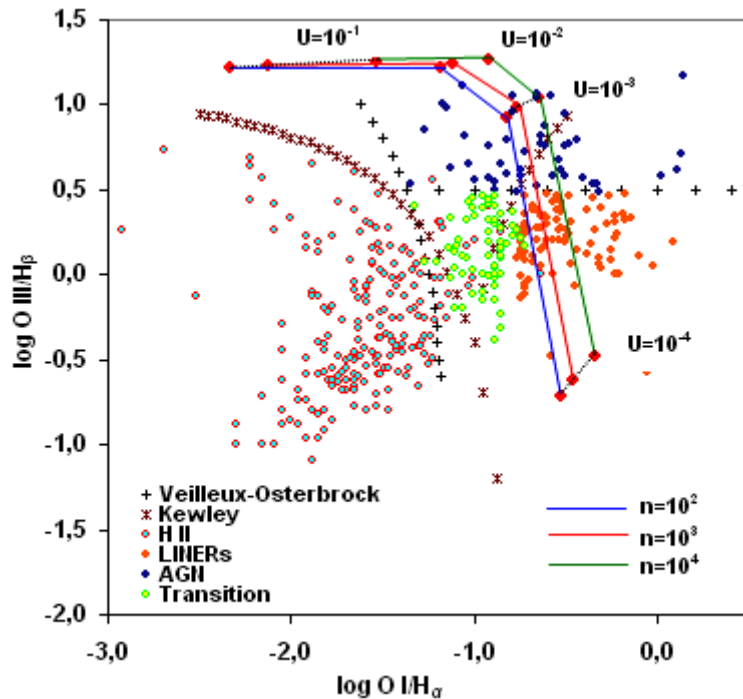


**Figure 30.** NLR model emission line tracks (CLOUDY continuum)

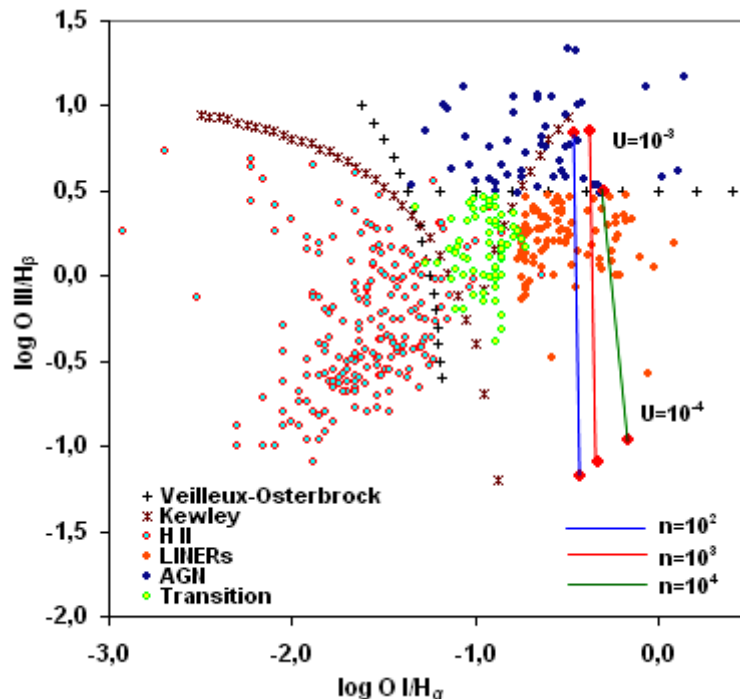


**Figure 31.** NLR model emission line tracks (Elvis continuum)

It is evident from Figure 30 and Figure 31 that for both ionizing continua, the emission line tracks from our NLR model lay within the defined areas (as defined from the VO and Kewley separating lines) for AGN and LINERs. Therefore, our photoionization NLR model produces the desired results we are confident to use it for the rest of the analysis.

## 2.5. NLR diagrams - data analysis

The following analysis presents the results from the interaction between the accretion flow models and the NLR model as displayed in NLR diagrams.

- In 2.5.1 a summary of results is presented.
- In 2.5.2 the effect of the illumination of the NLR model from the ionizing continua of the accretion flow models is investigated. This is the main part of the analysis.
- In 2.5.3 and 2.5.4 the effect of each type of ionizing continuum is discussed in detail, focusing on the correlation between the variation of the NLR model parameters ( $U$ ,  $n$ , *chemical composition*) as a function of the accretion flow model parameters ( $M$ ,  $f$ ,  $C$ , etc.).

### 2.5.1. Summary of results

The following tables present a summary of the results of our analysis

Accretion flow model: Semi spherical inner flow and Patchy corona	
Parameter	Results
All	<ul style="list-style-type: none"> <li>⇒ The produced emission line ratios and the respective area they occupy are within the defined areas for AGN and LINERs, as defined by the separating lines of Veilleux-Osterbrock and Kewley.</li> <li>⇒ It is not possible to distinguish between the accretion flow models (and consequently between the different geometries of the accretion flow region) since emission line ratios from both models occupy the same area in the NLR diagram.</li> <li>⇒ The intensity of [O I] <math>\lambda 6300</math> is systematically higher than that of the starburst-AGN separating line of VO and Kewley (shifting the occupied area to the right).</li> <li>⇒ Truncated accretion disks can also produce AGN type emission lines therefore are not associated with LINER-type AGN.</li> </ul>

**Table 4.** Summary of results → Ionization from both accretion flow models

Accretion flow model: Semi spherical inner flow	
Parameter	Results
All	<ul style="list-style-type: none"> <li>⇒ Higher values of <math>U</math> result in higher [O III] / <math>H_{\beta}</math></li> <li>⇒ The increase of <math>n</math> (gas density) does not affect the produced emission line ratios</li> <li>⇒ The variation of the chemical composition from 0.5 solar to solar increases (slightly) the intensity of [O III] <math>\lambda 5007</math></li> </ul>
$M$	⇒ The increase of $M$ does not affect the intensity of [O III] $\lambda 5007$
$R_{tr}$	<ul style="list-style-type: none"> <li>⇒ The increase of <math>R_{tr}</math> up to <math>10 R_s</math> does not affect the produced emission line ratios</li> <li>⇒ The intensity of O III <math>\lambda 5007</math> decreases for <math>R_{tr} &gt; 10 R_s</math></li> </ul>
$f$	<ul style="list-style-type: none"> <li>⇒ The intensity of [O III] <math>\lambda 5007</math> increases as <math>f</math> decreases</li> <li>⇒ For <math>f = 0.9</math> almost all emission line ratios occupy the area of LINERs</li> </ul>
$\delta$	⇒ The increase of $\delta$ does not affect the intensity of [O III] $\lambda 5007$

**Table 5.** Summary of results → Ionization from the semi spherical inner flow model

Accretion flow model: Patchy corona	
Parameter	Results
All	⇒ Higher values of $U$ result in higher $[O III] / H_{\beta}$ ⇒ The increase of $n$ (gas density) does not affect the produced emission line ratios ⇒ The variation of the chemical composition from 0.5 solar to solar increases (slightly) the intensity of $[O III] \lambda 5007$
$M$	⇒ The intensity of $[O III] \lambda 5007$ increases as $M$ increases* ⇒ For lower $M$ almost all emission line ratios occupy the area of LINERs
$\dot{m}$	⇒ The intensity of $[O III] \lambda 5007$ increases as $\dot{m}$ increases. ⇒ For lower $\dot{m}$ almost all emission line ratios occupy the area of LINERs
$f$	⇒ The intensity of $[O III] \lambda 5007$ increases as $f$ decreases ⇒ For $f > 0.5$ all emission line ratios occupy the area of LINERs
$C$	⇒ The intensity of $[O III] \lambda 5007$ increases as $C$ increases ⇒ For $C < 0.1$ all emission line ratios occupy the area of LINERs
$\mu_s$	⇒ The intensity of $[O III] \lambda 5007$ increases as $\mu_s$ increases ⇒ For $0 < \mu_s < 1$ all emission line ratios occupy the area of LINERs

\* This seems like an illusive result

**Table 6.** Summary of results → Ionization from the patchy corona model

## 2.5.2. NLR diagrams → both accretion flow models

The interaction between the accretion flow models and the produced NLR diagrams is presented in **Figure 32**.

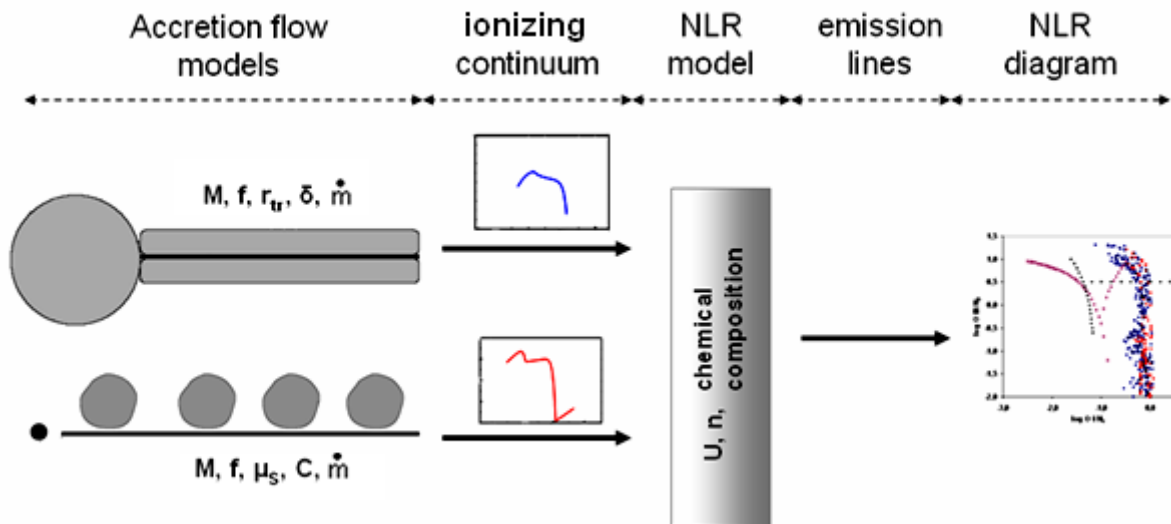


**Figure 32.** Production of NLR diagram → ionization from both accretion flow models

In the NLR diagrams that follow, the purple-stars represent the Kewley separation line and the black-crosses the VO separation line. Remarks (and the respective comments when necessary) for each NLR diagram or groups of NLR diagrams are outlined after each figure.

**Figure 33** presents the NLR diagram produced as a result of the illumination of all the NLR models from the incident continua of the semi spherical flow model (Figure 25) and the patchy corona model (Figure 26).

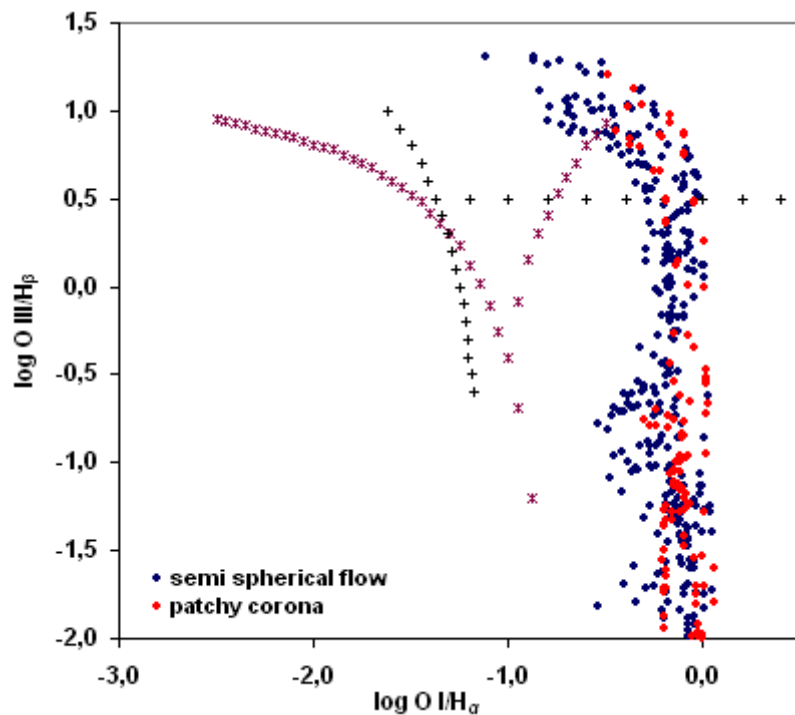


**Figure 33.** NLR diagram - all models

1. **The produced emission line ratios and the respective area they occupy are within the defined areas for AGN and LINERs, as defined by the separating lines of Veilleux-Osterbrock and Kewley**
2. **Emission line ratios from both models occupy the same area.** As a result, it is not possible to distinguish between the accretion flow models (and consequently between the different geometries of the accretion flow region)
3. **The intensity of [O I]  $\lambda 6300$  is systematically higher than that of the starburst-AGN separating line of VO and Kewley (shifting the occupied area to the right).** This is expected since the input continua in both accretion models investigated are pure AGN, while the separating lines correspond to a pure starburst continuum. In fact intermediate values of the [O I]  $\lambda 6300$  /  $H_{\alpha}$  ratio are consistent with “transition” objects (Figure 30 – yellowgreen circles) with ranging levels of relative starburst/AGN contribution. Furthermore, recent studies (Kaufman et al. 2003) imply that the separating lines of VO and Kewley between starbursts and AGN represent a very conservative lower limit on the true number of AGN. The revised separating line is shifted towards higher values of [O I]  $\lambda 6300$  in agreement with our results.
4. **The semi spherical inner flow model produces higher values of [O III]  $\lambda 5007$  /  $H_{\beta}$ , located well into the AGN area.** This is in contrast with the suggestion that LINER-type AGN could be associated with truncated accretion disks (Quataer et al. 1999) since it provides evidence that truncated accretion disks can also produce AGN type emission lines.
5. **There is a slightly wider spread of [O I]  $\lambda 6300$  /  $H_{\alpha}$  for the semi spherical inner flow model.**

**Figure 34** presents the NLR diagrams produced as a result of the variation of the NLR model parameters. One parameter is constant in each NLR diagram (the value of the parameter is displayed in the diagram) while the other NLR model parameters vary (density  $n$  in  $\text{cm}^{-3}$ ).

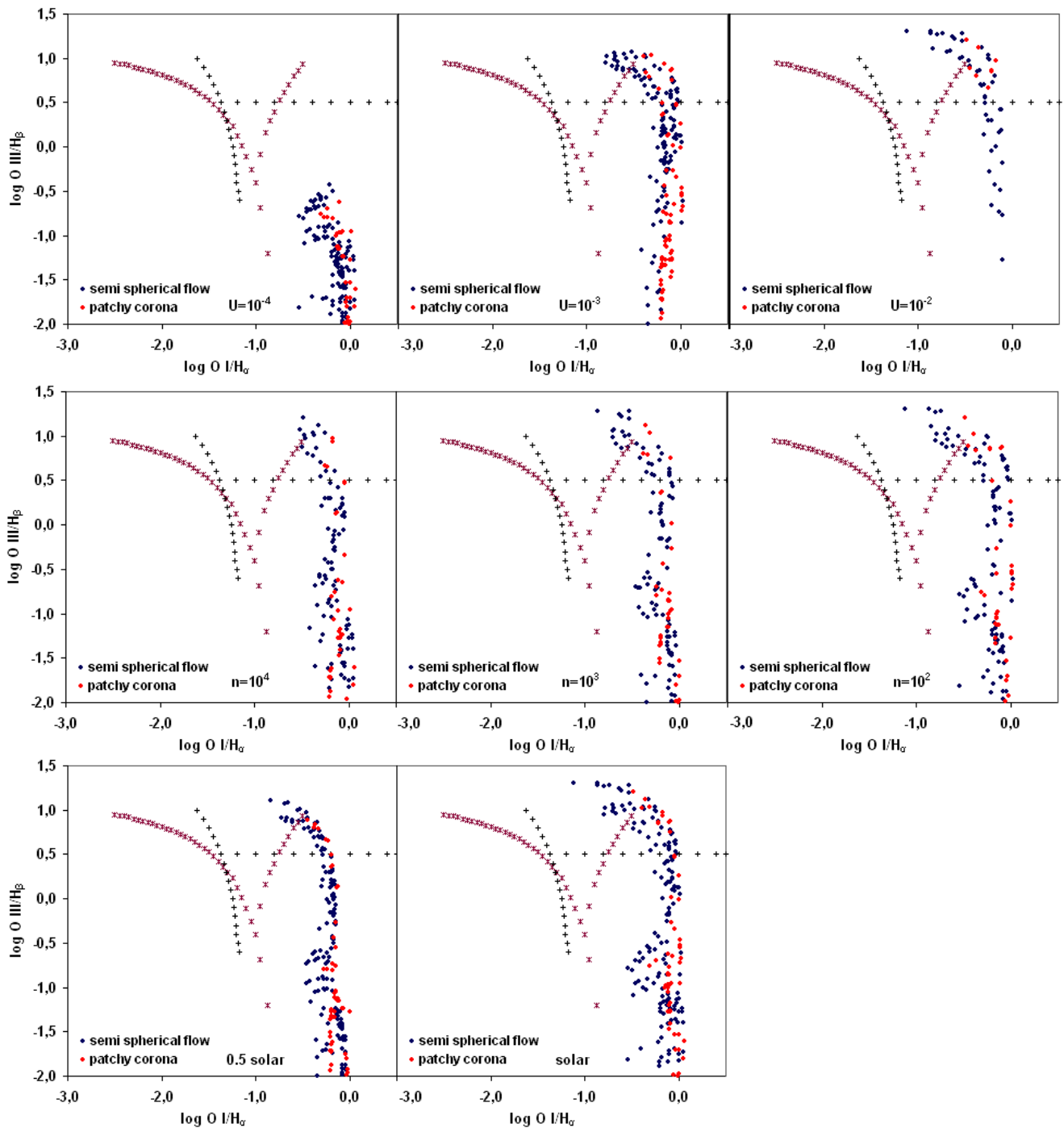


**Figure 34.** Variation of NLR model parameters

1. Higher values of  $U$  result in higher  $[O\ III] / H_{\beta}$  and  $[O\ I] / H_{\alpha}$  values
2. For  $U=10^{-3}$  and  $U=10^{-2}$  the intensity of  $[O\ III] \lambda 5007$  is higher for the semi spherical inner flow model

3. For  $U=10^{-2}$  all emission line ratios from the patchy corona model occupy the area defined for AGN (according to the VO curve). In other words, the patchy corona model illuminating a highly ionized gas is not consistent with LINER-type spectra.
4. The increase of  $n$  (gas density) does not affect the produced emission line ratios
5. The variation of the chemical composition (from 0.5 solar to solar) does not affect the produced emission line ratios. As expected, since we compare line ratios of the same species
6. The semi spherical inner flow model produces higher values of  $[\text{O III}] \lambda 5007 / \text{H}\beta$

Next we discuss the effects of each type of ionizing continuum in detail.

### 2.5.3. NLR diagrams → semi spherical inner flow model

The interaction between the semi spherical inner flow model and the produced NLR diagrams is presented in **Figure 35**.

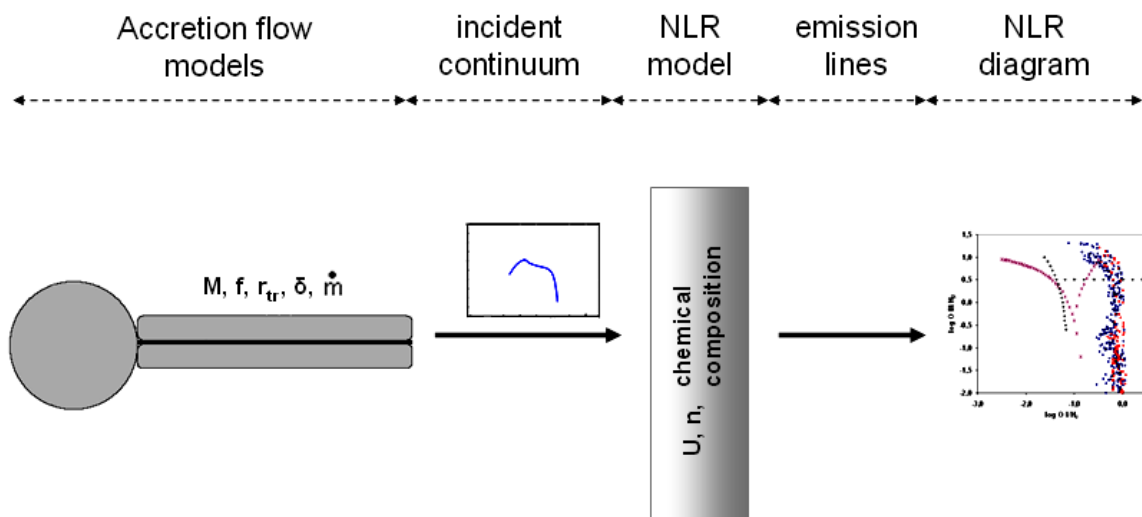


**Figure 35.** Production of NLR diagram → semi spherical inner flow model

The following figures present the NLR diagrams produced as a result of the variation of:

- the NLR model parameters ( $U, n, \text{chemical composition}$ )
- the semi spherical inner flow model parameter ( $M, f, R_{tr}, \delta$ ).

Remarks (and the respective comments when necessary) for each NLR diagram or groups of NLR diagrams are outlined after each figure.

**Figure 36** presents the variation of the NLR parameters ( $U, n, \text{chemical composition}$ ) – The emission line ratio loci for each NLR parameter are outlined on the diagrams on the right.

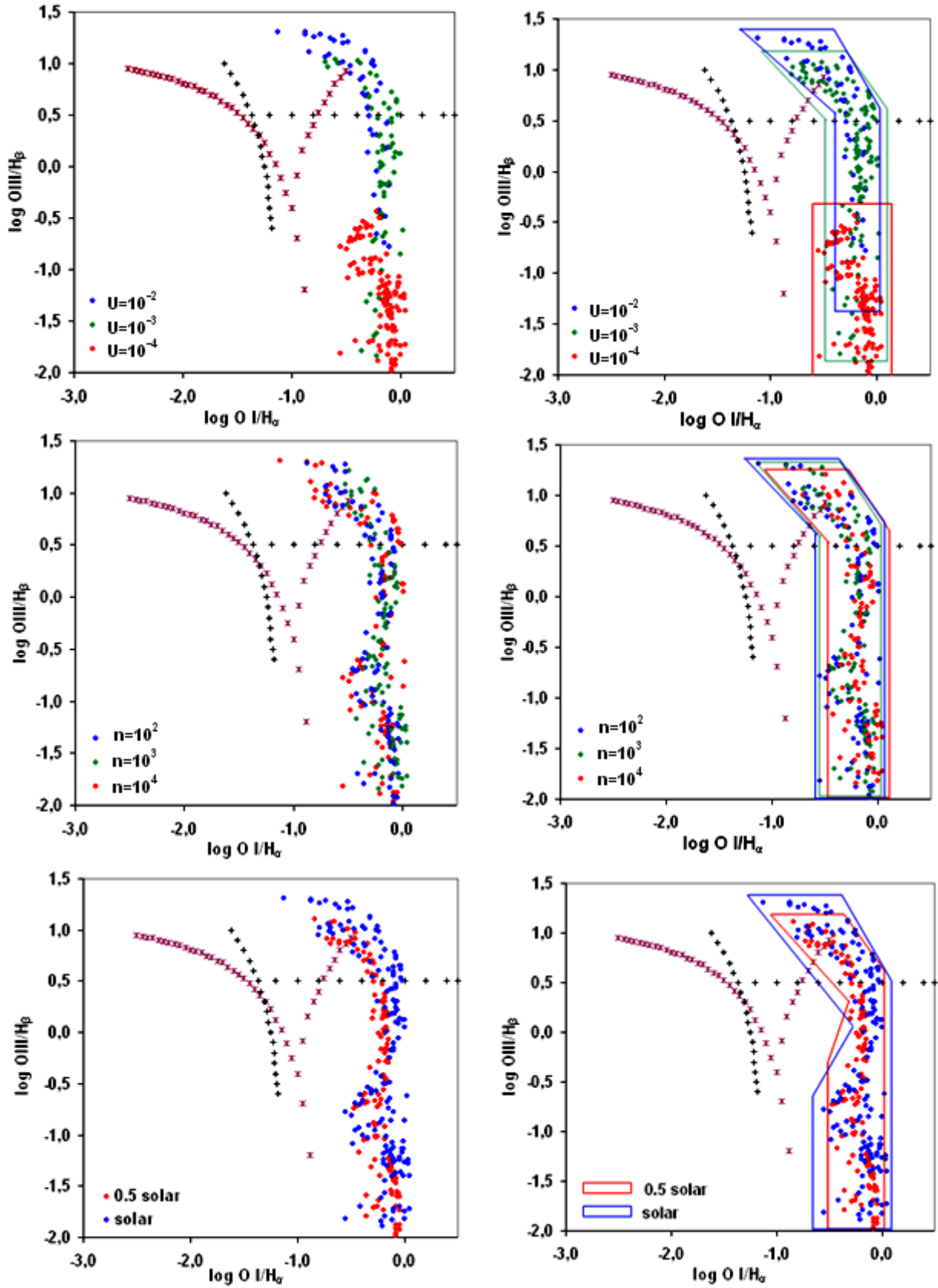


Figure 36. Semi spherical inner flow - variation of NLR model parameters

1. Higher values of  $U$  result in higher  $[\text{O III}] / \text{H}_\beta$
2. The increase of  $n$  (gas density) does not affect the produced emission line ratios
3. The variation of the chemical composition from 0.5 solar to solar increases (slightly) the intensity of  $[\text{O III}] \lambda 5007$

Figure 37 presents the effect of  $M$  (mass of the black hole) on the observed line ratios.

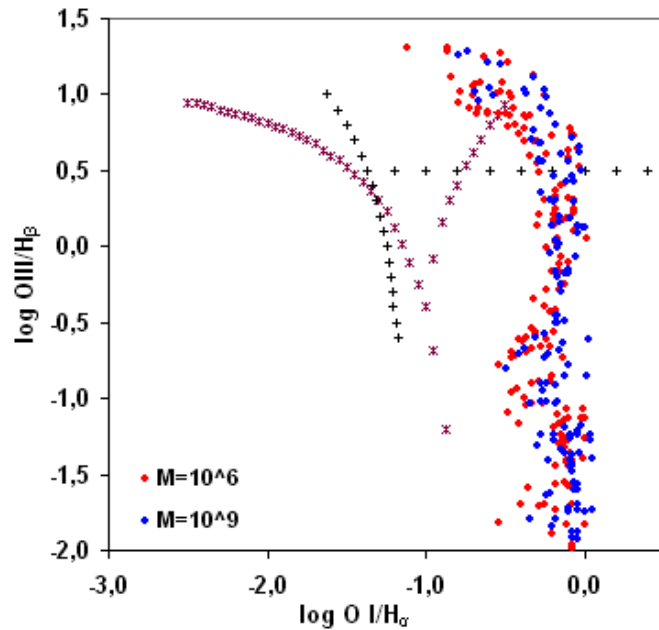
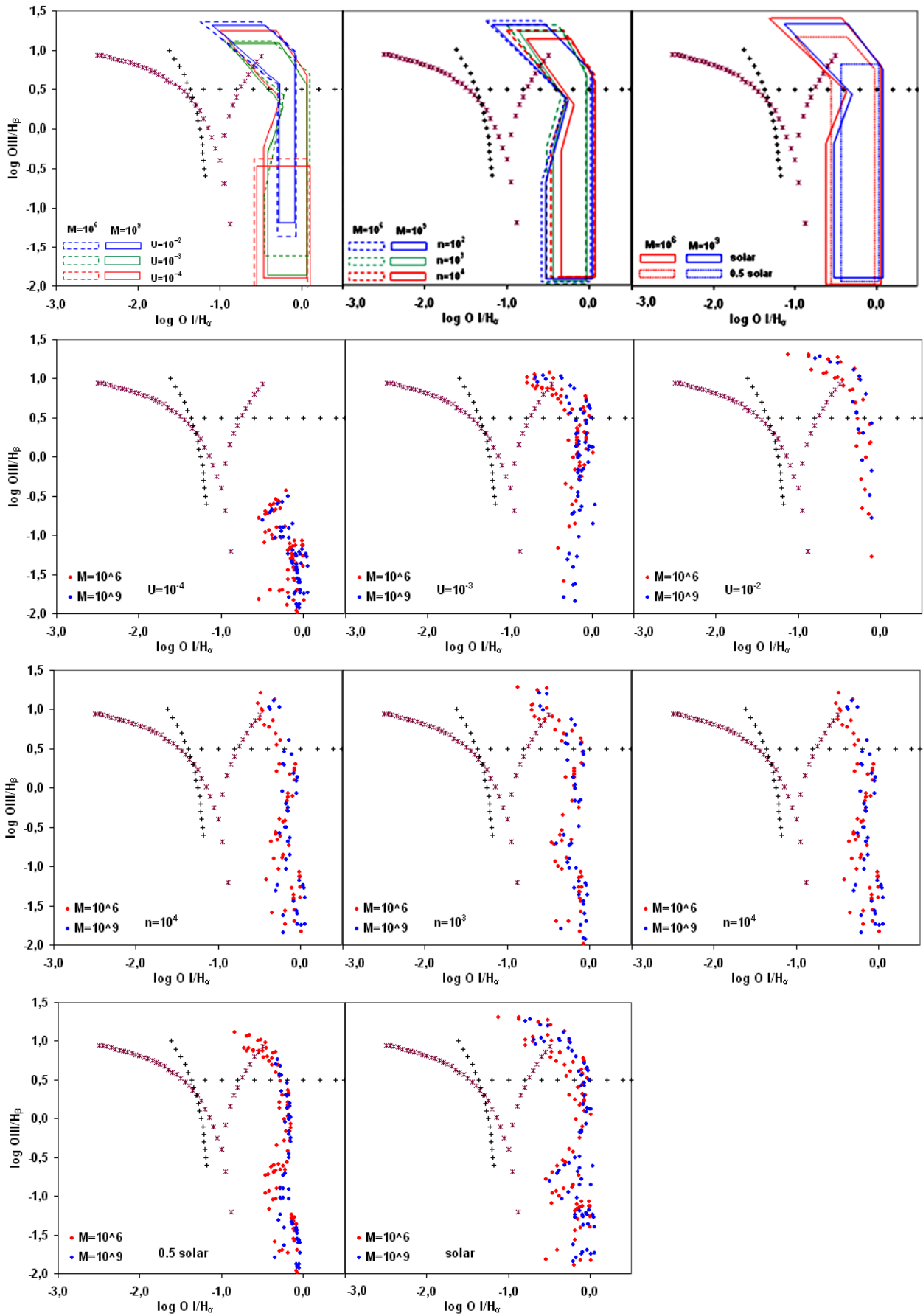


Figure 37. Semi spherical inner flow - effect of  $M$

1. The increase of  $M$  does not affect the intensity of  $[\text{O III}] \lambda 5007$

Figure 38 presents the effect of  $M$  on the variation of the NLR parameters ( $U$ ,  $n$ , chemical composition) – The emission line ratio loci for each NLR parameter are outlined on the diagrams on the first row.


 Figure 38. Semi spherical inner flow – effect of  $M$  on NLR parameters

1. As  $U$  increases, the variation of  $M$  does not affect the produced emission line ratios
2. The increase of  $n$  (gas density) does not affect the produced emission line ratios
3. The variation of the chemical composition from 0.5 solar to solar does not affect the produced emission line ratios for lower  $M$
4. For 0.5 solar chemical composition the intensity of [O III]  $\lambda 5007$  is considerably higher for lower  $M$
5. The variation of the chemical composition from 0.5 solar to solar increases the intensity of [O III]  $\lambda 5007$  for higher  $M$

Figure 39 presents the effect of  $R_{tr}$  (truncation radius) on the observed line ratios.

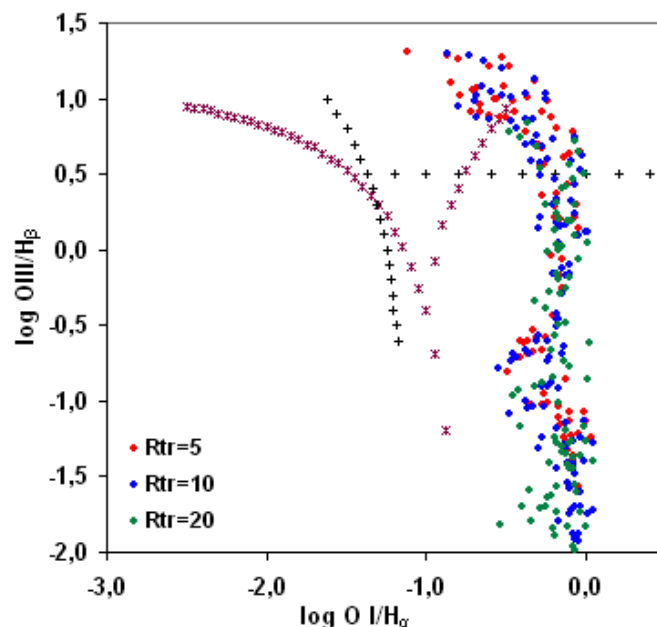


Figure 39. Semi spherical inner flow - effect of  $R_{tr}$  (in  $R_s$ )

1. The increase of  $R_{tr}$  up to  $10 R_s$  does not affect the produced emission line ratios
2. The intensity of O III  $\lambda 5007$  decreases for  $R_{tr} > 10 R_s$ . This is consistent with the considerably lower flux of the higher energy photons needed to ionize oxygen to the O III state

Figure 40 presents the effect of  $R_{tr}$  on the variation of the NLR parameters ( $U$ ,  $n$ , chemical composition) – The emission line ratio loci for each NLR parameter are outlined on the diagrams on the first row.

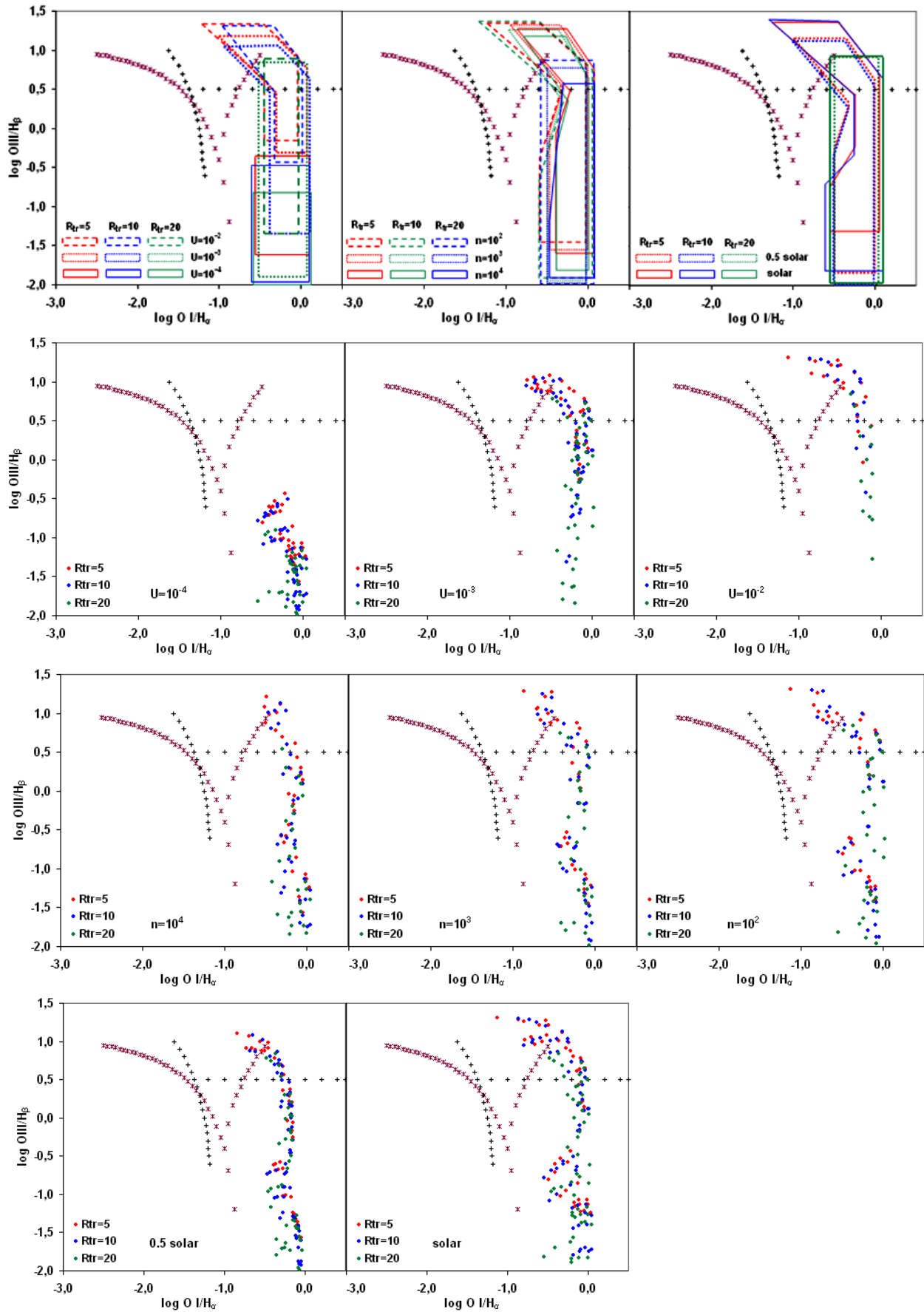


Figure 40. Semi spherical inner flow - effect of  $R_{tr}$  on NLR parameters

1. For  $U > 10^{-4}$  the intensity of [O III]  $\lambda 5007$  is higher for lower  $R_{tr}$ . This is consistent with the higher relative flux of higher energy UV photons
2. The increase of  $n$  (gas density) does not affect the produced emission line ratios
3. The variation of the chemical composition (from 0.5 solar to solar) does not affect the produced emission line ratios for  $R_{tr} = 20$
4. The variation of the chemical composition from 0.5 solar to solar increases (slightly) the intensity of [O III]  $\lambda 5007$  for lower  $R_{tr}$

Figure 41 presents the effect of  $f$  (fraction of gravitational energy dissipated in the corona) on the observed line ratios.

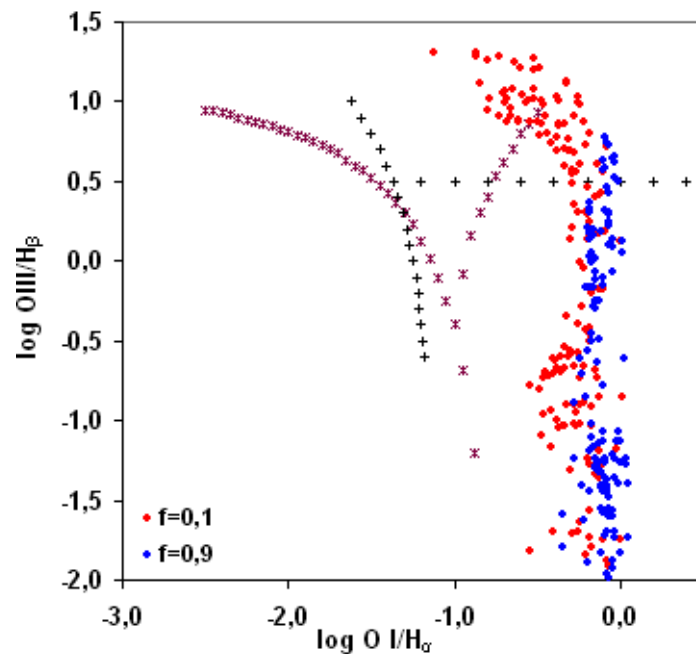
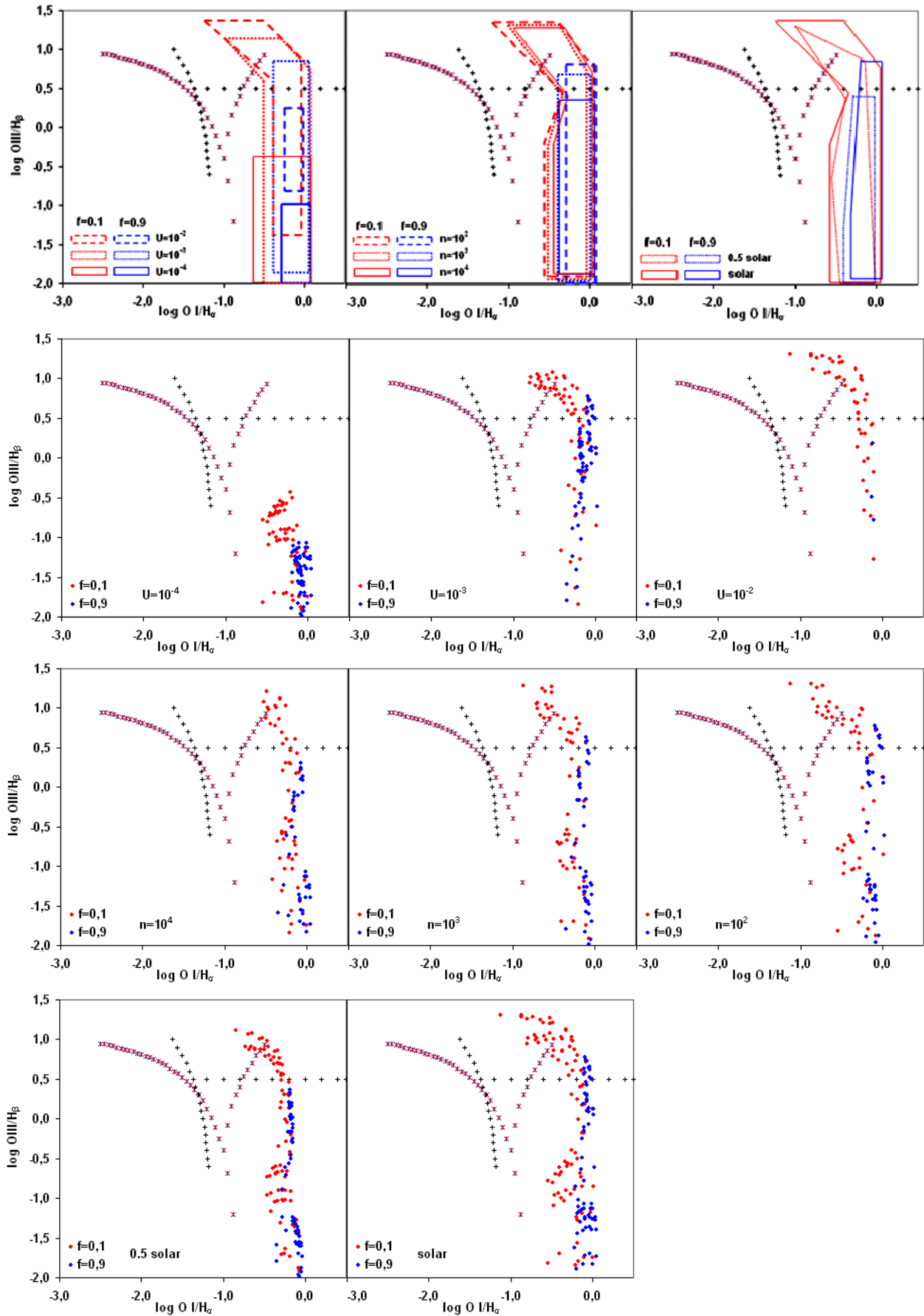


Figure 41. Semi spherical inner flow - effect of  $f$

1. The intensity of [O III]  $\lambda 5007$  increases as  $f$  decreases
2. For  $f = 0.9$  almost all emission line ratios occupy the area of LINERs

Figure 42 presents the effect of  $f$  on the variation of the NLR parameters ( $U$ ,  $n$ , chemical composition) –The emission line ratio loci for each NLR parameter are outlined on the diagrams on the first row.


 Figure 42. Semi spherical inner flow - effect of  $f$  on NLR parameters

1. For  $U < 10^{-2}$  the intensity of [O III]  $\lambda 5007$  is higher for lower  $f$
2. For  $U = 10^{-2}$  almost all emission line ratios are produced from  $f = 0.1$ . The few emission line ratios produced from  $f = 0.9$  occupy the LINERs area.
3. The increase of  $n$  (gas density) does not affect the produced emission line ratios
4. The variation of the chemical composition from 0.5 solar to solar increases (slightly) the intensity of [O III]  $\lambda 5007$ .

Figure 43 presents the variation of  $\delta$  (accretion efficiency correction) on the observed line ratios.

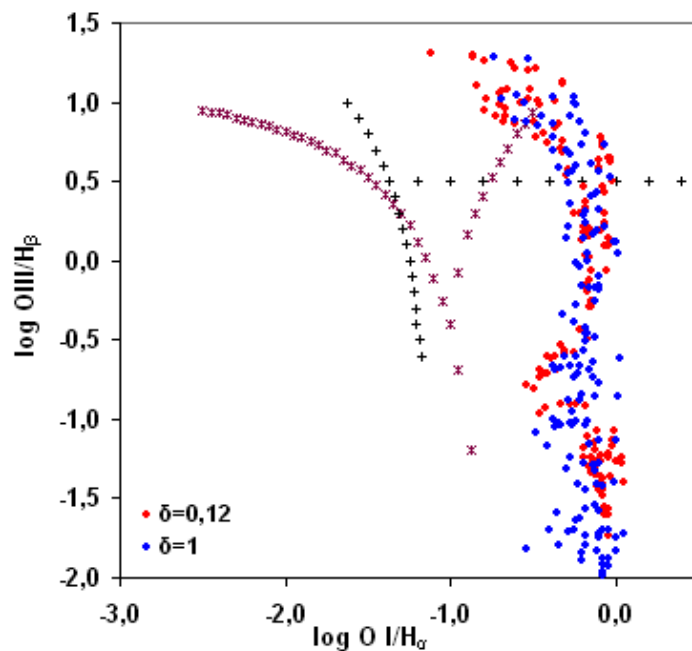


Figure 43. Semi spherical inner flow - effect of  $\delta$

1. The increase of  $\delta$  does not affect the intensity of [O III]  $\lambda 5007$

Figure 44 presents the variation of  $\delta$  in relation with the variation of the NLR parameters ( $U$ ,  $n$ , chemical composition) – The emission line ratio loci for each NLR parameter are outlined on the diagrams on the first row.

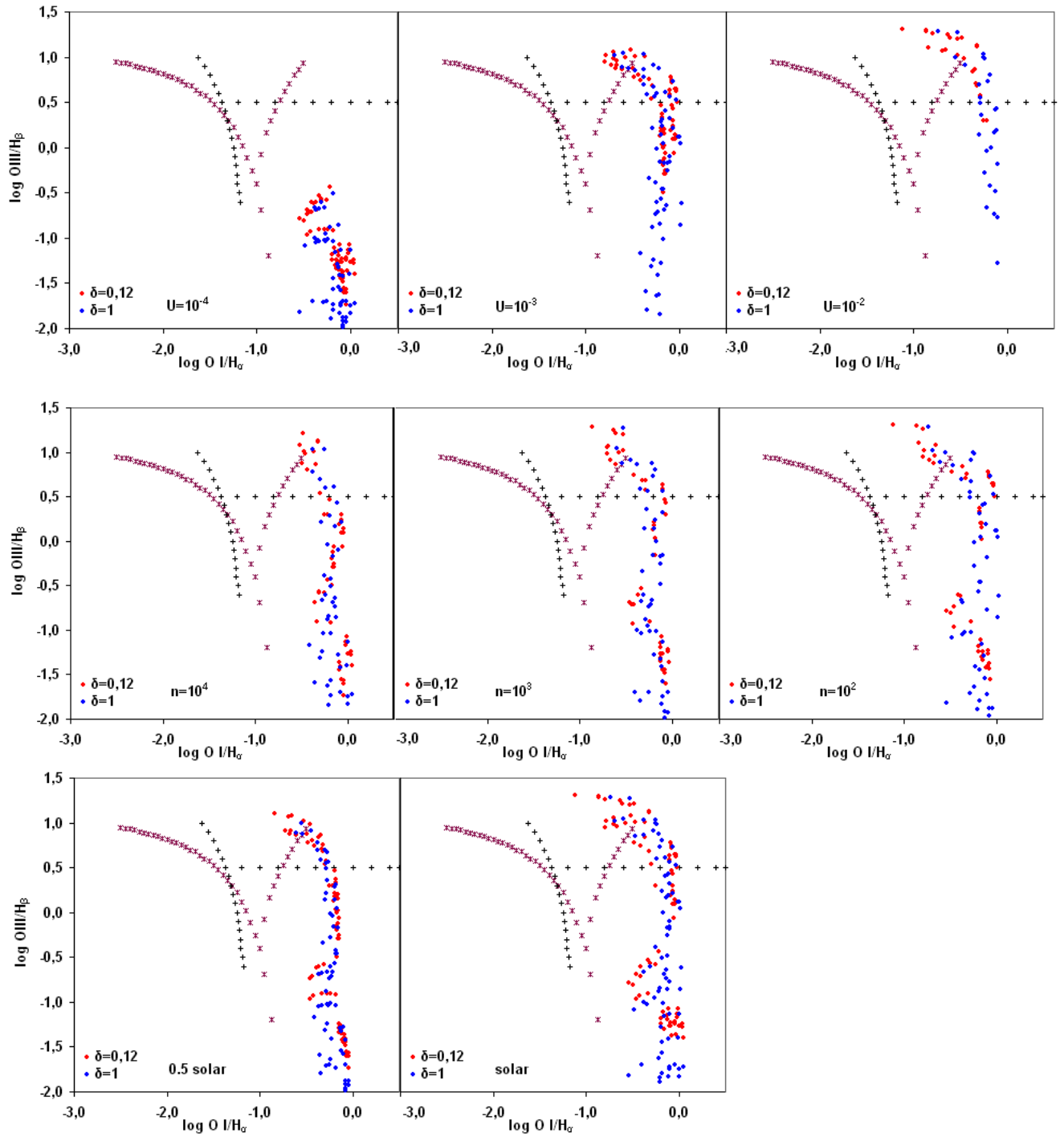
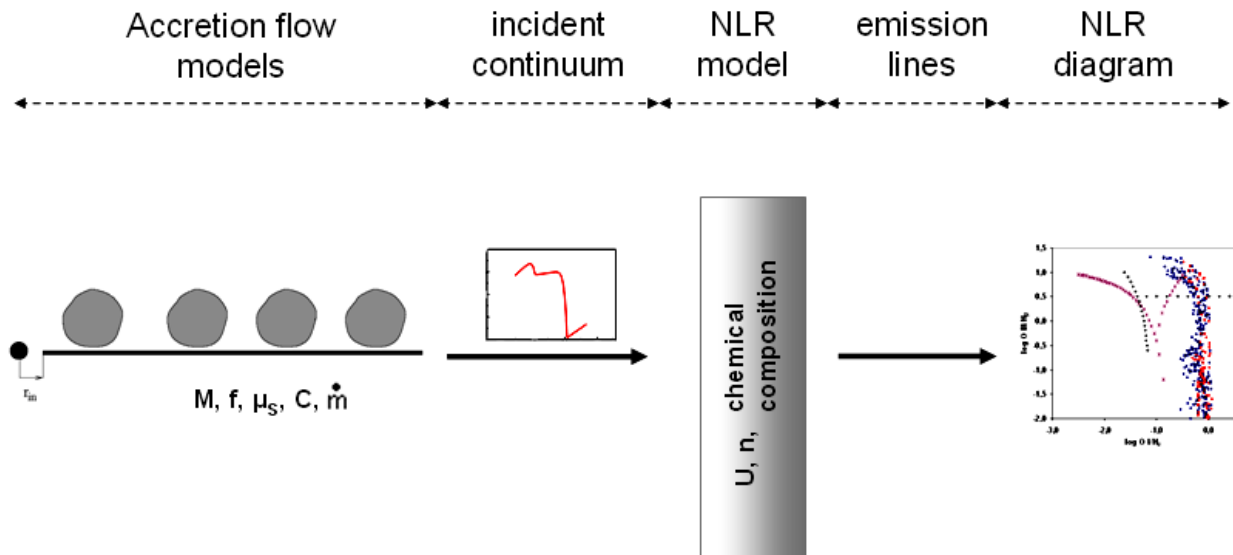


Figure 44. Semi spherical inner flow - effect of  $\delta$  on NLR parameters

1. The increase of  $\delta$  does not affect the intensity of  $[O III] \lambda 5007$

### 2.5.4. NLR diagrams → patchy corona flow model

The interaction between the patchy corona flow model and the produced NLR diagrams is presented in **Figure 45**.



**Figure 45.** Production of NLR diagram → patchy corona model

The following figures present the NLR diagrams produced as a result of the variation of:

- the NLR model parameters (U, n, chemical composition)
- the patchy corona model parameter ( $M, \dot{m}, f, \mu_s, C$ ).

Remarks (and the respective comments when necessary) for each NLR diagram or groups of NLR diagrams are outlined after each figure.

**Figure 46** presents the variation of the NLR parameters (U, n, chemical composition) – The emission line ratio loci for each NLR parameter are outlined on the diagrams on the right.

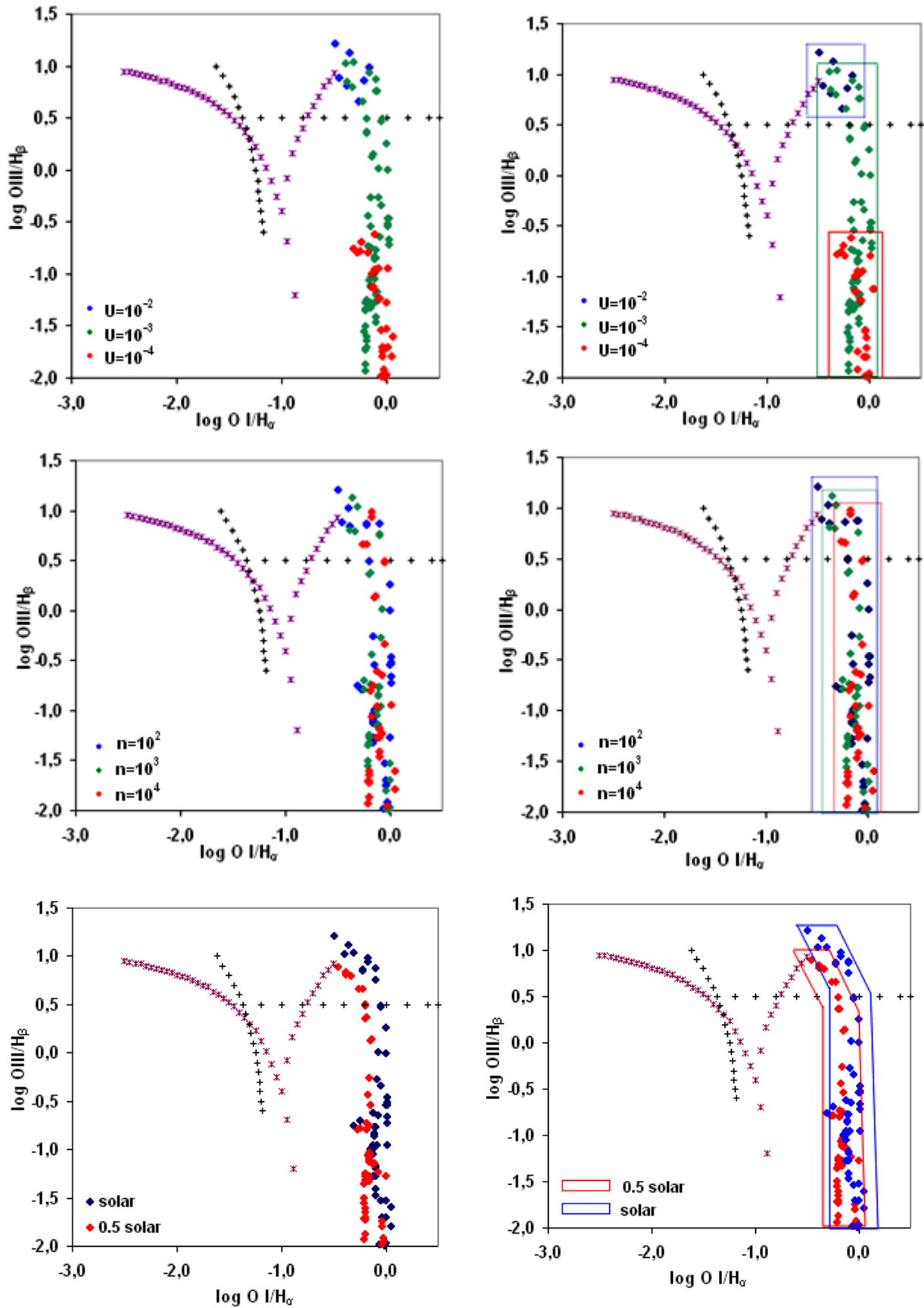


Figure 46. Patchy corona - variation of NLR model parameters

1. Higher values of  $U$  result in higher  $[\text{O III}] / \text{H}\beta$
2. The increase of  $n$  (gas density) does not affect the produced emission line ratios
3. The variation of the chemical composition from 0.5 solar to solar increases (slightly) the intensity of  $[\text{O III}] \lambda 5007$

Figure 47 presents the effect of  $M$  (mass of the black hole) on the observed line ratios.

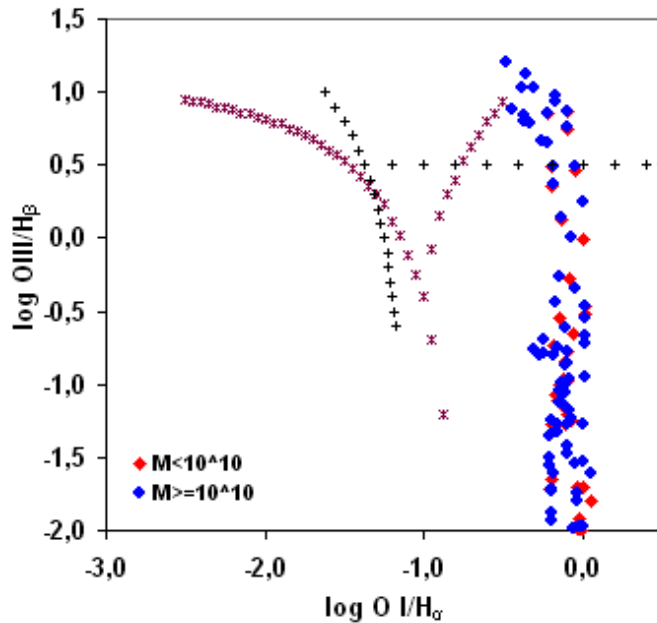
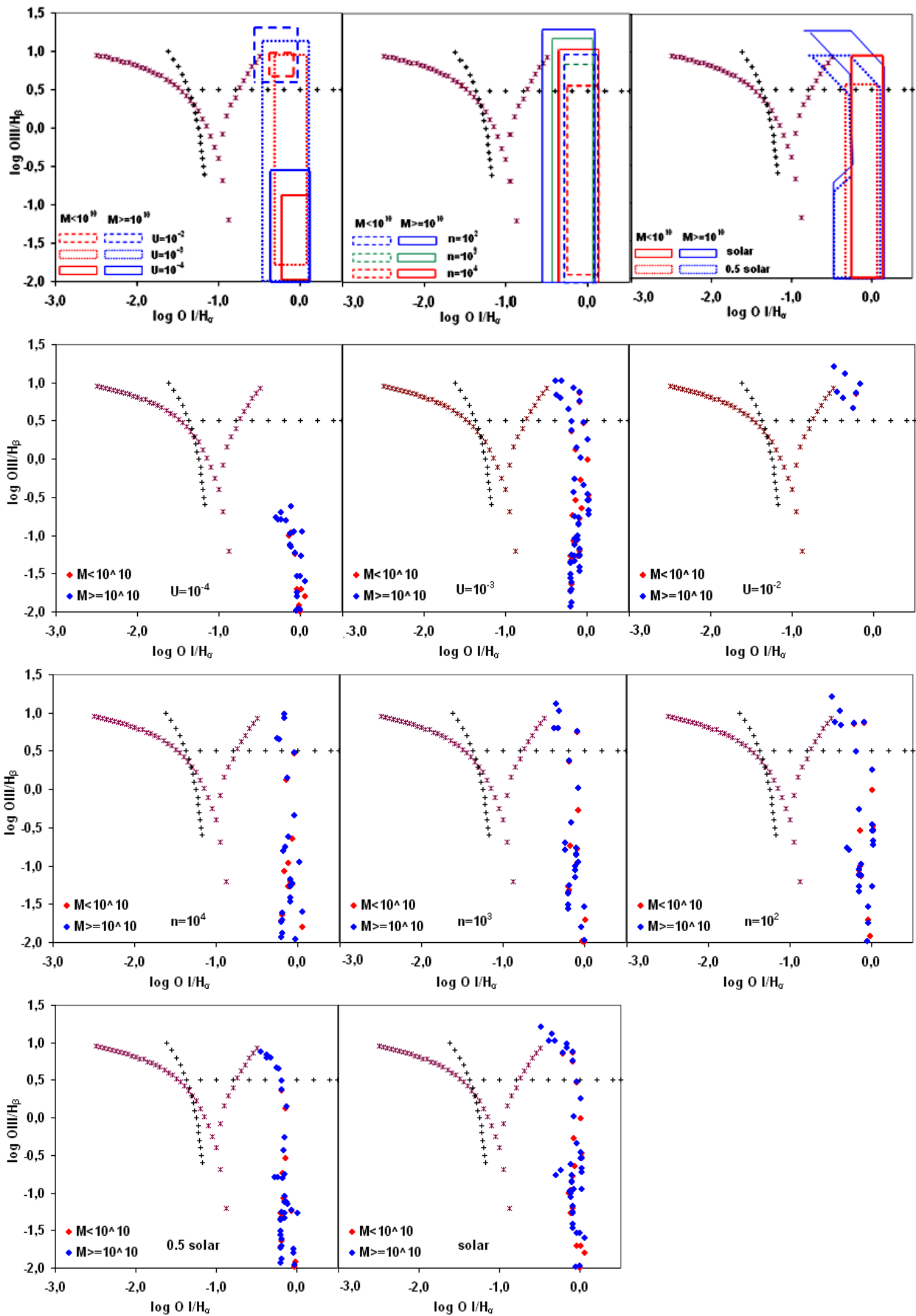


Figure 47. Patchy corona - effect of  $M$

1. **The intensity of  $[\text{O III}] \lambda 5007$  increases as  $M$  increases.** This is quite surprising, since the increase in  $M$  should result in lower intensity of  $[\text{O III}] \lambda 5007$  (as identified in the semi spherical inner flow model). This seems like an illusive result and is probably due to the small difference between the masses of the ionizing continua (the difference is less than a magnitude while in the semi spherical inner flow model is three).
2. **For lower  $M$  almost all emission line ratios occupy the area of LINERs**

Figure 48 presents the variation of  $M$  on the variation of the NLR parameters ( $U$ ,  $n$ , chemical composition) – The emission line ratio loci for each NLR parameter are outlined on the diagrams on the first row.



**Figure 48.** Patchy corona - effect of M on NLR parameters

1. The intensity of [O III]  $\lambda$ 5007 increases as M increases
2. For  $U=10^{-2}$  almost all emission line ratios are produced from higher M.
3. The increase of  $n$  (gas density) does not affect the produced emission line ratios
4. The variation of the chemical composition from 0.5 solar to solar increases (slightly) the intensity of [O III]  $\lambda$ 5007

Figure 49 presents the variation of  $\dot{m}$  (accretion rate) on the observed line ratios.

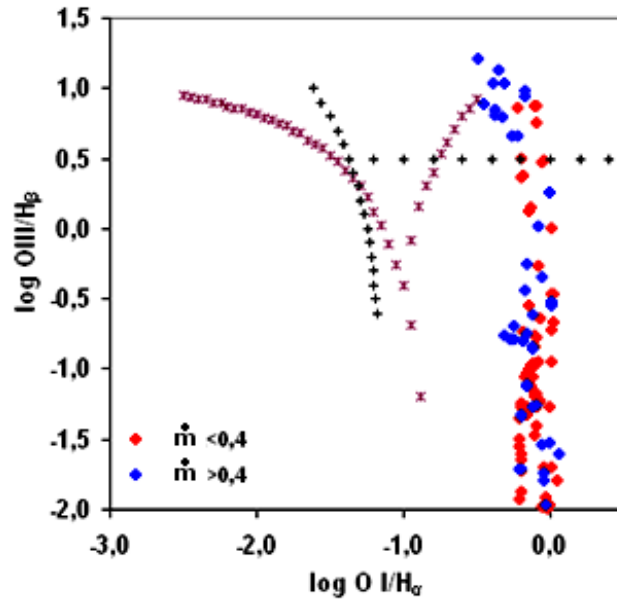
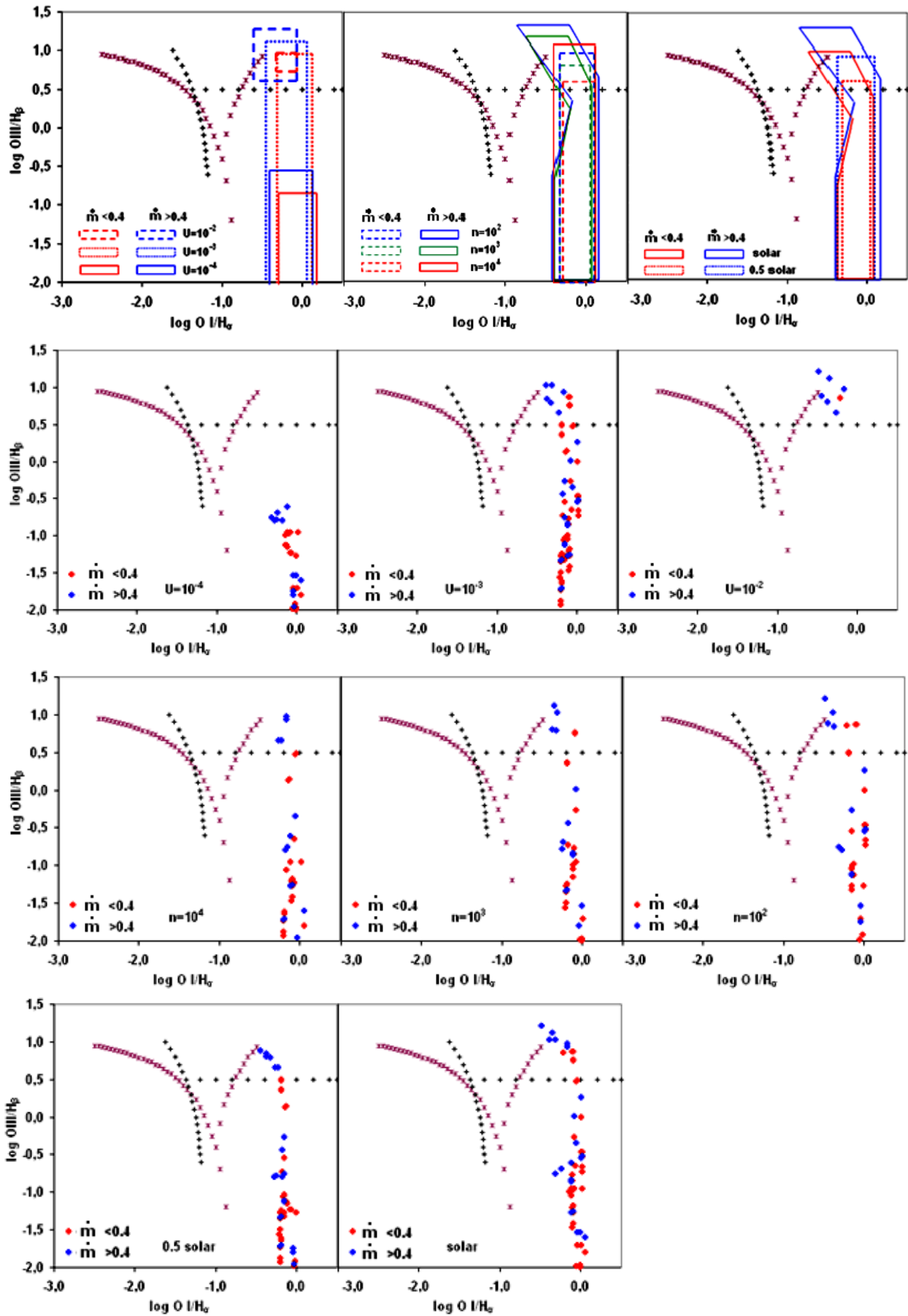


Figure 49. Patchy corona - effect of  $\dot{m}$

1. The intensity of [O III]  $\lambda$ 5007 increases as  $\dot{m}$  increases. This is expected since higher  $\dot{m}$  results in more energy on the accretion disk and as a consequence stronger disk emission (higher relative strength of the “big blue bump” in UV).
2. For lower  $\dot{m}$  almost all emission line ratios occupy the area of LINERs

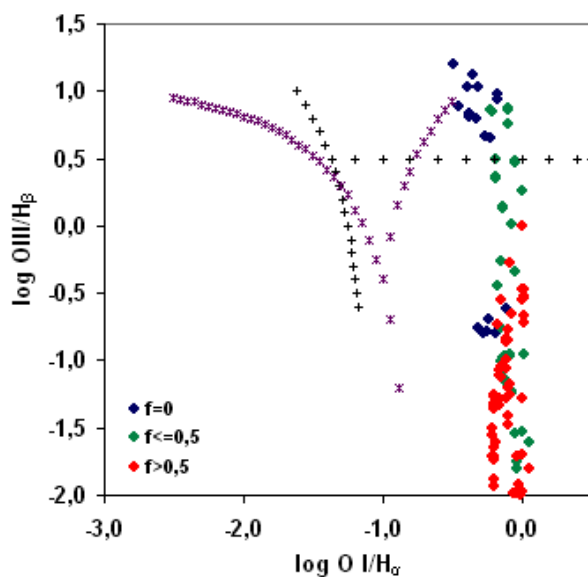
Figure 50 presents the effect of  $\dot{m}$  on the variation of the NLR parameters ( $U$ ,  $n$ , chemical composition) – The emission line ratio loci for each NLR parameter are outlined on the diagrams on the first row.



**Figure 50.** Patchy corona - effect of  $\dot{m}$  on NLR parameters

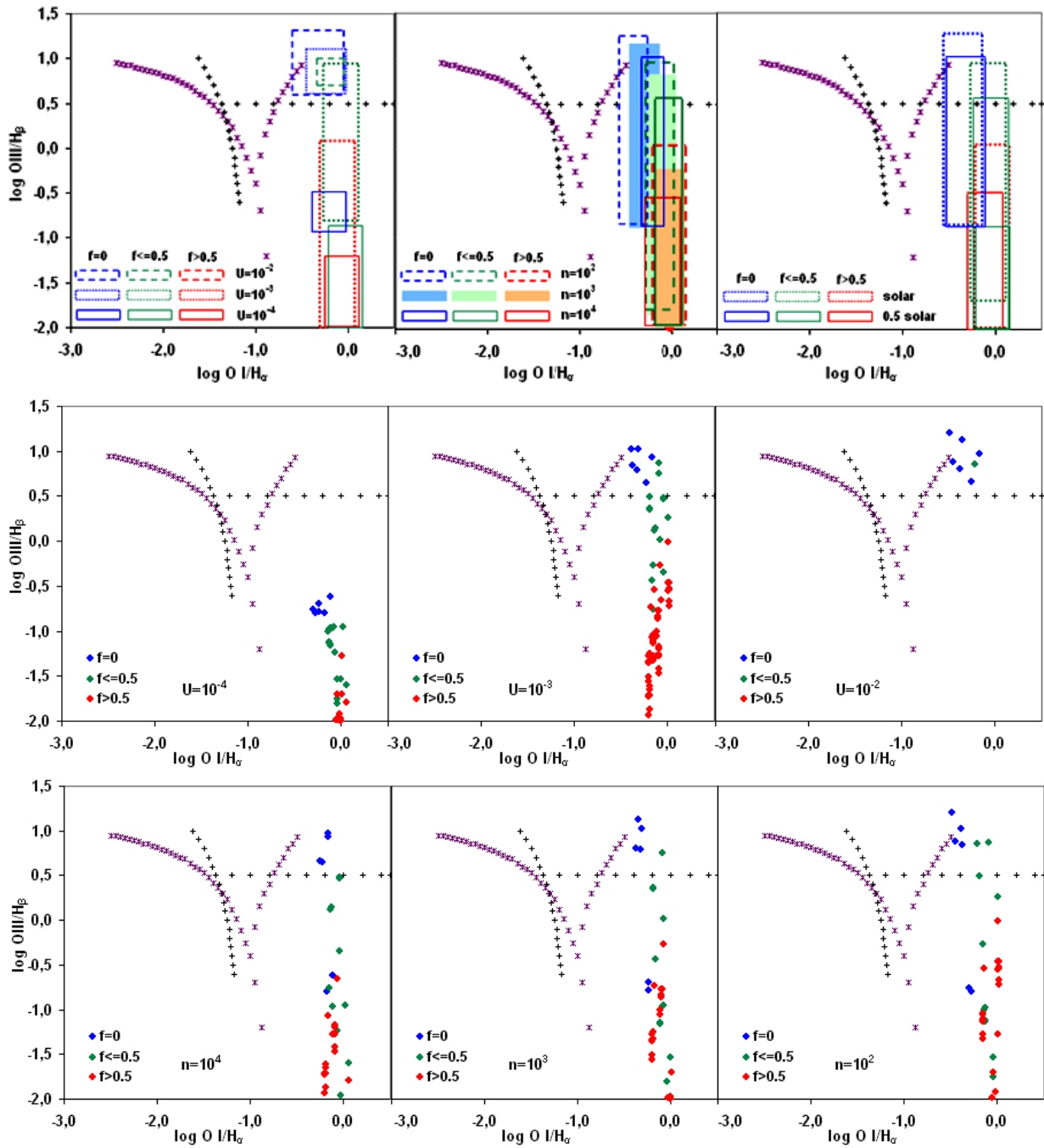
1. **As  $U$  increases, the intensity of [O III]  $\lambda$ 5007 is higher for  $\dot{m} > 0.4$**
2. **For  $U=10^{-2}$  almost all emission line ratios are produced from  $\dot{m} > 0.4$ .**
3. **The increase of  $n$  (gas density) does not affect the produced emission line ratios**
4. **The variation of the chemical composition from 0.5 solar to solar increases (slightly) the intensity of [O III]  $\lambda$ 5007**

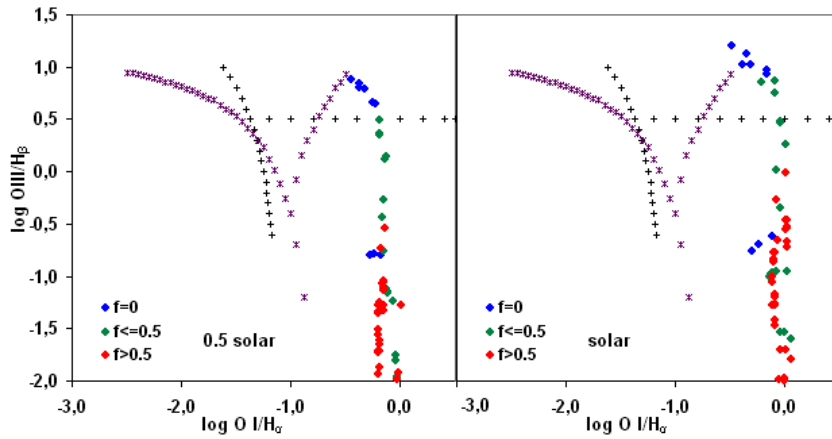
**Figure 51** presents the effect of  $f$  (fraction of gravitational energy dissipated in the corona) on the observed line ratios.


**Figure 51.** Patchy corona - effect of  $f$ 

1. **The intensity of [O III]  $\lambda$ 5007 increases as  $f$  decreases** This is expected since lower  $f$  results in more energy on the accretion disk and as a consequence stronger disk emission (higher relative strength of the “big blue bump” in UV).
2. **For  $f > 0.5$  all emission line ratios occupy the area of LINERs**

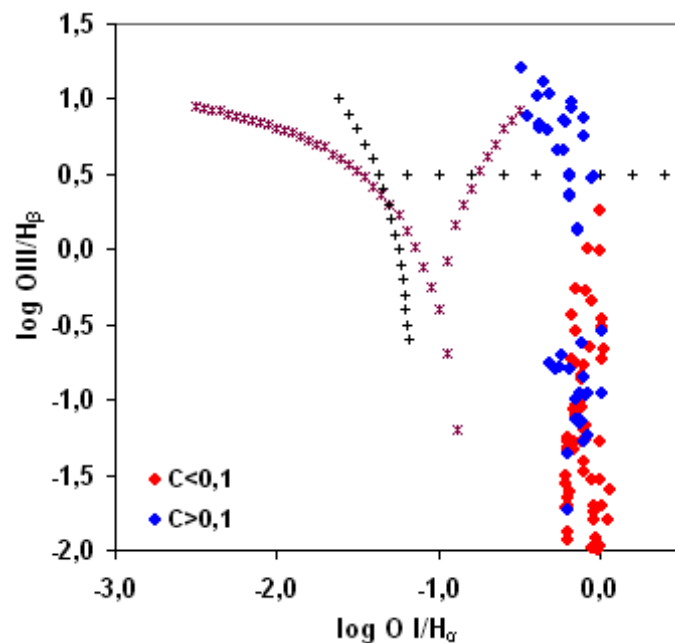
**Figure 52** presents the effect of  $f$  on the variation of the NLR parameters ( $U$ ,  $n$ , chemical composition) – The emission line ratio loci for each NLR parameter are outlined on the diagrams on the first row.




 Figure 52. Patchy corona - effect of  $f$  on NLR parameters

1. For  $U < 10^{-2}$  the intensity of  $[\text{O III}] \lambda 5007$  is higher for small  $f$
2. For  $U = 10^{-2}$  almost all emission line ratios are produced from  $f = 0$  (and occupy the AGN area)
3. The increase of  $n$  (gas density) does not affect the produced emission line ratios
4. The variation of the chemical composition from 0.5 solar to solar increases (slightly) the intensity of  $[\text{O III}] \lambda 5007$

Figure 53 presents the variation of  $C$  (disk covering factor) on the observed line ratios.

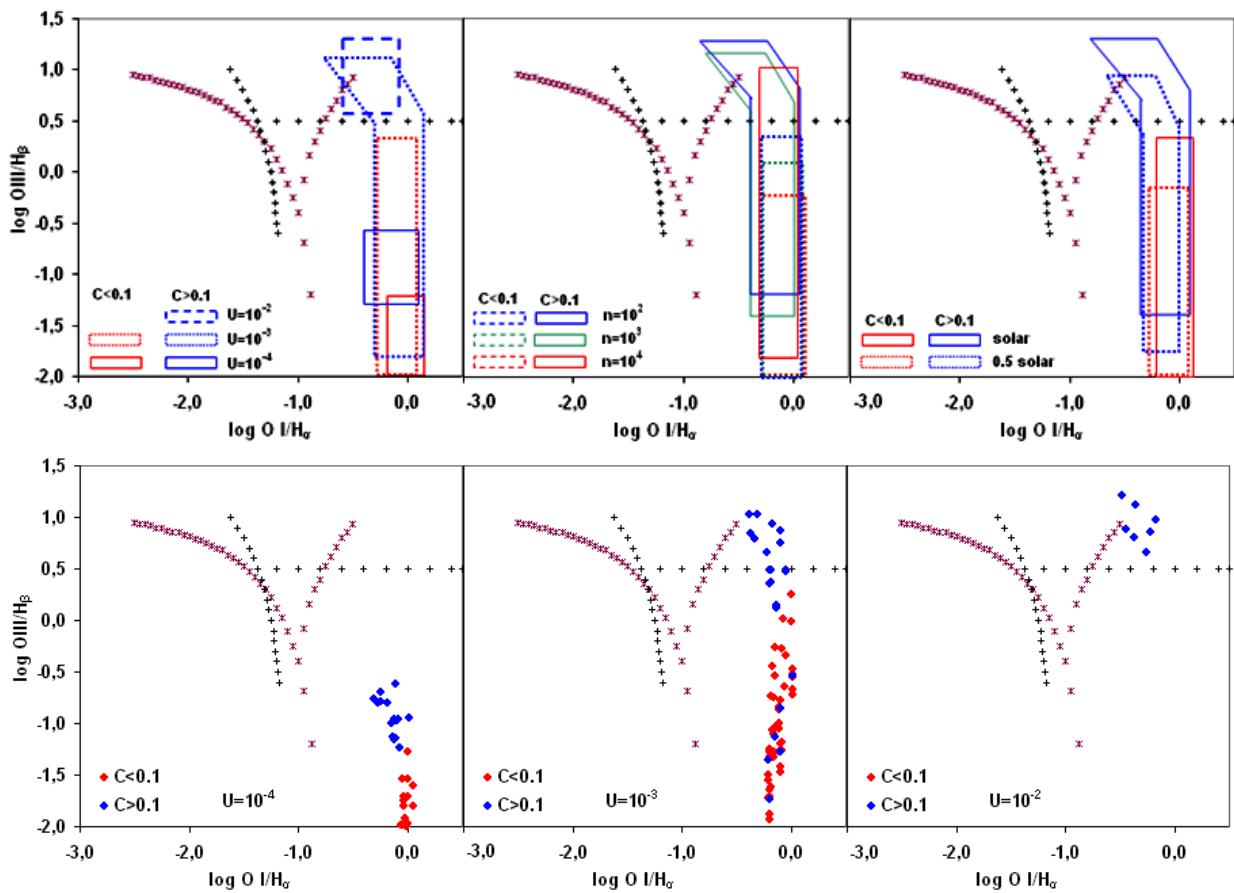

 Figure 53. Patchy corona - effect of  $C$ 

1. The intensity of  $[\text{O III}] \lambda 5007$  increases as  $C$  increases. This is quite surprising, since the increase in  $C$  should result in lower intensity of  $[\text{O III}] \lambda 5007$  as a consequence of

weaker disk emission (lower relative strength of the “big blue bump” in UV).

**2. For  $C < 0.1$  all emission line ratios occupy the area of LINERs**

**Figure 54** presents the effect of  $C$  on of the NLR parameters ( $U$ ,  $n$ , chemical composition) – The emission line ratio loci for each NLR parameter are outlined on the diagrams on the first raw.



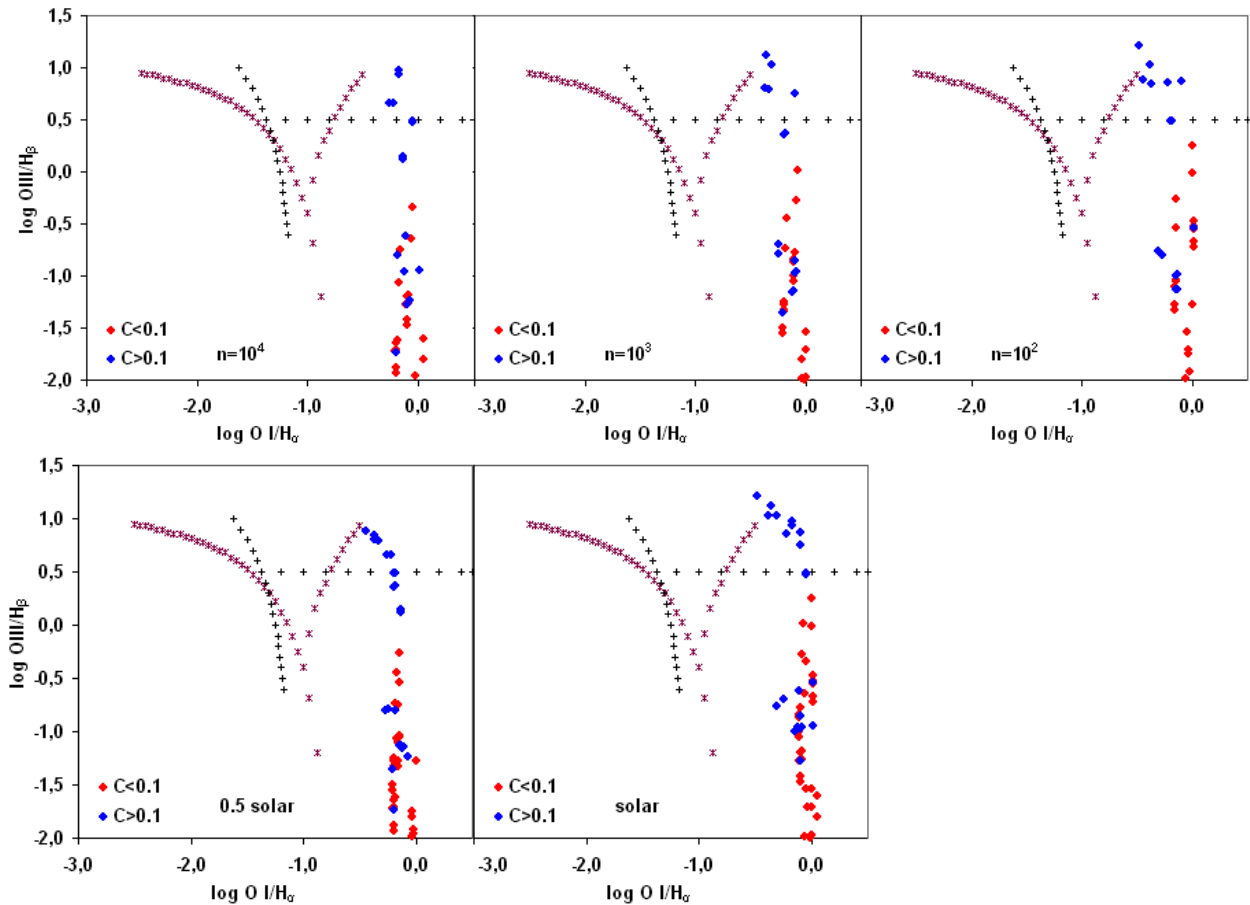


**Figure 54.** Patchy corona - effect of C on NLR parameters

1. The intensity of [O III]  $\lambda 5007$  is systematically higher for  $C > 0.1$
2. For  $U=10^{-2}$  all emission line ratios are produced from  $C > 0.1$  and all of them occupy the AGN area
3. The increase of  $n$  (gas density) does not affect the produced emission line ratios
4. The variation of the chemical composition from 0.5 solar to solar increases (slightly) the intensity of [O III]  $\lambda 5007$

**Figure 55** presents the variation of  $\mu_s$  (geometry of the clouds) on the observed line ratios.

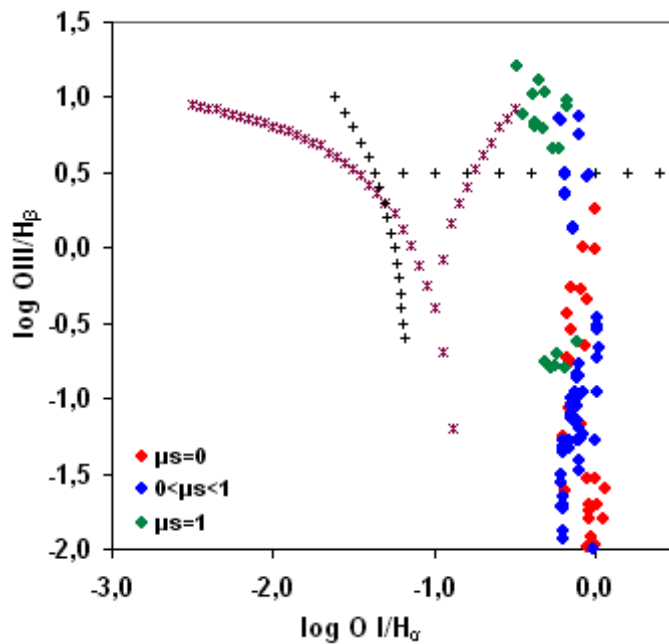
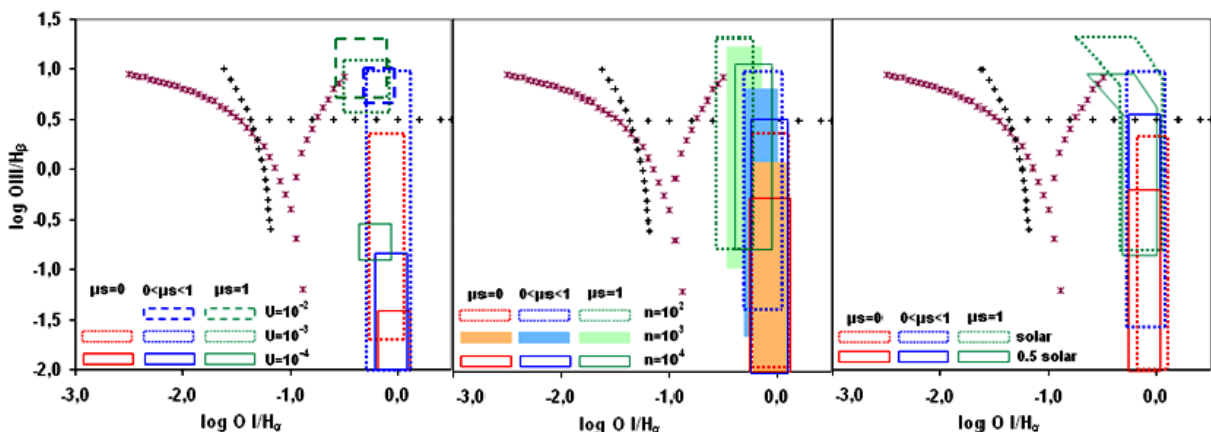


Figure 55. Patchy corona - effect of  $\mu_s$

1. **The intensity of [O III]  $\lambda$ 5007 increases as  $\mu_s$  increases.** This is expected since higher  $\mu_s$  corresponds to lower cloud radius  $R$  and as a consequence stronger disk emission (higher relative strength of the “big blue bump” in UV). For  $\mu_s = 0$  the corona covers the whole surface of the disk resulting in weaker disk emission, while for  $\mu_s = 1$  the corona vanishes (the cloud radius  $R \rightarrow 0$ ) resulting in stronger disk emission.
2. **For  $0 < \mu_s < 1$  all emission line ratios occupy the area of LINERs**

Figure 56 presents the variation of  $\mu_s$  in relation with the variation of the NLR parameters ( $U$ ,  $n$ , chemical composition) - The emission line ratio loci for each NLR parameter are outlined on the diagrams on the first row.



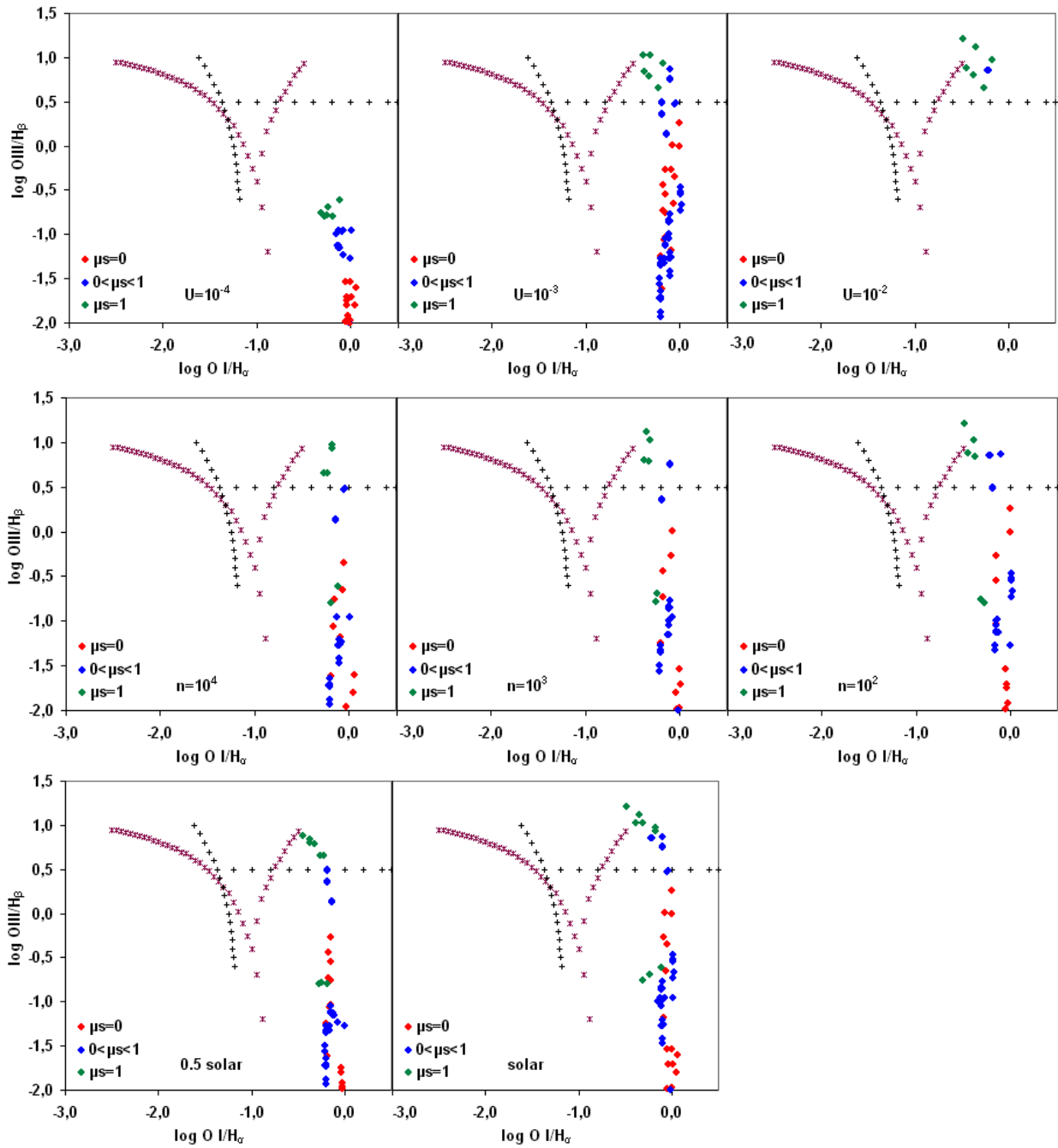


Figure 56. Patchy corona - effect of  $\mu_s$  on NLR parameters

1. As  $U$  increases, the intensity of  $[\text{O III}] \lambda 5007$  is higher as  $\mu_s$  increases
2. For  $U=10^{-2}$  almost all emission line ratios are produced from  $\mu_s = 1$  and all of them occupy the AGN area
3. The increase of  $n$  (gas density) does not affect the produced emission line ratios
4. The variation of the chemical composition from 0.5 solar to solar increases (slightly) the intensity of  $[\text{O III}] \lambda 5007$

## 2.6. Conclusions

In this work we developed a photoionization model using the CLOUDY photoionization code, based on the ionizing continuum from two self-consistent accretion flow models. The produced emission lines were analysed using the standard optical emission line diagnostic diagrams.

The key issue of the analysis was to investigate whether the accretion flow models can reproduce the emission line ratios of AGN and LINERs, which occupy well defined areas on the NLR diagrams (as defined by the separating lines of Veilleux-Osterbrock and Kewley). The results showed that the produced emission line ratios and the respective area they occupy are within the defined areas for AGN and LINERs, therefore the two self-consistent accretion flow models represent a possible geometry of the accretion flow.

Another important issue was to investigate whether we can distinguish between the accretion flow models (and consequently between the different geometries of the accretion flow region) from their produced emission line ratios. The analysis showed that it is not possible to distinguish between the accretion flow models since emission line ratios from both models occupy the same area in the NLR diagram.

A third issue was to investigate the suggestion that LINER-type AGN could be associated with truncated accretion disks (Quataer et al. 1999) similar to the geometry described in the semi-spherical inner flow model. The analysis showed that the semi spherical inner flow model produces higher values of  $[O III] \lambda 5007 / H_{\beta}$  (compared with the patchy corona model), and those values are located well into the AGN area. As a consequence, truncated accretion disks can also produce AGN type emission lines and therefore are not associated with LINER-type AGN.

---

---

## References

- Akiyama Masayuki 2001ASPC.234.539A  
Allen et al. 1998 ApJ 493 571-582  
Antonucci, R. and Miller, J. 1985, ApJ, 297, 621  
Baldwin, J. A., Phillips, M. M., & Terlevich, R. 1981, PASP, 93, 5  
Barcons et al 2002, A&A, 382, 522  
Brandl et al 2006 ApJ 653 1129-1144  
Charmandaris Vassilis & the Spitzer/IRS Instrument Team 2006, ApJ, 653, 1129  
Charmandaris Vassilis (2009) Lectures from “*PHYSICS OF GALAXIES*”  
Costero & Osterbrock 1977, Ap. I. 211, 675  
Cutri et al. 2001 ApJ, 564, L65  
Fan et al. AJ, 118, 1. 3  
Francis et al. 2004 AJ 127 646-655  
Gregg et al. 1996 AJ 112, 407  
Ho et al. 1997 ApJS 112 315-390  
Ho Luis Annual Review of Astronomy and Astrophysics, Vol. 46, No. 1. (2008), pp. 475-539.  
Kennefick et al. 1995a, AJ, 110, 78  
Kewley, L. J., Dopita, M. A., Sutherland, R. S., Heisler, C. A., & Trevena, J. 2001, ApJ, 556, 121  
Kewley Lisa (2001) “*THE AGN-STARBURST CONNECTION IN WARM INFRARED GALAXIES*”  
Laurent, O., Mirabel, I. F., Charmandaris, V., Gallais, P., Madden, S. C., Sauvage, M., Vigroux, L., & Cesarsky, C. 2000, A&A, 359, 887  
Mushotzky Richard 2003, AJ, 126, 2209  
Netzter H. (1990) “*AGN EMISSION LINES*”  
Netzter, H., Elitzur, M., and Ferland, G.J., 1985, Ap.J., 299, 752.  
Netzter, H., and Ferland, G.J., 1984, PASP, 96, 593.  
Osmer Patrick 2004cbhg.symp..324O  
Osterbrock D. Progress in Physics 54, 4, 579-633  
Osterbrock, D. E. 1993, ApJ, 404, 551  
Peterson, B.M. (1997) “*AN INTRODUCTION TO ACTIVE GALACTIC NUCLEI*” Cambridge University Press  
Politakis Haralampos (2009) “*METHODS FOR IDENTIFYING THE PRESENCE OF AN AGN*”  
Richards et al. 2001 AJ, 121, 2308  
Richards et al. 2002 AJ, 123, 2945  
Rola, Terlevich & Terlevich 1997 MNRAS, 289, 2, 419-427.  
Severgnini et al. 2003, A&A, 406, 483  
Seyfert Carl 1943 AJ, 97, 28-40  
Sparke & Gallagher “*GALAXIES IN THE UNIVERSE: AN INTRODUCTION 2nd EDITION*” Cambridge University Press  
Soboleska et al. 2004 AJ, 608 (1). pp. 80-94.  
Soboleska et a. 2004 AJ, 617 (1). pp. 102-112.  
Sturm et al. 2002, A&A , 393,821  
Tadhunter Clive 2008 New Astronomy Reviews, Volume 52, Issue 6, p. 227-239.  
Veilleux, S., & Osterbrock, D. E. 1987, ApJS, 63, 295  
Veilleux Sylvain Astronomical Society of the Pacific, 2002, p. 111  
Véron-Cetty and P. Véron 2000 A&A, 10, 1/2, 81-133  
Wadadekar Yogesh 2003 arXiv:astro-ph/0405359v1  
Whittle (2009) - Lectures from “*GRADUATE EXTRAGALACTIC ASTRONOMY*”